MONTHLY WEATHER REVIEW

A STUDY OF ENERGY CONVERSION AND MERIDIONAL CIRCULATION FOR THE LARGE-SCALE MOTION IN THE ATMOSPHERE [1]

A. WIIN-NIELSEN, Air Weather Service

Joint Numerical Weather Prediction Unit, Suitland, Md.

[Manuscript received August 31, 1959]

ABSTRACT

Energy conversion between potential and kinetic energy is considered. Section 2 contains the derivations which are necessary to compute the energy conversion for a large region on the basis of vertical velocities and relative topography as obtained from a two-parameter model presently used by the Joint Numerical Weather Prediction Unit. The energy conversion is divided into three parts: (1) energy conversion due to a mean vertical velocity over the region, (2) energy conversion in meridional planes, and (3) energy conversion in the zonal planes.

Section 3 contains a discussion of the results obtained for the months January and April 1959. The energy conversion is positive for each day in both months, but the conversion in the meridional planes has a different sign in the two months, being positive in January and negative in April. The pattern of the mean meridional circulation is discussed and the frictional dissipation estimated.

Section 4 describes a procedure for an evaluation of the energy conversion for the different wave numbers, and discusses the results for the same two months. The same section contains a comparison with results obtained from a linear, adiabatic theory.

Section 5 contains a discussion of the modifications to the results in section 4 caused by the diabatic heating of the atmosphere It is made plausible that the maximum conversion found for the small wave numbers by an adiabatic computation is greatly altered due to the effects of the heating.

1. INTRODUCTION

The problem of conversion between potential and kinetic energy has been studied by numerous authors from Margules' [9] original attempt to account for the kinetic energy of storms to very recent investigations by Phillips [13] and Smagorinsky [16] of the general circulation and the energetics of the atmosphere. These latter investigations are concerned with numerical integrations of idealized models of the atmosphere, including, however, the effects of diabatic heating and friction. A study of energy conversions based on data has been restricted in the past mainly because these conversions depend on the field of vertical motion in the atmosphere. The operational use of simplified baroclinic models of the atmosphere for short-range numerical prediction has made available daily fields of the vertical motion at at least one pressure level in the atmosphere. The vertical motion is of course computed from the model used for the numerical prediction and does not include the effects of heating and friction. It is computed under the assumption that the flow in the atmosphere is quasi-geostrophic, frictionless, and adiabatic. Consequently, it should be treated with great caution.

The vertical velocities computed from the method mentioned above seem nevertheless to be of approximately the correct order of magnitude and with the correct sign as is indicated by the use of the quantity in quantitative precipitation forecasts, for instance. It seems therefore

[1] During the preparation of this study the author became aware of a similar study conducted by Dr. Saltzman and Dr. Fleischer at Massachusetts Institute of Technology Their results for the month of February 1959 agree quite well with those reported here". (Personal communication.)

worthwhile to use the fields of vertical velocities to obtain estimates of energy conversions. An investigation of this kind was made by White and Saltzman [23] using the vertical velocities from the thermotropic model which was integrated by Gates et al. [5] for the entire month of January 1953. However, the region covered only approximately North America. A later investigation by Palmén [10] used a somewhat larger region, but this computation was made for only a few days in January 1956. The Joint Numerical Weather Prediction (JNWP) Unit has fields of vertical velocities available twice daily since November 1958. The octagonal region used in the numerical prediction covers the Northern Hemisphere down to approximately 13° N. It is these vertical velocities which have been used in the investigation reported in the following sections.

The first problem considered in this paper is the total energy conversion within the octagonal region. In connection with energy conversions it is always interesting to divide the total conversion into at least two parts, the first being due to mean meridional circulations, the other to circulations in the zonal planes. The computations were arranged to give this information together with the mean meridional circulation.

A second problem has been to study the energy conversion as it appears on the different scales of the atmospheric motions.

2. CONVERSION OF POTENTIAL TO KINETIC ENERGY

The computations which have been made assume that the atmosphere is in hydrostatic equilibrium. We are further going to consider only the kinetic energy of the horizontal flow, because the vertical velocity is small compared to the horizontal wind. An equation for the change of kinetic energy may then be obtained from the horizontal equations of motion in the following way. Let us first write the equations of motion with pressure as the vertical coordinate:

$$\frac{\partial u}{\partial t}+\mathbf{V}\cdot\nabla u+\omega\frac{\partial u}{\partial p}=-\frac{\partial \phi}{\partial x}+fv \qquad (2.1)$$

$$\frac{\partial v}{\partial t}+\mathbf{V}\cdot\nabla v+\omega\frac{\partial v}{\partial p}=-\frac{\partial \phi}{\partial y}-fu. \qquad (2.2)$$

In these equations $\mathbf{V}=\mathbf{V}\,(u,v)$ is the horizontal velocity; $\omega=dp/dt$, the "vertical velocity"; $\phi=gz$, the geopotential; g is the acceleration of gravity; z is the height of an isobaric surface; and f is the Coriolis parameter.

Multiplying (2.1) by u and (2.2) by v, adding the two equations, and defining $k=\frac{1}{2}\,(u^2+v^2)$, we obtain

$$\frac{\partial k}{\partial t}+\mathbf{V}\cdot\nabla k+\omega\frac{\partial k}{\partial p}=-\mathbf{V}\cdot\nabla\phi. \qquad (2.3)$$

Integrating (2.3) over the complete volume of the atmosphere and defining the total kinetic energy by:

$$K=\int_0^\infty\int_S \tfrac{1}{2}\rho(u^2+v^2)dSdz=\frac{1}{g}\int_0^{p_0}\int_S kdSdp, \qquad (2.4)$$

where ρ is the density and S the area over which we integrate, we obtain

$$\frac{\partial K}{\partial t}+\frac{1}{g}\int_0^{p_0}\oint_L kv_n dldp+\int_0^{p_0}\oint_L zv_n dldp=\int_0^{p_0}\int_S \omega\frac{\partial z}{\partial p}dSdp \qquad (2.5)$$

In deriving (2.5) we have used the boundary conditions $\omega=0$ for $p=0$ and $p=p_0$. We have further transformed certain area integrals into line integrals using Gauss' theorem $\left(\oint_L \text{ means a line integral around the closed boundary } L \text{ of the region } S, \text{ while } v_n \text{ is the outward directed normal velocity}\right)$.

The terms on the left side measure the change in kinetic energy of the volume, and the transport of kinetic energy and potential energy across the boundary. The term on the right hand side measures the conversion of potential to kinetic energy within the volume (White and Saltzman [23]). We shall, with Phillips' notation, write

$$\{P, K\}=\int_0^{p_0}\int_S \omega\frac{\partial z}{\partial p}dSdp \qquad (2.6)$$

where $\{P, K\}$ means the conversion from potential to kinetic energy.

The expression (2.6) was evaluated in the following way. The vertical velocities available apply at the 600-mb. level according to the model approximations, which further include the assumption that ω has a parabolic distribution with zero points at the 1000- and 200-mb. levels. The derivative was evaluated by finite differences as

$$\frac{\partial z}{\partial p}=-\frac{1}{35}h \qquad (2.7)$$

where h is the thickness field between 850 and 500 mb. This approximation for $\partial z/\partial p$ was used only because h was available for each day.

When the two approximations are introduced in (2.6) we arrive at the following formula

$$\{P, K\}=-\frac{32}{21}\int_S \omega h dS \qquad (2.8)$$

where ω now is the vertical velocity at 600 mb.

Let us next separate ω and h into their mean values and deviations from these mean values. We define

$$\left.\begin{array}{l} h=\bar{h}+h' \\ \omega=\bar{\omega}+\omega' \end{array}\right\} \qquad (2.9)$$

where the mean values are defined as area means:

$$\overline{(\ )}=\frac{1}{S}\int_S (\ )\,dS. \qquad (2.10)$$

Inserting the expression (2.9) in (2.8) we obtain

$$\{P, K\} = -\frac{32}{21}\,\bar{\omega}\bar{h}S - \frac{32}{21}\int_s \omega'h'dS. \qquad (2.11)$$

The first term in (2.11) represents an energy conversion due to a mean vertical velocity over the region. Now, if S were the complete surface of the sphere we would have $\bar{\omega}=0$, because

$$\bar{\omega} = -\frac{1}{S}\int_0^p \int_s \nabla\cdot\mathbf{V}\,dS dp \equiv 0, \qquad (2.12)$$

i. e., the divergence integrated over the sphere is zero. For a restricted region S, as used in these computations, there is no assurance that $\bar{\omega}=0$. We find in general from the data that $\bar{\omega}$ has small positive or negative values. The first term in (2.11) was computed separately.

It is furthermore of interest to divide the last term in (2.11) into energy conversion due to the presence of a mean meridional circulation. We define therefore the mean meridional circulation by the following operator:

$$(\widetilde{}) = \frac{1}{L}\int_0^L (\ ) dx \qquad (2.13)$$

where L is the length of the latitude circle and x the eastward directed coordinate.

Writing now:

$$\left.\begin{array}{l} h' = \tilde{h}' + h'' \\ \omega' = \tilde{\omega}' + \omega'' \end{array}\right\} \qquad (2.14)$$

we obtain

$$\{P, K\} = -\frac{32}{21}\,\bar{\omega}\bar{h}S - \frac{32}{21}\int_s \tilde{\omega}'\tilde{h}'dS - \frac{32}{21}\int_s \omega''h''dS$$

$$= \{P, K\}_1 + \{P, K\}_2 + \{P, K\}_3. \qquad (2.15)$$

The term $\{P, K\}_2$, the energy conversion in the mean meridional circulation, was also computed separately.

The values of the vertical velocity and the relative topography used in these computations were given at the grid points of a quadratic grid on a polar-stereographic projection (standard latitude 60° N.). Special care has therefore to be taken when we perform the numerical integrations of the different terms in 2.15). Let us consider, as an example, the last integral $\{P, K\}_3$. We have

$$\{P, K\}_3 = -\frac{32}{21}\int_s \omega''h''dS \simeq -\frac{32}{21}\sum_i\sum_j \omega''_{ij}h''_{ij}(\Delta S)_e \qquad (2.16)$$

where $(\Delta S)_e$ is the area on the earth corresponding to an elementary grid square on the map. Performing the computations on the map leads then to the expression

$$\{P, K\}_3 = -\frac{32}{21}\sum_i\sum_j \omega''_{ij}h''_{ij}(1/m^2)(\Delta S)_m \qquad (2.17)$$

where m is the map scale factor, $(1+\sin 60°)/(1+\sin \phi)$,

and $(\Delta S)_m$ is the square of the grid interval at the standard latitude, in our case $(3.81\times 10^5)^2\text{m.}^2$ Similar caution was taken in forming the mean values $(\bar{})$ and $(\widetilde{})$ and in evaluating the other integrals.

The three terms $\{P, K\}_i$, $i=1$, 2, 3 in (2.15) may be thought of as conversions due to (1) a mean vertical lifting or sinking of the air mass within the region S, (2) circulations in the meridional plane, and (3) circulations in the zonal plane. The two last terms measure also according to Lorenz [7] transformations between zonal available potential energy and zonal kinetic energy and transformation between eddy available potential energy and eddy kinetic energy, respectively.

3. RESULTS OF THE TOTAL ENERGY CONVERSIONS

The procedure outlined in the preceding section was used to compute the three terms in (2.15) for each day in the months January and April 1959. Only the data applying at 0000 GMT were used in the computations.

Let us first summarize the results obtained for January 1959. Table 1 contains in the first row the total energy conversion in the average for the month in the unit kj. sec.$^{-1}$. In the second row the same results are rewritten in the unit kj. sec.$^{-1}$m.$^{-2}$ by dividing by the total area of the octagonal region $(1.97\times 10^{14}\text{ m.}^2)$. For comparison with other estimates the numbers in the second row are converted to the c.g.s. units, erg, gm.$^{-1}$, sec.$^{-1}$ and written in the last row.

Now, in considering the numbers presented in table 1 we notice a number of interesting things. The first column shows (see (2.15)) that the initial vertical velocities indicate a mean downward motion. The mean vertical motion was in fact downward on 70 percent of the days going into the computation. We shall not include $\{P, K\}_1$ in our measure of the total energy conversion since this term would be zero if we considered the whole earth. It would, incidentally, be an advantage to impose the constraint $\bar{\omega}=0$ in the numerical forecasts with two-parameter baroclinic models over an almost hemispheric region in order to avoid fictitious changes in total circulation, as shown by the author (Wiin-Nielsen [21]). If $\bar{\omega}\neq0$, as in these computations, we get a significant energy conversion solely due to the mean lifting of sinking, amounting to about 10 percent of the sum of $\{P, K\}_2$ and $\{P, K\}_3$.

The next important quantity to consider is the energy conversion due to the mean meridional circulation. Our region is so large that it includes the whole polar region, the mid-latitudes, and at least part of the Tropics. The

TABLE 1.—*Total energy conversion computed for January 1959.*

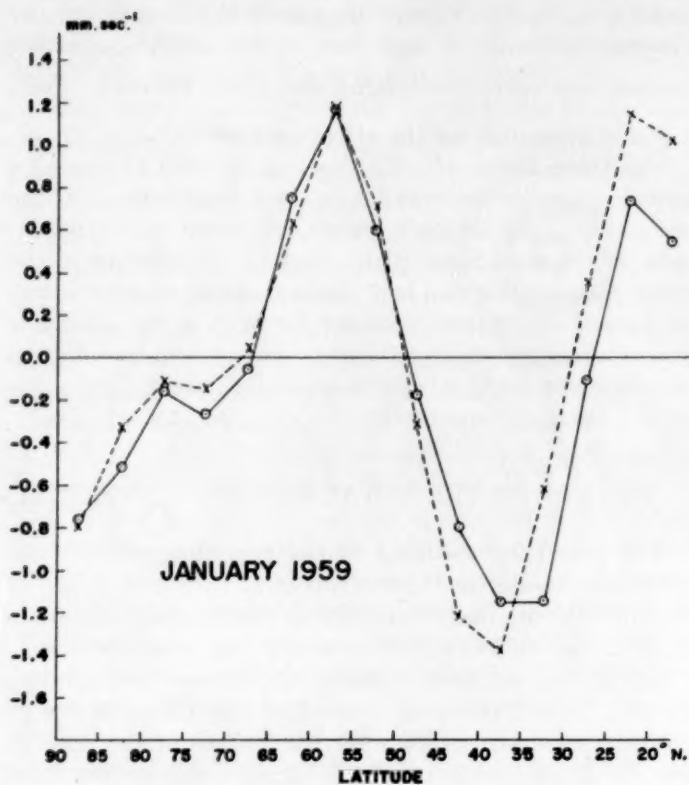| Unit	$\{P, K\}_1$	$\{P, K\}_2$	$\{P, K\}_3$
kj. sec.$^{-1}$	-3.14×10^{10}	$+2.04\times 10^{10}$	$+28.82\times 10^{10}$
kj. sec.$^{-1}$m.$^{-2}$	-1.59×10^{-4}	$+1.03\times 10^{-4}$	$+14.60\times 10^{-4}$
erg gm.$^{-1}$ sec.$^{-1}$	-0.159	$+0.103$	$+1.46$

FIGURE 1.—Vertical velocity in units mm. sec.$^{-1}$ averaged along latitudes and in time, for January 1959. The solid curve was computed from observed data, the dashed curve from 36-hour forecasts.

adiabatic method of computing the vertical velocity makes use in our case of the geostrophic wind. This method would certainly break down at and near the equator. As the mean latitude of the southern boundary of the octagon is about 13° N., we can probably believe in the vertical velocities even in the southern portions of the grid. The computation for January shows that we have a positive conversion of potential to kinetic energy in the meridional planes, although it amounts to only about 7 percent of the energy conversion in the zonal planes. It is very interesting first to see what kind of meridional circulation we have in the average for the month. This mean meridional circulation was found by averaging the vertical velocity for each day in the month and then computing the average for the month. The result is given in figure 1, where the horizontal coordinate is latitude from the pole down to 20° N., while the vertical coordinate is the mean vertical velocity in the unit mm. sec.$^{-1}$. Figure 1 shows that the mean meridional circulation for this month definitely consists of the classical three cells with rising motion to the south, the maximum downward motion around 35° N., the maximum upward motion between 55° and 60° N., and downward motion over the polar region.

The dashed curve on figure 1 indicates the mean meridional motion for January 1959 for the 36-hour forecasts.

The three-cell pattern is still very well defined in the 36-hour forecasts, but there seems to be a tendency to produce great upward motion in the southernmost portions of the region, and perhaps to shift the maximum downward motion somewhat to the north by about 5° of latitude. Now, with a well-defined indirect cell in the middle latitudes, this cell alone would give a conversion of kinetic energy to potential energy as was also found by White and Saltzman [23] in their computation which uses data for January 1953 between 35° N. and 60° N. The net positive value obtained in this computation shows that the conversion from potential to kinetic energy in the two direct cells to the north and the south is sufficient to give a positive conversion for the whole meridional circulation. It should also be stressed that the main part (93 percent) of the conversion takes place in the zonal planes.

The presence of the three-cell meridional circulations in the initial vertical velocities is especially interesting because these vertical motions are computed from a model which does not include the effect of friction and diabatic heating. It has been pointed out by Phillips [12] in a theoretical study that the three-cell meridional circulation is a result of the presence of baroclinic unstable waves. Phillips also computed the intensity of the vertical velocity in the meridional cross section. In order to make this computation he has estimated an average warming of the northern latitudes of about 0.5° C. day^{-1} in order to balance the yearly average cooling due to radiation over the northern half of the Northern Hemisphere. In this way he arrives at a maximum mean vertical motion of about 3 mb. day^{-1} which, converted to our units, corresponds to about 0.5 mm. sec.$^{-1}$ The computation of the mean meridional circulation made here is certainly in agreement with Phillips' computation as far as the pattern and order of magnitude are concerned, although it seems that the mean meridional circulation is somewhat stronger in the particular month.

The total energy conversion for January 1959 amounts to about 31 × 10^{10} kj. sec.$^{-1}$ when we add the contribution from the circulations in the meridional and zonal planes. As our region is very large we are probably allowed in the first approximation to neglect the contributions from the advection of kinetic and potential energy into the region; see equation (2.5). If this is the case, we have that the change in total kinetic energy is equal to the conversion from potential to kinetic energy minus the frictional dissipation. Including now the frictional dissipation in equation (2.5) we obtain

$$\frac{\partial K}{\partial t} = \{P, K\} - D \qquad (3.1)$$

where D measures the frictional dissipation. In a long-term mean we have $\partial K/\partial t = 0$ and the conversion from potential to kinetic energy must balance the frictional dissipation; i.e.,

$$D=\{P,K\} \tag{3.2}$$

If we assume that $\partial K/\partial t=0$ for the month of January 1959, we find that $D=31 \times 10^{10}$ kj. sec.$^{-1}$ or about 1.6×10^{-3} kj. m.$^{-2}$ sec.$^{-1}$, a value which agrees rather well with the value estimated by Pisharoty [11], who obtained 2×10^{-3} kj. m.$^{-2}$ sec.$^{-1}$ The value obtained from the present study is about one-third of the estimate made by Brunt [1]: 5×10^{-3} kj. m.$^{-2}$ sec.$^{-1}$ White and Saltzman [23] obtained for the middle latitudes a value closer to Brunt's, while Palmén's [10] recent computation agrees well with the value obtained in this study.

The integrals in (2.5) may be thought of as sums of contributions from different sub-regions of S, although the contribution from a subregion is not related directly to the change of energy within the region because of the contribution from the boundary integrals; i.e., transport of potential and kinetic energy into the region. In the computation of the total energy conversions for the region S, the contribution from each 5-degree latitude ring was computed. We could look upon these values as changes of the kinetic energy, if there were no transport across the boundaries, or simply as measures of the correlation between the vertical motion and the relative topography (i.e., the mean temperature). The contributions from the 5-degree latitude bands are plotted in figure 2, where the horizontal coordinate is latitude and the vertical coordinate has the dimension of an energy conversion per unit area and unit time. As shown by the figure the greatest positive correlation is in the band between 40° and 45° N. and in the polar regions. In these regions therefore in the average warm air is rising and cold air sinking, while this to a much lesser extent is true in the latitude bands 55°–65° N. and 20°–35° N. The northernmost region of these two represents for this month a region where we have a small negative correlation, meaning that in the average the warm air is sinking and the cold air rising. The curve agrees fairly well with the one given by White and Saltzman [23] for the latitude band 35°–60° N.

The computations reported so far give energy conversions as computed from initial data. There are therefore no forecasts involved except for the very first time step which in the present scheme is necessary in order to solve for the vertical velocity in the adiabatic equation. This procedure could actually be avoided by solving the so-called ω-equation (see later). From the point of view of numerical prediction it is of interest to investigate the conversion of potential to kinetic energy as the forecast progresses in time. This investigation may be made along the same lines as outlined in section 2 replacing ω and h by the corresponding forecast values.

The models so far used in short-range prediction have been adiabatic and frictionless. For such a model the energy equation states that the sum of kinetic and potential energy is constant. As the models also have been hydrostatic, the internal energy per unit column is proportional to the potential energy, and the sum of the two
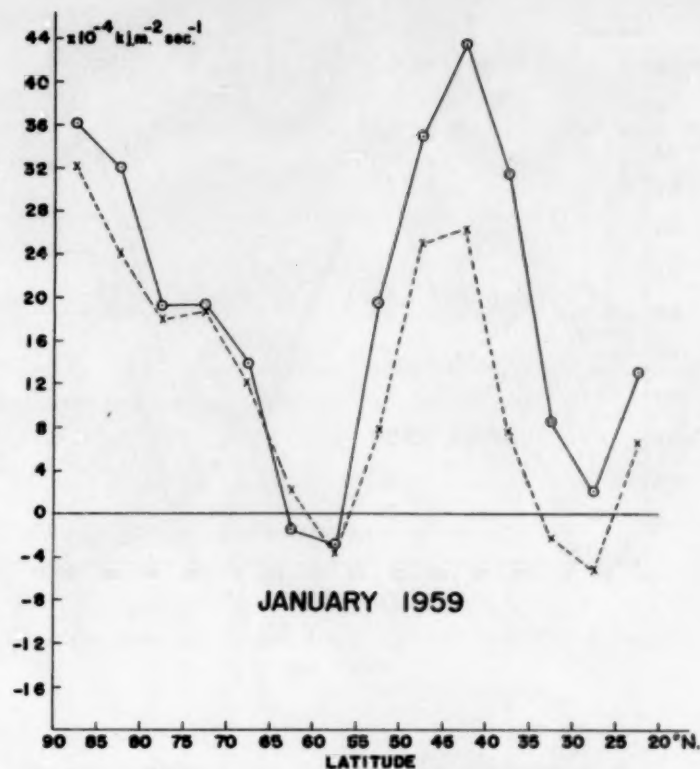

FIGURE 2.—Correlation between vertical velocity and mean temperature expressed as an energy conversion per unit area and unit time as a function of latitude for January 1959. The solid curve was computed from observed data, the dashed curve from 36-hour forecasts.

will be called, as is now customary, the potential energy. As shown by Lorenz [8] the sum of kinetic energy and the available potential energy A is also constant for an adiabatic model, and he estimates that the ratio between kinetic energy and available potential energy is of the order of magnitude of 10^{-1}. One important question is whether the rate of increase of kinetic energy in a model used for numerical prediction is about the same as in the real atmosphere. We shall be able to answer this question by computing the energy conversion at, for instance, 12, 24, and 36 hours under the assumption that the region is so large that it can be considered closed. For simple sinusoidal waves it can be shown that the energy conversion in a quasi-geostrophic model depends upon the phase-lag between the temperature (thickness) field and the pressure field. If the temperature field lags behind the pressure field, as it usually does in the atmosphere, a positive conversion will take place, while the opposite is true in the reverse situation. Now, it has been noted by Thompson [18] that one of the errors in the quasi-geostrophic models is that the phase difference between the temperature field and the pressure field decreases too rapidly as compared to the real atmosphere. We may therefore expect that the energy conversion takes place too rapidly in the models, if the observation above is quite general.
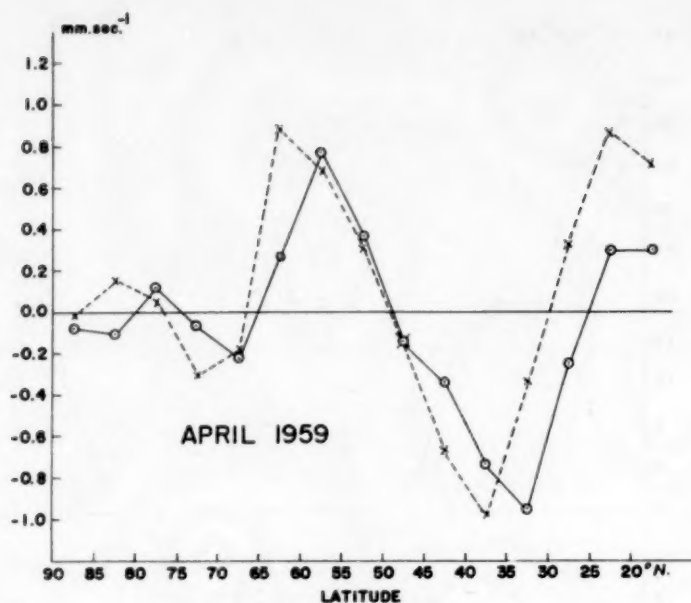
FIGURE 3.—Vertical velocity, April 1959. For explanation see figure 1.

It is interesting to notice that this is indeed the case. The 36-hour forecast for the month of January has an energy conversion which in total amounts to 24×10^{10} kj. sec.$^{-1}$ as compared to 31×10^{10} kj. sec.$^{-1}$ for the initial data, or roughly ¾ of what it should be. An inspection of the data for the individual days indicates further that there were no days when the conversion computed from the 36-hour forecast was greater than the one in the corresponding initial data. It may therefore be concluded that the conversion of potential energy to kinetic energy in the quasi-geostrophic model gradually decreases as the forecast progresses in time. This fact is also shown clearly in figure 2, where the dashed curve gives the correlation for the month of January between vertical velocity and relative topography in the 36-hour forecasts. Although the general characteristics of the curve are the same, the average level is lower.

In order to investigate whether the same general characteristics would hold for another month the computations were carried out for April 1959. They are summarized in table 2 and in figures 3 and 4.

TABLE 2.—*Total energy conversion computed for April 1959.*

Unit	$\{P, K\}_1$	$\{P, K\}_2$	$\{P, K\}_3$
kj. sec.$^{-1}$	-7.72×10^{10}	-2.12×10^{10}	$+21.66 \times 10^{10}$
kj. sec.$^{-1}$m.$^{-2}$	-3.92×10^{-4}	-1.08×10^{-4}	$+11.00 \times 10^{-4}$
erg gm.$^{-1}$sec.$^{-1}$	-0.392	-0.108	$+1.100$

Table 2 shows that we again have a negative contribution from the term $\{P, K\}_1$ indicating a net downward motion over the entire region in the majority of the cases.
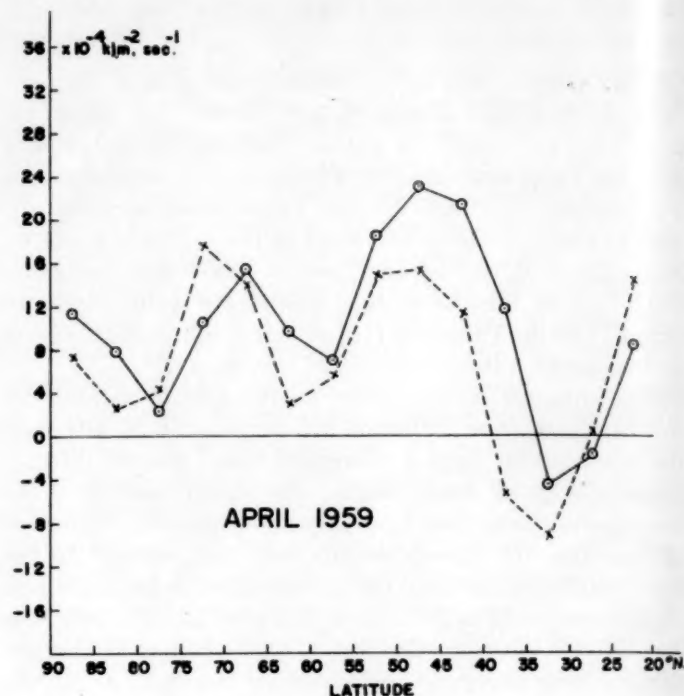

FIGURE 4.—Correlation between vertical velocity and mean temperature, April 1959. For explanation see figure 2.

In April it turns out that an average downward motion exists on all days except one.

Contrary to the situation in January we find now that the mean meridional circulation converts kinetic energy into potential energy. The mean meridional circulation still has the three-cell pattern, although some irregularities now exist in the very high latitudes. The mean vertical motion is weaker in April than in January, but the extreme values appear approximately at the same latitudes in the two months. The main difference between the two months is probably that the direct cells in the low and high latitudes are less developed in April, while the indirect cell in the middle latitudes, although somewhat weaker, still is well defined and regular. These differences account for the different signs of the energy conversion in the meridional plane. However, the energy conversion $\{P, K\}_2$ in April is still a rather small fraction of the conversion in the zonal planes (about 10 percent).

If we, for April, assume that the change of the total kinetic energy is zero ($\partial K/\partial t = 0$), we obtain the result that the frictional dissipation for this month amounts to about 1.0×10^{-3}kj. m.$^{-2}$ sec.$^{-1}$ as compared to 1.6×10^{-3} kj. m.$^{-2}$ sec.$^{-1}$ in January.

The correlation between vertical velocity and relative topography, again expressed as an energy conversion per unit area and time, is given in figure 4. We find again that the greatest positive correlation is around $45°$ N., and

that high correlations exist in the high latitudes although more irregularly than in January.

The 36-hour forecast vertical velocity gives the mean meridional circulation drawn as the dashed curve in figure 3. The main error in the 36-hour forecasts for this month is a shift to the north amounting to about 5° of latitude for the maxima and minima, and again we note that the forecast vertical velocities in the low latitudes are somewhat larger than observed. This difference is probably due to erroneous boundary conditions.

The conversion indicated by the 36-hour forecasts is again somewhat smaller in April than the one given by the initial data. While the initial data give a conversion of about 20×10^{10} kj. sec.$^{-1}$ within the octagonal region, we obtain only about 17×10^{10} kj. sec.$^{-1}$ for the 36-hour forecasts, or 85 percent of the value given by the initial data.

4. ENERGY CONVERSIONS ON DIFFERENT SCALES

It has been known for a long time that the atmosphere is not equally effective in releasing potential energy on different scales. According to baroclinic instability theory we find certain scales (4000–6000 km.) which are the most unstable. It is also known that the unstable baroclinic wave converts potential to kinetic energy. The results mentioned above have been obtained from theoretical studies using a linear perturbation theory. An evaluation of the energy conversion on the different scales is therefore worth while doing, first of all to get a check on the validity of the linear perturbation theories, and secondly to investigate whether other energy conversions not treated by the theory could be important. Saltzman [14] has recently considered the energy equation in the wave-number regime. We shall here be interested in only the direct conversion of potential to kinetic energy.

Let us return to the equation (2.8) giving the conversion from potential to kinetic energy:

$$\{P, K\} = -\frac{32}{21} \int_S \omega h dS. \qquad (4.1)$$

We shall in the following consider only a sub-region of the complete octagonal region. For convenience we divide the polar-stereographic map into rings having the center at the north pole. The width of the rings is one grid increment on the map. With this arrangement we have:

$$\int_S \omega h dS = \int_0^y \int_0^{2\pi} \omega h R \cos \phi d\lambda dy \qquad (4.2)$$

where R is the radius of the earth, considered as a sphere, ϕ is latitude, λ longitude, and y the measure of length in the south-north direction. We may also write (4.2) in the form:

$$\int_S \omega h dS = R \int_0^y I(y) \cos \phi dy \qquad (4.3)$$

with

$$I(y) = \int_0^{2\pi} \omega(\lambda, y) h(\lambda, y) d\lambda \qquad (4.4)$$

Let us next write $\omega(y)$ and $h(y)$ as Fourier-series in the form:

$$\left. \begin{aligned} \omega(\lambda, y) &= a_0(y) + \sum_{n=1}^{N} \{a_n(y) \sin (n\lambda) + b_n(y) \cos (n\lambda)\} \\ h(\lambda, y) &= A_0(y) + \sum_{n=1}^{N} \{A_n(y) \sin (n\lambda) + B_n(y) \cos (n\lambda)\} \end{aligned} \right\} \quad (4.5)$$

Inserting (4.5) into (4.4) and using the orthogonality of the functions $\cos (n\lambda)$ and $\sin (n\lambda)$ we obtain:

$$I(y) = 2\pi a_0(y) A_0(y) + \pi \sum_{n=1}^{N} \{a_n(y) A_n(y) + b_n(y) B_n(y)\}. \quad (4.6)$$

The formulae for the Fourier coefficients are:

$$\left. \begin{aligned} a_0(y) &= \frac{1}{2\pi} \int_0^{2\pi} \omega(\lambda, y) d\lambda \\ a_n(y) &= \frac{1}{\pi} \int_0^{2\pi} \omega(\lambda, y) \sin (n\lambda) d\lambda, \\ b_n(y) &= \frac{1}{\pi} \int_0^{2\pi} \omega(\lambda, y) \cos (n\lambda) d\lambda \end{aligned} \right\} \quad (4.7)$$

and corresponding expressions for $A_0(y)$, $A_n(y)$, $B_n(y)$.

Let us next consider the evaluation of the complete integral. We have

$$\int_0^y I(y) \cos \phi dy = \int_0^y I(y) \cos \phi \frac{dS}{m(\phi)} \qquad (4.8)$$

where dS now is the distance on the map. Evaluating the last integral by finite differences we obtain

$$\int_0^y I(y) \cos \phi dy = \frac{\Delta S}{(1 + \sin \phi_0)} \sum_{j=1}^{j_{max}} I_j \cos \phi (1 + \sin \phi) \quad (4.9)$$

where we have introduced the expression $m = (1 + \sin \phi_0)/(1 + \sin \phi)$ and also the symbol j for the counter of the rings. With the present JNWP grid $j_{max} = 27$; the counter j is considered to increase from the North Pole toward the equator on the map.

It is now convenient to rewrite the original expression in the form:

$$\{P, K\} = \{P, K\}_{(0)} + \sum_{n=1}^{N} \{P, K\}_{(n)} \qquad (4.10)$$

where

$$\left. \begin{aligned} \{P,K\}_{(0)} &= -\frac{32}{21} \frac{\Delta S}{(1 + \sin \phi_0)} \times \\ &\qquad \sum_{j=1}^{j_{max}} \{\cos \phi (1 + \sin \phi) a_0(j) A_0(j)\} \\ \{P,K\}_{(n)} &= -\frac{32}{21} \frac{\Delta S}{(1 + \sin \phi_0)} \times \\ &\qquad \sum_{j=1}^{j_{max}} \{\cos \phi (1 + \sin \phi) (a_n(j) A_n(j) + b_n(j) B_n(j))\} \end{aligned} \right\} \quad (4.11)$$

The Fourier coefficients were computed using a procedure developed by G. 'Arnason, formerly at JNWP. The arrangement of the grid points in the octagonal grid is not directly suited for a Fourier analysis along latitude circles. A short description of the procedure is therefore necessary.

Each of the zonal bands with a width ΔS is divided into zones of $10°$ of longitude ($\Delta\lambda = 10°$). Exceptions to this are made for the high latitudes. In each zone k we define

$$\left. \begin{array}{l} \overline{(\alpha \sin n\,\lambda)_k} = \dfrac{1}{N_k} \sum_{i=1}^{N_k} (\alpha \sin n\lambda)_i \\[2mm] \overline{(\alpha \cos n\,\lambda)_k} = \dfrac{1}{N_k} \sum_{i=1}^{N_k} (\alpha \cos n\lambda)_i \end{array} \right\} \quad (4.12)$$

N_k is the number of grid points in the zone, k. The Fourier coefficients are then computed using the formulae

$$a_n = \frac{1}{18} \sum_{k=1}^{36} \overline{(\alpha \sin n\lambda)_k}, \quad b_n = \frac{1}{18} \sum_{k=1}^{36} \overline{(\alpha \cos n\lambda)_k} \quad (4.13)$$

The increments $\Delta\lambda$ are as follows:

$$j \geq 9, \; \Delta\lambda = 10°$$
$$9 > j \geq 5, \; \Delta\lambda = 20°$$
$$5 > j \geq 3, \; \Delta\lambda = 30°$$
$$3 > j > 0, \; \Delta\lambda = 60°$$

where j, as noted earlier, is the counter of grid distances from the pole.

The computations were again made for each day of January and April 1959. The energy conversion was averaged for the month to get a picture of the mean conditions. The results are shown in figures 5 and 6.

For each day the Fourier analysis was made up to wave number 15 to be on the safe side. In the middle latitudes ($\phi = 45°$ N.) $n = 15$ would correspond to a wavelength of 1800 km., which probably is about the smallest wavelength we can hope to analyze with any accuracy with our present aerological network. It turns out, as can be seen on figures 5 and 6, that the energy conversion is negligible for $n \geq 11$.

The spectra show for both months two rather broad maxima for $n = 2$ and $n = 6$ in January and $n = 2$ and $n = 7$ in April. The maximum corresponding to $n = 6$ or 7 is clearly connected with the most unstable baroclinic wave. Converting again to wavelength in the middle latitudes we find that $n = 6$ and 7 correspond roughly to wavelengths of 4700 and 4000 km., which coincides well with the most unstable waves as predicted from the linear perturbation theory.

It is furthermore predicted by linear perturbation theory that all waves with a wavelength shorter than about 3000 km. for the middle latitudes should be stable. This coincides rather well with the abrupt cutoff in the spectra for $n = 10$, which corresponds to $L = 2800$ km.

These results support strongly the results of the linear theory. It is in fact not too difficult to see that an adiabatic linear theory must give a result of this nature.

Let us consider a simple sinusoidal wave pattern in the atmosphere. The stream function at 600 mb. and the thermal stream function for the layer 800 to 600, or 600 to 400 mb. will be given in the form

$$\left. \begin{array}{l} \psi_2 = -U_2 y + A \sin mx \\[1mm] \psi' = -U' y + B \sin (mx + \alpha) \end{array} \right\} \quad (4.14)$$

where U_2 and U' are the zonal winds considered as constants, A and B the amplitudes, $m = 2\pi/L$ the wave number, and α the phase-difference between the thermal wave and the stream function. Note that α is positive if the thermal wave is behind the pressure wave.

We want in the following to find the energy conversion for the wave pattern. In order to do this we need the vertical velocity field. This can be found from the ω-equation which for the simple baroclinic model underlying the computations here takes the form
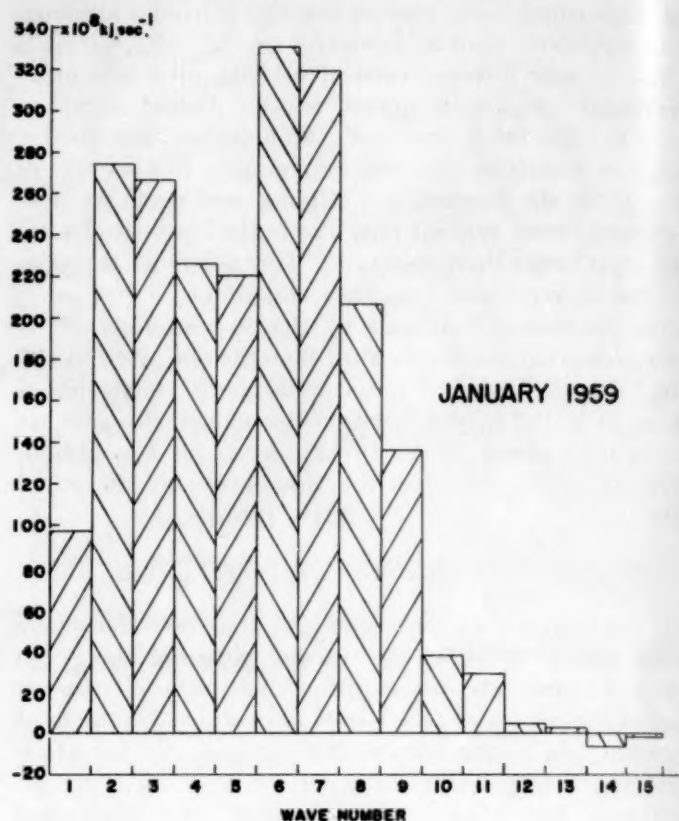

FIGURE 5.—Energy conversion as a function of wave number averaged in time, for January 1959. The horizontal coordinate is number of waves around the hemisphere, while the vertical coordinate is energy conversion per unit time north of about 15° N.
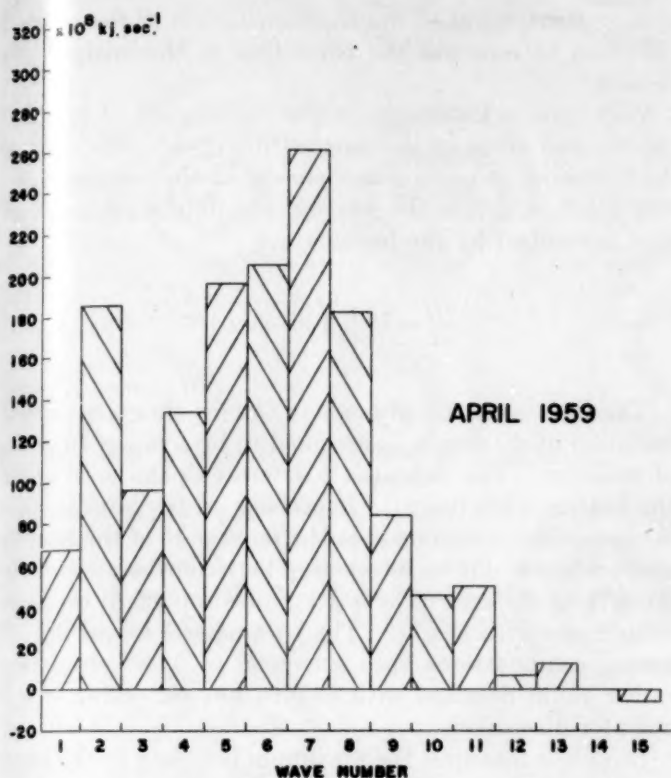
APRIL 1959

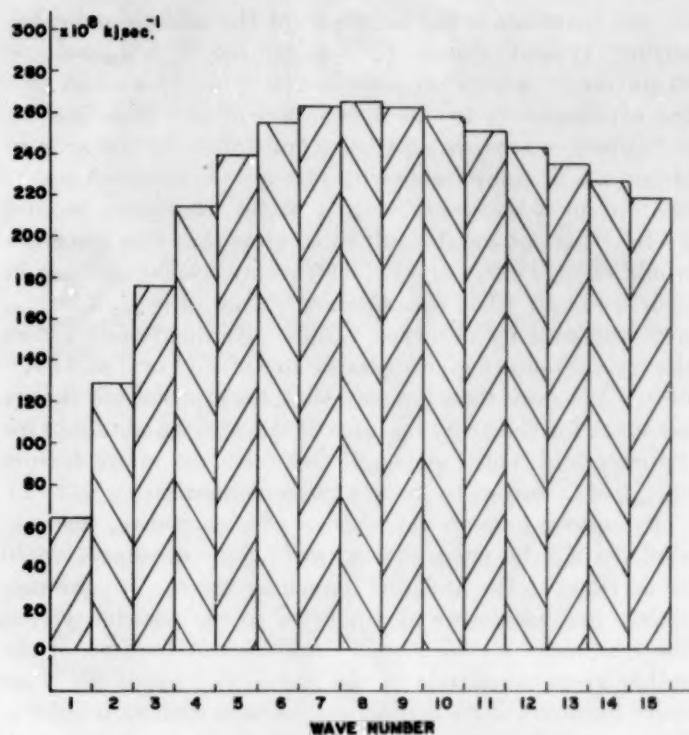FIGURE 6.—Energy conversion, April 1959. For explanation see figure 5.

FIGURE 7.—Energy conversion as a function of wave number according to linear adiabatic theory keeping all parameters except the wave number constant.

$$\sigma\nabla^2\omega_2-\frac{2f_0^2}{P^2}\,\omega_2=\frac{2f_0}{P}\{\nabla^2(\mathbf{V}_2\cdot\nabla\psi')-\mathbf{V}_2\cdot\nabla\zeta'-\mathbf{V}'\cdot\nabla(\zeta_2+f)\}$$

(4.15)

For the details in this derivation the reader is referred to a paper by the author [21], in which it also is shown that a solution to (4.15) may be written in the form,

$$\omega_2=\frac{2f_0}{P}\,\frac{1}{m^2\sigma+\frac{2f_0^2}{P^2}}\,(\beta v'-2m^2U'v_2)$$

(4.16)

for the simple waves given by (4.14).   In (4.15) and (4.16) $\sigma=-\alpha\partial\ln\theta/\partial p$ is a measure of static stability, $P=40$ cb., and $v_2=\partial\psi_2/\partial x$, $v'=\partial\psi'/\partial x$ are the meridional velocities in the waves given by (4.14).

The energy conversion per unit area may now easily be computed by inserting the expression for ω_2 and ψ' in the formula

$$\frac{1}{S}\,\{P,\,K\}=-\frac{32}{21}\frac{1}{S}\int_s\omega_2h\,dS\simeq-\frac{32}{21}\frac{1}{S}\frac{f_0}{g}\int_s\omega\psi'\,dS.$$ (4.17)

As there is no variation in the y-direction we may take the area S as a unit band; i.e., $S=1\cdot L=2\pi R\cos\phi$. We obtain then

$$\frac{1}{S}\,\{P,\,K\}=\frac{32}{21}\frac{f_0^2}{gP}\,U'v_{2\,max}\,v'_{max}\sin\alpha\,\frac{2m}{m^2\sigma+\frac{2f_0^2}{P^2}}\cdot$$ (4.18)

Expressed in this form we find that the energy conversion depends upon (1) the zonal thermal wind, (2) the amplitude of the meridional wind components, (3) the phase-lag between the thermal field and the stream function, and (4) the scale (wave number).

If we next introduce the number of waves n around the hemisphere into (4.18); i.e., $m=n/R\cos\phi$, we obtain:

$$\frac{1}{S}\,\{P,\,K\}=\frac{32}{21}\frac{f_0^2}{gP}\,U'v_{2\,max}\,v'_{max}\sin\alpha R\cos\phi\,\frac{2n}{n^2\sigma+\frac{2f_0^2}{P^2}R^2\cos^2\phi}\cdot$$

(4.19)

Several investigations, the first one by Charney [2], have shown that the meridional components $(v_2,\,v')$ will be greatest for the baroclinic waves $(n=6$ or $7)$ and for the ultra-long waves $(n=2$ or $3)$. The wind components above in (4.19) will therefore tend to give a maximum for the wave numbers mentioned above. Beside this there is a definite influence of the scale of the motion as expressed by the last factor in (4.19). If we for a moment assume that $v_{2\,max}$ and v'_{max} are the same for all waves

we can investigate the influence of the scale alone. Inserting typical values ($U'=5$ m. sec.$^{-1}$, $v_{2\,max}=v'_{max}=10$ m. sec.$^{-1}$, $\phi=45°$ N., $\sin \alpha=10^{-1}$, $\sigma=4$) we can plot the expression (4.19) as a function of n. This is done in figure 7, where we also have multiplied by the area to obtain a unit comparable with the units in figures 6 and 7. We obtain a spectrum with a broad maximum around $n=8$. It is not too difficult to imagine that this spectrum would change into one with a structure similar to those in figures 6 and 7 when the standard values of $v_{2\,max}$ and v'_{max} were replaced by observed values. As mentioned before this would tend to give a maximum for $n=2$ or 3 and $n=6$ or 7. We may therefore say that *linear adiabatic* theory accounts for the gross features of the spectra obtained for January and April, although there are too many factors ($v_{2\,max}$, v'_{max}, and α) to make a close comparison.

Returning now to the nature of the spectra, we concluded that the maximum appearing for $n=6$ or 7 could be ascribed to the unstable baroclinic waves. In the preceding paragraphs we also pointed to the possibility that the maximum for $n=2$ or 3 could appear because of the rather great amplitude in the meridional winds for these wave numbers, if we made a comparison with an *adiabatic, linear* theory. The following question may now be asked: Would the energy conversion spectra be radically different if external effects (heating, friction) could be taken into account? Suppose for a moment that the spectrum would be changed only slightly. This would mean that the ultra-long waves ($n=1$, 2, and 3) would be self-maintaining, having an energy conversion which takes place on the same scale, which then would balance the frictional dissipation. If on the other hand, heating, for instance, will produce a system of vertical motions which are correlated with temperatures in such a way that the energy conversion is greatly reduced, we will have to postulate another mechanism responsible for the maintenance of the kinetic energy of these long waves against frictional dissipation. One possible mechanism would be a transfer of kinetic energy from higher to lower wave numbers through non-linear interaction, a mechanism which certainly must be operating in the atmosphere. It has in fact been shown by Fjørtoft [4] that a transfer of this nature takes place in a two-dimensional, non-divergent fluid. The quasi-barotropic character of the atmosphere makes it likely that the same mechanism to some extent is operating in the real atmosphere.

A definite answer to the question stated above is not easy to give, mainly because the distribution of heat sources and sinks is not known with any great accuracy. The present knowledge should, however, be sufficient to discuss at least the order of magnitude of the effect. The following section will deal with this question.

5. ON THE INFLUENCE OF DIABATIC HEATING ON THE ENERGY CONVERSION

In this section we shall first estimate the vertical velocities due to a reasonable distribution of heat sources and sinks. Next, we shall use the distribution of the vertical velocities to estimate the correction in the energy conversion.

Very little is known about the distribution of the heat sources and sinks in the vertical direction. We shall in the following consider a component of the heating function dQ/dt, which is the heating per unit mass and unit time prescribed by the formula:

$$\frac{dQ}{dt} = r\left(\frac{p}{p_0}\right)^\delta \sin m\,x \,. \qquad (5.1)$$

The main assumption made in (5.1) is that the vertical variation of dQ/dt can be assumed to be a power function of pressure. The exponent δ determines the decrease of the heating with height. Especially on the large scale it is reasonable to assume that the main part of the heating and cooling is due to interaction between the air and the underlying surface. The heating function ought therefore to decrease with height. The parameter δ has in the following computations been set equal to 3, which gives a rather rapid decrease with height, but the value of δ is open for discussion.

In (5.1) r measures the maximum intensity of the heating at the surface ($p=p_0$). Some recent computations of the vertically averaged heating makes it possible to determine r. The distribution of heating and cooling presented by Staff Members, Academia Sinica [17] shows in January a well-defined pattern on the ultra-large scale (essentially two waves) with an amplitude approximately 10^{-5} cal. gm.$^{-1}$ sec.$^{-1}$ for the vertically averaged heating. This corresponds to a total heating of 0.4185 kj. m.$^{-2}$ sec.$^{-1}$ The total maximum heating obtained from (5.1) is

$$H = \int_0^\infty \frac{dQ}{dt}\rho\,dz = \frac{1}{g}\int_0^{p_0} r\left(\frac{p}{p_0}\right)^\delta dp = \frac{p_0}{g}\frac{r}{\delta+1} \,. \qquad (5.2)$$

Equating these two we find that

$$r \simeq 0.17 \text{ kj. t.}^{-1} \text{ sec. }^{-1} \qquad (5.3)$$

If, on the other hand, we take the values used by Smagorinsky [15] we find that he considers a value of 0.3 cal. cm.$^{-2}$ min.$^{-1}=\frac{1}{2}\times 0.4185$ kj. m.$^{-2}$ sec.$^{-1}$ as a representative value in winter, although an overestimate in summer. As seen, this value is only half the value computed by the Staff Members, Academia Sinica, and would correspond to $r \simeq 0.08$ kj. t.$^{-1}$ sec.$^{-1}$ Our computations are, however, linear in r, and it will be easy to find the corrections due to the assumed intensity of the heating.

The author, in collaboration with Dr. N. A. Phillips and in connection with other problems, has recently made a computation of the heating for the month of January. It is hoped that these computations can be described in detail later. It suffices here to say that the heating was computed from the thermal vorticity equation in the sta-
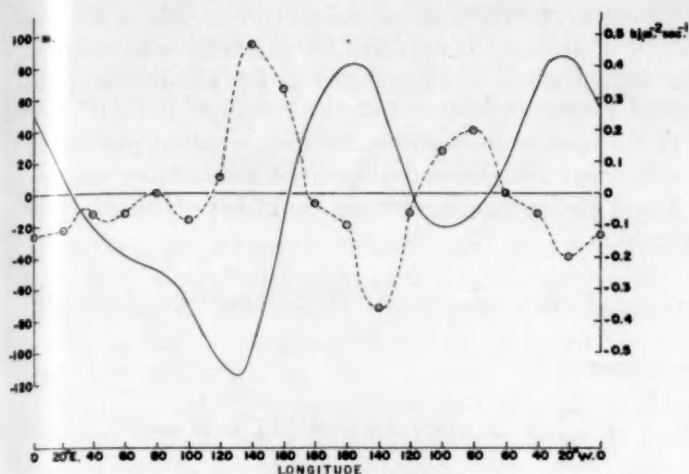
FIGURE 8.—The solid curve is the profile of the mean relative topography along 50° N. for the normal maps of January given as departures from the mean value (left scale). The dashed curve gives the latitudinal distribution of heat sources and sinks computed from the same normal maps (right scale).

tionary case in a two-parameter model paying attention to the influence of mountains and surface friction. The two-parameter model that was used was carefully constructed using the scheme described by Eliassen [3]. The normal maps prepared by Jacobs [6], Wege [20], and U.S. Weather Bureau [19] for the surfaces 1000, 850, 700, 500, 300, 200, and 100 mb. were used to define the average height field $\bar{z}$ and the thermal field h. The heating derived this way for 50° N. is reproduced in figure 8 together with the mean temperature field h.

The result of the computation is in many respects similar to the one obtained by Staff Members, Academia Sinica, although the maximum heating and cooling in our computation appears a little more toward the west than in theirs. The maxima are of the same order of magnitude.

The vertical motions produced by the heating and cooling may be found from the ω-equation. Including the diabatic heating in the thermodynamic energy equation we arrive at an ω-equation of the form:

$$\sigma \nabla^2 \omega + f_0^2 \frac{\partial^2 \omega}{\partial p^2} = \frac{\partial}{\partial p} \left(\mathbf{V} \cdot \nabla \eta \right) - \nabla^2 \left(\mathbf{V} \cdot \nabla \frac{\partial \phi}{\partial p} \right) - \frac{R}{C_p} \frac{1}{p} \nabla^2 \left(\frac{dQ}{dt} \right). \tag{5.4}$$

We are here interested in only the vertical motions due to heating and cooling and shall consequently consider the following equation:

$$\sigma \nabla^2 \omega + f_0^2 \frac{\partial^2 \omega}{\partial p^2} = -\frac{R}{C_p} \frac{1}{p} \nabla^2 \left(\frac{dQ}{dt} \right). \tag{5.5}$$

In the solution of (5.5) we shall assume that $\sigma = a/p^2$. For the goodness of this approximation see a paper by the author [22]. A solution to (5.5) may now be written in the

form

$$\omega(x, p) = F(p) \sin mx \tag{5.6}$$

where $F(p)$ will have to satisfy the equation

$$f_0^2 \frac{d^2 F}{dp^2} - m^2 \frac{a}{p^2} F = \frac{R}{C_p} m^2 \frac{r}{p_0^\delta} p^{\delta-1}. \tag{5.7}$$

Solutions to the homogeneous part of this equation are of the form p^α. Inserting this function in the homogeneous equation corresponding to (5.7) we find that α has to satisfy the equation

$$\alpha^2 - \alpha - \frac{m^2 a}{f_0^2} = 0 \tag{5.8}$$

giving the two solutions

$$\alpha_{1,2} = \frac{1}{2} \left(1 \pm \sqrt{1 + 4am^2/f_0^2} \right). \tag{5.9}$$

We find further that $F(p) = Bp^\epsilon$ is a solution to the nonhomogeneous equation provided

$$\epsilon = \delta + 1, \quad B = \frac{R}{C_p} \frac{m^2 r}{p_0^\delta} \frac{1}{f_0^2 \delta(\delta+1) - m^2 a}. \tag{5.10}$$

The complete solution may therefore be written:

$$F(p) = Bp^{\delta+1} + C_1 p^{\alpha_1} + C_2 p^{\alpha_2}. \tag{5.11}$$

The two integration constants C_1 and C_2 are determined from the boundary conditions $\omega = 0$ for $p = 0$ and $p = p_0$, giving $C_2 = 0$ and

$$C_1 = -Bp_0^{\delta+1-\alpha_1}. \tag{5.12}$$

The complete solution is therefore

$$F(p) = Bp_0^{\delta+1} \left[\left(\frac{p}{p_0} \right)^{\delta+1} - \left(\frac{p}{p_0} \right)^{\alpha_1} \right]. \tag{5.13}$$

$F(p)$ gives the vertical distribution of the vertical velocity, when it is a maximum. This distribution is given in figure 9, where we have used the following parameters: $f_0 = 10^{-4}$ sec.$^{-1}$, $a = 10^4$m.^{2} sec.$^{-2}$, $r = 0.08$kj.t.$^{-1}$ sec.$^{-1}$, $m = 0.45 \times 10^{-6}$m.$^{-2}$ (corresponding to two waves around the hemisphere).

Our next problem is to find the energy conversion due to this vertical velocity. The most critical feature here is of course in which way the temperature (thickness) patterns are arranged relative to the heat sources and sinks and therefore also to the diabatic vertical motion. Let us write the component of the thickness field as

$$h = h_a \sin (mx + \Delta) \tag{5.14}$$

where h_a is the amplitude of the thickness field and Δ the phase-lag between the heat source and the thickness field. Note that Δ is positive if the thickness field is lagging behind the heat source field. The diabatic vertical
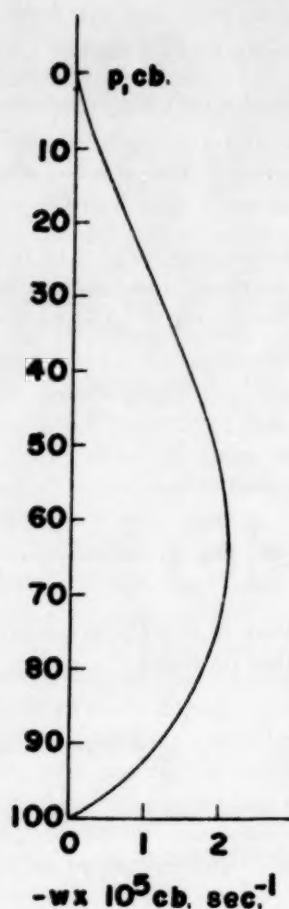
FIGURE 9.—Vertical profile of vertical velocity caused solely by heating.

velocity may be written

$$\omega = \omega_a \sin (mx + \pi) \qquad (5.15)$$

where ω_a now is positive.

The energy conversion per unit area due to diabatic heating may then be computed from the expression

$$\frac{1}{L} \{P, K\} = -\frac{32}{21} \frac{1}{L} \int_0^L \omega h \, dx \qquad (5.16)$$

which reduces to

$$\frac{1}{L} \{P, K\} = \frac{16}{21} \omega_a h_a \cos \Delta. \qquad (5.17)$$

In estimating Δ it is important to note that the computations of heat sources and sinks show that the atmosphere is heated where it is cold and cooled where it is warm. This is seen from figure 8 where the heating is approximately 180° out of phase with the thickness pattern. The Academia Sinica computation shows about the same although the phase difference here is smaller.

It seems therefore safe to conclude that cos Δ for the month of January is negative for the large-scale motion. The amplitude h_a was computed as the amplitude of the second Fourier component in the thickness in figure 8.

If the heat sources and sinks were situated just below the thermal troughs and ridges, we would have cos $\Delta = -1$ and the energy conversion could be estimated to be ($h_a \simeq 50$ m.)

$$\{P, K\}_{(2), \text{ diab.}} \simeq -9 \times 10^{-4} \text{ kj. m.}^{-2} \text{ sec.}^{-1} \qquad (5.18)$$

as compared to

$$\{P, K\}_{(2), \text{ adiab.}} \simeq +1.4 \times 10^{-4} \text{ kj. m.}^{-2} \text{ sec.}^{-1} \qquad (5.19)$$

Although (5.18) may be an overestimate due to the assumption that cos $\Delta = -1$ and further to the uncertainty of the intensity and position of the heat sources and sinks, it is safe to conclude that the large energy conversion found by the adiabatic computation in winter is not real, but that the heating and cooling produce a system of vertical motion which is correlated with the mean temperature in such a way that the energy conversion from potential energy to kinetic energy is greatly reduced or perhaps even takes the opposite sign.

If this conclusion is right, it also follows that the very long waves must receive the necessary amount of kinetic energy to balance the frictional dissipation in other ways than through energy conversions from the potential energy. One possibility is, as mentioned before, that non-linear interaction between shorter and longer waves transfers energy to the long waves. This apparently means that it is necessary to consider the changes in the shorter waves in order to predict changes on the larger scale. This conclusion, if true, makes the prediction of the large-scale motion extremely difficult.

Another conclusion of importance for even short-range prediction is that any baroclinic numerical prediction model, which does not include the effect of diabatic heating, apparently converts too much potential energy into kinetic energy on the very large scale. For this reason alone it seems important to incorporate large-scale heat sources and sinks in a baroclinic model.

It should also be mentioned that diabatic heating may modify the energy spectra on the smaller scale, although the main effect there would be heating due to condensation rather than interaction with the underlying surface. The greater part of the condensation in winter is connected with the traveling waves ($n = 6$ or 8). Here, however, it is most likely that the diabatic heating will work in the opposite direction because a release of condensation heat can be of significance only if a considerable amount of moisture is available, and this seems to be the case only in a warm air mass. For this scale we may therefore expect that the vertical motions produced by the heating are

positively correlated with the thickness. A qualitative argument of this type indicates that the energy conversion on the scale $n=6$ or 8 may be greater than indicated in figures 5 and 6.

6. GENERAL CONCLUSIONS

On the basis of computations of energy conversions from potential to kinetic energy for individual days it was found that each individual day gave a positive conversion of potential to kinetic energy. The mean conversions for the months of January and April were 15.6×10^{-4} kj. m.$^{-2}$ sec.$^{-1}$ and 10×10^{-4} kj. m.$^{-2}$ sec.$^{-1}$, respectively. Estimates of the frictional dissipation based on these computations agree fairly well with values obtained by Pisharoty from independent data. It is found that energy conversion in the meridional planes is small in magnitude compared to the conversion in the zonal planes. The computations further show that the weak meridional circulation consists of the classical three-cell pattern. A difference between January and April is found with respect to energy conversions in the meridional planes. The meridional circulation in January has a positive energy conversion, while it is negative in April. This seems to be connected with a less well-defined direct circulation in the low and high latitudes in April.

It is further found that the energy conversion gets smaller and smaller as time progresses in the present JNWP forecasts, verifying an earlier observation that the phase-lag between the temperature and pressure fields becomes small too rapidly in these forecasts. The mean meridional circulation is maintained in the forecasts although there seems to be a shift of the pattern toward the north.

The energy conversion for different wave numbers is computed in section 4. It is found that an adiabatic, frictionless computation shows two maxima for the wavelengths corresponding to 2 and 6 or 7 waves around the hemisphere.

In section 5 it is shown that the maximum, which appears for the very long waves, most likely would disappear if heat sources and sinks could be taken into account. It seems therefore that the very long waves will receive the main part of their kinetic energy through a non-linear interaction with the shorter waves.

7. ACKNOWLEDGMENTS

REFERENCES

1. D. Brunt, *Physical and Dynamical Meteorology*, Cambridge University Press, London, 1941.
2. J. Charney, "Dynamic Forecasting by Numerical Process," *Compendium of Meteorology*, American Meteorological Society, Boston, Mass., 1951, pp. 470–482.
3. A. Eliassen, "A Procedure for Numerical Integration of the Primitive Equations of the Two-Parameter Model of the Atmosphere," *Final Report* Contract AF 19(604)–1286, Dept. of Meteorology, University of California at Los Angeles, 1956, 53 pp.
4. R. Fjørtoft, "On the Changes of the Spectral Distribution of Kinetic Energy for Two-Dimensional Non-Divergent Flow," *Tellus*, vol. 5, No. 3, Aug. 1953, pp. 225–230.
5. W. L. Gates et al., "Results of Numerical Prediction with the Barotropic and Thermotropic Atmospheric Models," *Geophysical Research Papers* No. 46, U.S. Air Force, Cambridge Research Center, Aug. 1955, 107 pp.
6. I. Jacobs, "5- bzw. 40-jährige Monatsmittel der absoluten Topographien der 1000 mb, 850 mb, 500 mb, und 300 mb Flächen sowie der relativen Topographien 500/1000 mb und 300/500 mb über der Nordhemisphäre und ihre monatlichen Änderungen, Pt. 2," *Meteorologische Abhandlungen*, Band IV, Heft 2, Institut für Meteorologie und Geophysik der Freien Universität, Berlin, 1958, 121 pp.
7. E. N. Lorenz, "The Basis for a Theory of the General Circulation," *Final Report*, Contract AF 19(222)–153, Massachusetts Institute of Technology, 1954, pp. 522–534.
8. E. N. Lorenz, "Available Potential Energy and the Maintenance of the General Circulation," *Tellus*, vol. 7, No. 2, May 1955, pp. 157–167.
9. M. Margules, "Über die Energie der Stürme," *Jahrbuch 1903*, Appendix, Centralamt für Meteorologie und Geodynamik, Wien, 1905.
10. E. Palmén, Personal communication.
11. P. R. Pisharoty, "The Kinetic Energy of the Atmosphere," *Final Report*, Contract AF 19(122)–48, Dept. of Meteorology, University of California at Los Angeles, 1954, 140 pp.
12. N. A. Phillips, "Energy Transformations and Meridional Circulations Associated with Simple, Baroclinic Waves in a Two-Level, Quasi-Geostrophic Model," *Tellus*, vol. 6, No. 3, Aug. 1954, pp. 273–286.
13. N. A. Phillips, "General Circulation of the Atmosphere: A Numerical Experiment," *Quarterly Journal of the Royal Meteorological Society*, vol. 82, No. 352, Apr. 1956, pp. 123–164.
14. B. Saltzman, "Equations Governing the Energetics of the Larger Scales of Atmospheric Turbulence in the Domain of Wave Number," *Journal of Meteorology*, vol. 14, No. 6, Dec. 1957, pp. 513–523.
15. J. Smagorinsky, "The Dynamical Influence of Large-Scale Heat Sources and Sinks on the Quasi-Stationary Mean Motions of the Atmosphere," *Quarterly Journal of the Royal Meteorological Society*, vol. 97, No. 341, July 1953, pp. 342–366.
16. J. Smagorinsky, "On the Numerical Integration of the Primitive Equations of Motion for Baroclinic Flow in a Closed Region," *Monthly Weather Review*, vol. 86, No. 12, Dec. 1958, pp. 457–466.
17. Staff Members, Academia Sinica, "On the General Circulation over Eastern Asia (III)," *Tellus*, vol. 10, No. 3, Aug. 1958, pp. 299–312.
18. P. D. Thompson, "Statistical Aspects of the Dynamics of Quasi-Nondivergent and Divergent Baroclinic Models," *C.-G. Rossby Memorial Volume*, Stockholm, 1959.

19. U.S. Weather Bureau, "Normal Weather Charts for the Northern Hemisphere," *Technical Paper* No. 21, Washington, D.C., 1952.

20. K. Wege, *Mean Monthly Contours, Temperature, and Isotachs at 200, 100, and 50 mb 1949–53*, Freien Universität, Berlin, 1957. (Reprinted by U.S. Air Weather Service, Technical Support Division, Rhein/Main Air Base, Germany.)

21. A. Wiin-Nielsen, "On Certain Integral Constraints for the Time-Integration of Baroclinic Models," *Tellus*, vol. 11, No. 1, Feb. 1959, pp. 45–59.

22. A. Wiin-Nielsen, "On Barotropic and Baroclinic Models with Special Emphasis on Ultra-Long Waves," *Monthly Weather Review*, vol. 87, No. 5, May 1959, pp. 171–183.

23. R. M. White and B. Saltzman, "On Conversions between Potential and Kinetic Energy in the Atmosphere," *Tellus*, vol. 8, No. 3, Aug. 1956, pp. 357–363.

CORRECTION

Monthly Weather Review, vol. 87, July 1959, p. 281: In column 2, line 2, the vertical motion value should be ± 1 mm./sec.

NUMERICAL INTEGRATION OF THE PRIMITIVE EQUATIONS ON THE HEMISPHERE

NORMAN A. PHILLIPS

Massachusetts Institute of Technology, Cambridge, Mass.

ABSTRACT

A 48-hr. forecast for the entire Northern Hemisphere of a barotropic hydrostatic atmosphere is made with the "primitive equations." Overlapping Mercator and stereographic grids are used, together with the finite-difference scheme proposed by Eliassen. Initial data corresponded to a Haurwitz-type pattern of wave number 4. The initial wind field was nondivergent and the initial geopotential field satisfied the balance equation. The computations seem to be stable and well behaved, except for two small temporary irregularities. The amplitude of the gravity-inertia waves present in the forecast geopotential field is about 1/30 that of the large-scale field. It can be shown that this is due to the neglect, in the initial data, of the quasi-geostrophically conditioned divergence field. The computational technique itself therefore does not give any unreal prominence to the "meteorological noise." The computational characteristics and stability criterion of the Eliassen finite-difference system are investigated for a linearized version of the equations.

1. INTRODUCTION

The so-called "primitive equations" have not been used much in numerical forecasting because of two main difficulties. First, if the initial wind and pressure fields are not known accurately, artificially large gravity waves will appear in the forecast [3,8]. Secondly, the computational stability criterion for these equations requires a time step of at most 10 minutes compared to the 40- to 60-minute time step allowed in the geostrophic system. The development of larger and faster computing machines is rapidly eliminating the second difficulty. It also seems probable that a gradual improvement of the rawin and radiosonde network, combined with special analyses of the initial data, may go far toward solving the first difficulty. A stable and accurate computation scheme is then all that will be required to take advantage of the more faithful reproduction of atmospheric processes which is possible with the primitive equations. (The geostrophic system not only fails at short wavelengths [2], but also loses its special prognostic value at extremely long wavelengths [1]. In addition, certain important effects such as the horizontal variation of static stability cannot be incorporated into the geostrophic system [10,11].)

There are two aspects to the design of a good computation scheme for the primitive equations: (a) the finite difference equivalents of the partial differential equations themselves, and (b) the formulation of lateral boundary conditions. Eliassen [6] and Platzmann [15] have discussed the former and have arrived at a finite-difference scheme for the primitive equations which is more efficient than the type of finite-differences currently used in geo-

strophic forecasts. However, boundary conditions for the solution of the primitive equations by finite-differences also require considerable care in their formulation, as has been pointed out, for example, by Smagorinsky [17]. This problem is greatly simplified if the lateral boundary of the forecast region can be placed on the equator, where suitable symmetry assumptions can be imposed on the forecast variables. Although the equator as a boundary is readily fitted into either a spherical coordinate system or into coordinates on a Mercator map, both of these coordinate systems have singularities at the North Pole.

In an attempt to avoid this problem, the writer has suggested the simultaneous use of a Mercator map in low latitudes and a stereographic projection in high latitudes [13]. However, the computational stability of this system is then too complicated a question to be examined by mathematical analysis. A numerical test of the scheme has therefore been made and the results are described in this paper. The equations used were those appropriate to a homogeneous incompressible atmosphere moving hydrostatically. The initial wind and pressure (geopotential) fields were defined mathematically, rather than being obtained from a weather map. The computations are therefore a test only of this method of computation, and do not purport to answer the question of whether adequate initial data can be defined for real forecasts.

2. THE EQUATIONS OF MOTION

The horizontal equations of motion in spherical coordinates, assuming hydrostatic balance and neglecting friction, can be written

$$a\ddot{\lambda} \cos \theta = 2a\dot{\theta}(\dot{\lambda}+\Omega) \sin \theta - \frac{1}{a \cos \theta}\frac{\partial \phi}{\partial \lambda}, \tag{1}$$

$$a\ddot{\theta} = -a\dot{\lambda} \cos \theta(\dot{\lambda}+2\Omega) \sin \theta - \frac{1}{a}\frac{\partial \phi}{\partial \theta}. \tag{2}$$

Here λ=longitude, θ=latitude, a=radius of the earth, Ω=angular velocity of the earth, and ϕ=the geopotential of an isobaric surface. The dot (˙) is the substantial derivative:

$$(\dot{\ }) = \frac{d}{dt} = \frac{\partial}{\partial t}+\dot{\lambda}\frac{\partial}{\partial \lambda}+\dot{\theta}\frac{\partial}{\partial \theta}+\dot{p}\frac{\partial}{\partial p}. \tag{3}$$

Here p is the pressure, and it is clear that the independent variables which are being used are λ, θ, p, and t. Equations (1) and (2) do not contain the Coriolis term $2\Omega\dot{a} \cos \theta$ or the inertia terms $2\dot{\lambda}\dot{a} \cos \theta$ and $2\dot{a}\dot{\theta}$. They must be neglected for consistency when the hydrostatic approximation is used, since their counterparts in the third equation of motion have also been neglected.

Applying these equations to the motion of an incompressible homogeneous atmosphere with a free surface we find that (1) and (2) carry over as written, if ϕ is set equal to gz, where z is the variable depth of the atmosphere. (3) becomes simpler by the disappearance of the $\partial/\partial p$ operator, since $\dot{\lambda}$ and $\dot{\theta}$ may be taken as independent of the vertical coordinate p. The only other equation needed is the continuity equation, which for this atmosphere can be written

$$\frac{\partial \phi}{\partial t} = -\text{div }(\phi\mathbf{v}) = -\frac{\partial(\phi\dot{\lambda})}{\partial \lambda} - \sec \theta \frac{\partial(\phi\dot{\theta} \cos \theta)}{\partial \theta}. \tag{4}$$

(Here g, the acceleration of gravity, has been assumed constant, and variations in a have also been neglected.)

We now define the map coordinates for the Mercator and stereographic projections as follows:

$$\text{Mercator:}\begin{cases} X=a\lambda, \\ Y=-a \ln h, \end{cases} \tag{5}$$

$$\text{Stereographic:}\begin{cases} x=2ah \cos \lambda, \\ y=2ah \sin \lambda, \end{cases} \tag{6}$$

$$h=\cos \theta(1+\sin \theta)^{-1}. \tag{7}$$

Following the procedure outlined in [13], we define

$$U=a\dot{\lambda} \cos \theta = M^{-1}\dot{X},$$

$$V=a\dot{\theta}=M^{-1}\dot{Y},$$

$$M=\sec \theta, \tag{8}$$

so that U and V are the horizontal velocity components along the X- and Y-axes of the Mercator projection. M is the scale factor for this projection.

For the stereographic projection we define

$$u=-a\dot{\lambda} \cos \theta \sin \lambda-a\dot{\theta} \cos \lambda=m^{-1}\dot{x},$$

$$v=a\dot{\lambda} \cos \theta \cos \lambda- a\dot{\theta} \sin \lambda=m^{-1}\dot{y}, \tag{9}$$

$$m=2(1+\sin \theta)^{-1},$$

so that u and v are the horizontal velocity components along the x- and y-axes of the stereographic projection. m is the scale factor for this projection. (U, V) and (u, v) are related by the expressions:

$$u=-U \sin \lambda-V \cos \lambda,$$

$$v=U \cos \lambda-V \sin \lambda. \tag{10}$$

The two horizontal equations of motion and the continuity equation (4) can now be written in the map coordinates:

$$\frac{\partial U}{\partial t} = -M\left[\frac{\partial \phi}{\partial X}+U\frac{\partial U}{\partial X}+V\frac{\partial U}{\partial Y}\right]+V \sin \theta\left[2\Omega+\frac{MU}{a}\right], \tag{11}$$

$$\frac{\partial V}{\partial t} = -M\left[\frac{\partial \phi}{\partial Y}+U\frac{\partial V}{\partial X}+V\frac{\partial V}{\partial Y}\right]-U \sin \theta\left[2\Omega+\frac{MU}{a}\right], \tag{12}$$

$$\frac{\partial \phi}{\partial t} = -M^2\left[\frac{\partial}{\partial X}\left(\frac{U\phi}{M}\right)+\frac{\partial}{\partial Y}\left(\frac{V\phi}{M}\right)\right], \tag{13}$$

$$\frac{\partial u}{\partial t} = -m\left[\frac{\partial \phi}{\partial x}+u\frac{\partial u}{\partial x}+v\frac{\partial u}{\partial y}\right]+v\left[2\Omega \sin \theta-\frac{(xv-yu)}{2a^2}\right], \tag{14}$$

$$\frac{\partial v}{\partial t} = -m\left[\frac{\partial \phi}{\partial y}+u\frac{\partial v}{\partial x}+v\frac{\partial v}{\partial y}\right]-u\left[2\Omega \sin \theta-\frac{(xv-yu)}{2a^2}\right], \tag{15}$$

$$\frac{\partial \phi}{\partial t} = -m^2\left[\frac{\partial}{\partial x}\left(\frac{u\phi}{m}\right)+\frac{\partial}{\partial y}\left(\frac{v\phi}{m}\right)\right]. \tag{16}$$

The Mercator equations (11)–(13) are equivalent to the stereographic equations (14)–(16) and also to the spherical equations (1)–(4).

Equations (11)–(13) have a singularity at the pole where $M=\sec \theta$ becomes infinite. Equations (14)–(16) have a singularity at the south pole, where $m=2(1+\sin \theta)^{-1}$ becomes infinite. As described in [13], the finite-difference solution of (11)–(16) is to be carried out over one hemisphere by applying (11)–(13) on a Mercator grid in low latitudes and (14)–(16) on a stereographic grid in high latitudes. The Mercator grid should extend from the equator to about 43° latitude, with the stereographic grid being responsible for the area poleward of this latitude (see fig. 1). The singularities are thereby avoided

3. FINITE-DIFFERENCE EQUATIONS

To solve (11)–(16) we use the finite-difference scheme proposed by Eliassen [6] for the primitive equations. To describe this scheme in the present context we must define *four* lattices on the Mercator map and *four* on the stereographic. First we introduce the constant space increment Δ to be used on both maps:

$$\Delta = \frac{2\pi a}{P}, \quad (P = \text{integer}). \qquad (17)$$

The finite difference coordinates will be (p, q) and (i, j):

$$\text{Mercator:} \begin{cases} X = (p - p_0)\Delta, \ p = 0, 1, \ldots, P+1, \\ Y = (q - q_0)\Delta, \ q = 0, 1, \ldots, Q+1. \end{cases} \qquad (18)$$

$$\text{Stereographic:} \begin{cases} x = (i - i_0)\Delta, \ i = 0, 1, \ldots, I+1, \\ y = (j - j_0)\Delta, \ j = 0, 1, \ldots, I+1. \end{cases}$$

(It will be convenient to take I as an even integer.) The Mercator grid is therefore rectangular $(P+2) \times (Q+2)$ and the stereographic grid is square $(I+2) \times (I+2)$. The numbers (p_0, q_0) and (i_0, j_0) determine the location on the map of the origin of each grid. We define the four Mercator and the four stereographic grids (denoted by $A, B, C,$ and D) by the four sets of values of (p_0, q_0) and (i_0, j_0) shown in table 1. Figure 2 shows the relative orientation on the map of the points on the four grids which have the same subscripts (p, q) or (i, j). From the definition of X in (5) and Δ in (17), it can be seen that the points $p=0$ and $p=1$ on the Mercator grid are identical with the points $p=P$ and $p=P+1$, respectively. These extra points are included in the grids merely for convenience in solving the equations.

The Eliassen computation scheme is obtained by defining the variables (U, V, ϕ) or (u, v, ϕ) on the grids as follows. At time $t = \Delta t, 2\Delta t, 3\Delta t, \ldots, n\Delta t$, U (or u) is represented at the lattice points of grid B; V (or v) is represented at the lattice points of grid C; and ϕ (or ϕ) is represented at the lattice points of grid A. At the intermediate times, $t = 1/2\Delta t, 3/2\Delta t, 5/2\Delta t, \ldots, (n+1/2)\Delta t$, U (or u) is represented on grid C, V (or v) on grid B, and ϕ (or ϕ) on grid D. Such an arrangement is much more efficient than when all quantities (e.g. U, V, and ϕ)
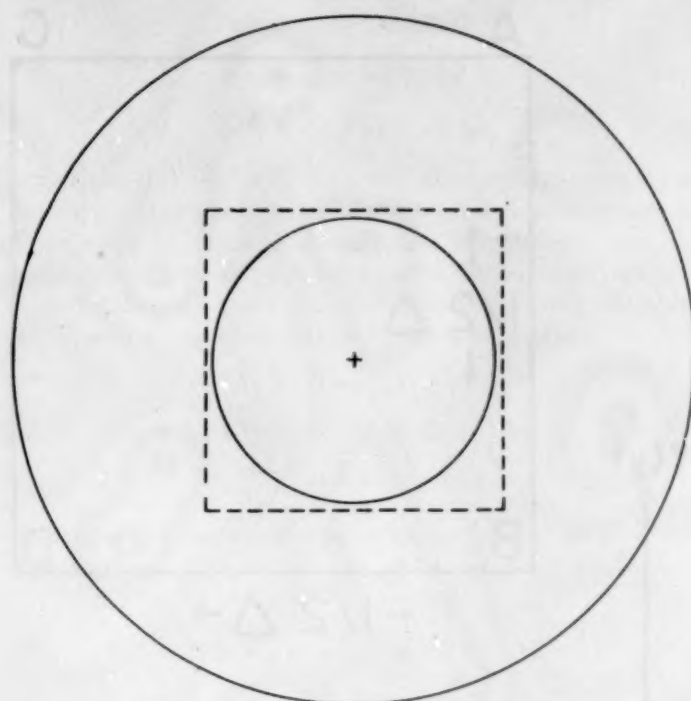

FIGURE 1.—General orientation of Mercator and stereographic grids, shown on a stereographic projection. The stereographic grid covers the square dashed area centered at or near the pole. A Mercator grid covers the area between the equator (outer circle) and the inner circle.

are defined at *each* point of a single grid at *all* time steps. (Note the discussion of fig. 5 in section 7.) For convenience in notation we will hereafter use a prime superscript ($U', V', \phi', u', v', \phi'$) to indicate the quantities defined at the intermediate times $t = 1/2\Delta t, \ldots, (n+1/2)\Delta t$. For example, ϕ_{pqn} will indicate $\phi[X = (p-1/2)\Delta, Y = (q-1/2)\Delta, t = n\Delta t]$ (stored on grid A, where $p_0 = 1/2$ and $q_0 = 1/2$). ϕ'_{pqn}, however, will indicate $\phi[X = p\Delta, Y = (q-1)\Delta, t = (n+1/2)\Delta t]$ (stored on grid D, where $p_0 = 0$ and $q_0 = 1$.)

For convenience in writing the finite-difference equivalents of (11)–(16) we also introduce the notation δ_p and σ_p for the following operators:

$$\delta_p S_{pq} = S_{pq} - S_{p-1\,q},$$

$$\sigma_p S_{pq} = \tfrac{1}{2}(S_{pq} + S_{p-1\,q}).$$

Similar definitions hold for δ_q, σ_q, δ_i, δ_j, σ_i, and σ_j. Finally, to eliminate unnecessary repetition of letter subscripts in the formulae, a quantity such as S_{pq} will be written simply as S_{00}, $S_{p\,q+1}$ as S_{01}, etc.

In the Eliassen scheme, the six equations (11)–(16) applied to the Mercator and stereographic projections, result in 12 finite-difference equations. Quantities appearing on the right side of these equations are understood to have the time subscript n in all cases. The symbol f

TABLE 1.—*Origin coordinates of the four grids used in the Eliassen finite-difference scheme.*

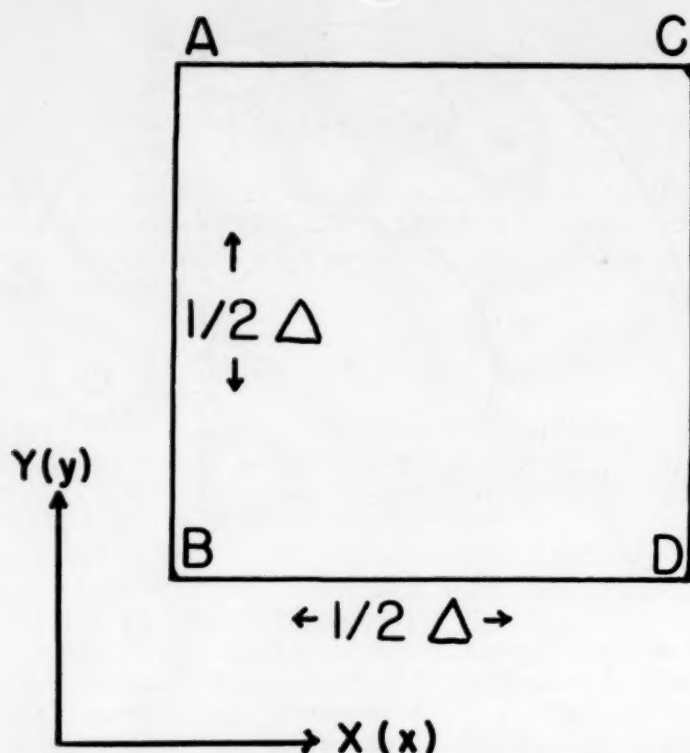| Grid	p_0	q_0	i_0	j_0
A	1/2	1/2	I/2+3/4	I/2+1/4
B	1/2	1	I/2+3/4	I/2+3/4
C	0	1/2	I/2+1/4	I/2+1/4
D	0	1	I/2+1/4	I/2+3/4

FIGURE 2.—Relative positions on a Mercator (or stereographic) map of the points on the four grids A, B, C, and D which have the same finite-difference coordinates p, q (or i, j).

is used for the Coriolis parameter $2\Omega \sin \theta$. f and the scale factors M and m are identified by additional subscripts A, B, C, or D denoting the grid on which they are located.

$$U'_{00n} - U'_{00\,n-1} = -M_{00C}\left(\frac{\Delta t}{\Delta}\right)\{\delta_p\phi_{10} + \sigma_q[(\sigma_p U_{11})(\delta_p U_{11})]$$
$$+ V'_{00}\delta_q\sigma_p U_{11}\} + V'_{00}\Delta t f_{00C}\left[1 + \left(\frac{M_{00C}}{2\Omega a}\right)\sigma_p\sigma_q U_{11}\right], \quad (19)$$

$$V'_{00n} - V'_{00\,n-1} = -M_{00B}\left(\frac{\Delta t}{\Delta}\right)\{\delta_q\phi_{00} + U_{00}\delta_p\sigma_q V_{00}$$
$$+ \sigma_p[(\sigma_q V_{00})(\delta_q V_{00})]\} - U_{00}\Delta t f_{00B}\left[1 + \left(\frac{M_{00B}}{2\Omega a}\right)U_{00}\right], \quad (20)$$

$$\phi'_{00n} - \phi'_{00\,n-1} = -M^2_{00D}\left(\frac{\Delta t}{\Delta}\right)$$
$$\left\{\delta_p\left[U_{10}\sigma_q\left(\frac{\phi_{10}}{M_{10A}}\right)\right] + \delta_q\left[V_{00}\sigma_p\left(\frac{\phi_{10}}{M_{10A}}\right)\right]\right\}, \quad (21)$$

$$U_{00\,n+1} - U_{00n} = -M_{00B}\left(\frac{\Delta t}{\Delta}\right)\{\delta_p\phi'_{00} + \sigma_q[(\sigma_p U'_{00})(\delta_p U'_{00})]$$
$$+ V'_{00}\delta_q\sigma_p U'_{00}\} + V'_{00}\Delta t f_{00B}\left[1 + \left(\frac{M_{00B}}{2\Omega a}\right)\sigma_p\sigma_q U'_{00}\right], \quad (22)$$

$$V_{00\,n+1} - V_{00n} = -M_{00C}\left(\frac{\Delta t}{\Delta}\right)\{\delta_q\phi'_{01}$$
$$+ U'_{00}\delta_p\sigma_q V'_{11} + \sigma_p[(\sigma_q V'_{11})(\delta_q V'_{11})]\}$$
$$- U'_{00}\Delta t f_{00C}\left[1 + \left(\frac{M_{00C}}{2\Omega a}\right)U'_{00}\right], \quad (23)$$

$$\phi_{00\,n+1} - \phi_{00n} = -M^2_{00A}\left(\frac{\Delta t}{\Delta}\right)$$
$$\left\{\delta_p\left[U'_{00}\sigma_q\left(\frac{\phi'_{01}}{M_{01D}}\right)\right] + \delta_q\left[V'_{01}\sigma_p\left(\frac{\phi'_{01}}{M_{01D}}\right)\right]\right\}, \quad (24)$$

$$u'_{00n} - u'_{00\,n-1} = -m_{00C}\left(\frac{\Delta t}{\Delta}\right)$$
$$\{\delta_i\phi_{10} + \sigma_j[(\sigma_i u_{11})(\delta_i u_{11})] + v_{00}\delta_j\sigma_i u_{11}\} + v_{00}\Delta t$$
$$\left\{f_{00C} - \frac{\Delta}{2a^2}[(i-i_0)v_{00} - (j-j_0)\sigma_i\sigma_j u_{11}]\right\}, \quad (25)$$

$$v'_{00n} - v'_{00\,n-1} = -m_{00B}\left(\frac{\Delta t}{\Delta}\right)$$
$$\{\delta_j\phi_{00} + u_{00}\delta_i\sigma_j v_{00} + \sigma_i[(\sigma_j v_{00})(\delta_j v_{00})]\} - u_{00}\Delta t$$
$$\left\{f_{00B} - \left(\frac{\Delta}{2a^2}\right)[(i-i_0)\sigma_i\sigma_j v_{00} - (j-j_0)u_{00}]\right\}, \quad (26)$$

$$\phi'_{00n} - \phi'_{00\,n-1} = -m^2_{00D}\left(\frac{\Delta t}{\Delta}\right)\left\{\delta_i\left[u_{10}\sigma_j\left(\frac{\phi_{10}}{m_{10A}}\right)\right]$$
$$+ \delta_j\left[v_{00}\sigma_i\left(\frac{\phi_{10}}{m_{10A}}\right)\right]\right\}, \quad (27)$$

$$u_{00\,n+1} - u_{00n} = -m_{00B}\left(\frac{\Delta t}{\Delta}\right)$$
$$\{\delta_i\phi'_{00} + \sigma_j[(\sigma_i u'_{00})(\delta_i u'_{00}) + v'_{00}\delta_j\sigma_i u'_{00}\} + v'_{00}\Delta t$$
$$\left\{f_{00B} - \left(\frac{\Delta}{2a^2}\right)[(i-i_0)v'_{00} - (j-j_0)\sigma_i\sigma_j u'_{00}]\right\}, \quad (28)$$

$$v_{00\,n+1} - v_{00n} = -m_{00C}\left(\frac{\Delta t}{\Delta}\right)$$

$$\{\delta_j\phi'_{01} + u'_{00}\delta_i\sigma_j v'_{11} + \sigma_i[(\sigma_j v'_{11})(\delta_j v'_{11})]\} - u'_{00}\Delta t$$

$$\left\{f_{00C} - \left(\frac{\Delta}{2a^2}\right)[(i-i_0)\sigma_i\sigma_j v'_{11} - (j-j_0)u'_{00}]\right\}, \quad (29)$$

$$\phi_{00\,n+1} - \phi_{00n} = -m_{00A}^2\left(\frac{\Delta t}{\Delta}\right)$$

$$\left\{\delta_i\left[u_{00}\sigma_j\left(\frac{\phi'_{01}}{m_{01D}}\right)\right] + \delta_j\left[v'_{01}\sigma_i\left(\frac{\phi'_{01}}{m_{01D}}\right)\right]\right\}. \quad (30)$$

The first six of these refer to the Mercator grid, the second six to the stereographic grid. [The numbers i_0 and j_0 have the value $(I/2+1/4)$ in equations (25) and (29), and the value $(I/2+3/4)$ in equations (26) and (28).]

The order of solving the equations is (19)–(21) and (25)–(27), followed by (22)–(24) and (28)–(30). From the form of the equations it is clear that they can all be solved on the *interior* points of the grids ($p=1, 2, 3, \ldots, P$; $q=1, 2, \ldots, Q$) and ($i=1, 2, 3, \ldots, I$; $j=1, 2, \ldots, I$). A further inspection will show that the left ($i=0$ or $p=0$) and top ($j=I+1$ or $q=Q+1$) boundaries can be computed with equations (21) and (27); the left and bottom ($j=0$ or $q=0$) boundaries can be computed in (19), (23), (25), and (29); the bottom and right ($i=I+1$ or $p=P+1$) boundaries in (24) and (30); and right and top boundaries can be computed in (20), (22), (26), and (28). The remaining boundary values (in general, two adjacent boundaries for each grid of data) must be computed by other means than (19)–(30) in order to regenerate the complete grids of data at each time step. The procedure that was used here is described in the next section.

The system (19)–(30), although written in a form suggestive of uncentered differences, actually uses centered differences. (The truncation error can be expressed as a series in Δ^2 and $(\Delta t)^2$.) A special starting procedure must be used to get the primed variables at time $t=1/2\Delta t$. In the test computation described in this paper, an uncentered step was used to get the initial values of U', V', etc. at $n=0(t=1/2\Delta t)$. U', V', etc. were initially known at $t=0$. Their value at $t=1/2\Delta t(n=0)$ was obtained from (19)–(21) and (25)–(27) by temporarily replacing Δt by $1/2\Delta t$ on the right side of those equations, and the second term on the left side of those equations by $U'(t=0)$, etc.

4. BOUNDARY CONDITIONS

We examine first the equatorial boundary condition, which is used to specify the variables on the bottom row of the Mercator grid ($q=0$). If the motion at one instant $t=t_0$ over the *entire* sphere satisfies the symmetry conditions

$$\dot\lambda(\lambda,\theta, t_0) \equiv \dot\lambda(\lambda,-\theta, t_0),$$

$$\dot\theta(\lambda, \theta, t_0) \equiv -\dot\theta(\lambda,-\theta, t_0), \quad (31)$$

$$\phi(\lambda, \theta, t_0) \equiv \phi(\lambda,-\theta, t_0),$$

equations (1)–(4) will preserve this symmetry for all future t. It is clear that under these conditions computations need be made over only one hemisphere, and the appropriate boundary conditions at the equator may be inferred directly from (31). For the Mercator variables U, V, and ϕ, equation (31) may then be written

$$U(X, Y, t) \equiv U(X,-Y, t),$$

$$V(X, Y, t) \equiv -V(X,-Y, t), \quad (32)$$

$$\phi(X, Y, t) \equiv \phi(X,-Y, t).$$

As applied to the six Mercator grids of data, we find that this implies

$$U'_{p0} \equiv U'_{p1} \quad (q_0=1/2)$$
$$V'_{p0} \equiv -V'_{p2} \quad (q_0=1)$$
$$\phi'_{p0} \equiv \phi'_{p2} \quad (q_0=1)$$
$$U_{p0} \equiv U_{p2} \quad (q_0=1)$$
$$V_{p0} \equiv -V_{p1} \quad (q_0=1/2)$$
$$\phi_{p0} \equiv \phi_{p1} \quad (q_0=1/2)$$

(33)

(It can be shown from equations (20) that V'_{p1} will always be zero.)

The left and right boundaries of the Mercator grid are easily handled by applying the cyclic boundary condition that the point ($p=0, q=q$) is identical to the point ($p=P, q=q$) and the point ($p=P+1, q=q$) is identical with the point ($p=1, q=q$).

On the top boundary ($q=Q+1$) of the Mercator grids, V', ϕ', and U can be forecast by (20), (21), and (22). The variables U', V, and ϕ at $q=Q+1$ cannot be forecast by (19), (23), and (24), however. (Note that these latter quantities are stored on grids A and C, which have the smaller value of q_0 in table 1, and therefore the most northerly position of the four Mercator grids, as shown by fig. 2.) In addition, boundary values of the six stereographic variables u', v', ϕ', u, v, and ϕ must be obtained on the boundaries listed in the third column of table 2. (These are the only points on those grids which cannot be forecast from the finite difference equations (25)–(30).) In [13] a method was outlined for obtaining these boundary values by interpolation from the associated grid. For example, a Mercator boundary value of ϕ is interpolated from the corresponding stereographic grid of ϕ values, and vice versa. In the case of the velocity components (U, V) and (u, v) the relations (10) must of course be used to supplement the interpolation process, as indicated in the last column of table 2.

TABLE 2.—*Interpolation of boundary values between the Mercator and stereographic grids*

Variable	Grid	Boundaries needed	Interpolated from grid—
U''	Merc. (C)	$q=Q+1$	Ster: u' (C) and v' (P)
ϕ	Merc. (A)	$q=Q+1$	Ster: ϕ (A)
V	Merc. (C)	$q=Q+1$	Ster: u (B) and v (C)
u'	Ster. (C)	$i=I+1$ and $j=I+1$	Merc: U'' (C) and V'' (B)
v'	Ster. (B)	$i=0$ and $j=0$	Merc: U'' (C) and V'' (B)
ϕ'	Ster. (D)	$i=I+1$ and $j=0$	Merc: ϕ' (D)
u	Ster. (B)	$i=0$ and $j=0$	Merc: U (B) and V (C)
v	Ster. (C)	$i=I+1$ and $j=I+1$	Merc: U (B) and V (C)
ϕ	Ster. (A)	$i=0$ and $j=I+1$	Merc: ϕ (A)

In order to perform the boundary interpolations in a "neat" manner it is necessary that the individual Mercator and stereographic grids overlap one another to a certain extent. To make this statement more precise, let us define the *sub-boundary* points of a grid as those points located next to a boundary (i.e. where $q=Q$ on the Mercator grids or the points with $i=1$ or I, $j=1$ or I on the stereographic grids). We require that the points $q=Q+1$ on Mercator grids A and C (for which $Y=(Q+1/2)\Delta$) lie *north* of the most northerly sub-boundary point of the stereographic grids. This latter point is located at a distance $r=\sqrt{x^2+y^2}=(\Delta/4)[(2I-3)^2+1]^{1/2}$ from the pole on the stereographic projection. The boundary values of U', ϕ, and V required in table 2 can then be obtained by interpolation on the stereographic grids without reference to the boundary values on those grids. Referring to (5), (6), and (7) we find that Y and r are related by the equation $\exp(-Y/a)=r/2a$. We must therefore have

$$\exp[-(2Q+1)\pi/P]<(\pi/4P)[(2I-3)^2+1]^{1/2}. \quad (34)$$

Another constraint which should be satisfied is that the northernmost boundary point on a stereographic grid (at $r=(\Delta/4)[(2I+1)^2+1]^{1/2}$) be located *south* of the southernmost sub-boundary point on the Mercator grids (located at $q=Q$ on grids B and D, with $Y=(Q-1)\Delta$). The boundary values of u', v', ϕ', u, v, and ϕ required in table 2 on stereographic boundaries can then be obtained by interpolation on the Mercator grids without reference to any Mercator boundary points. This leads to a second inequality:

$$\exp[-(2Q-2)\pi/P]<(\pi/4P)[(2I+1)^2+1]^{1/2}. \quad (35)$$

If Q and I are not large enough to satisfy both (34) and (35), the interpolation process becomes more complicated and will undoubtedly lead to mathematical instabilities.

The values of P, Q, and I used in this test computation were

$$P=80, \ Q=12, \ I=22.$$

This gives a grid increment $\Delta=2\pi a/P$ of 500.4 km. The corresponding distances on the earth varied from 500.4 km. at the pole ($m=1$) and equator ($M=1$) to a minimum of about 350 km. ($m\sim M\sim 1.4$) in middle latitudes. It should be pointed out that horizontal space differences in the system (19)—(30) are taken over the distance Δ, rather than 2Δ as is customary at present in numerical weather prediction.

It might be thought that *all* boundary values on the stereographic grids, including those which can be forecast by (19)–(24), could be obtained by interpolation. This procedure was in fact tried in a preliminary computation. (It is logically easier from the point of view of the machine program to interpolate all four boundaries on the stereographic grids than it is to do only those listed in table 2.) However, the results of this preliminary computation were quite unsatisfactory compared to the results described in this paper. When interpolation was done on all boundaries, the flow patterns tended to move at different speeds on the two grids, and discontinuities developed near the grid boundaries.

The details of the interpolation process were as described in [13]. Computation of one interpolated boundary value took less machine time than did a computation of one of the equations (19)–(30) at one pont. Thus, only about 5 percent of the total computation time was spent on the boundary computations.

5. INITIAL DATA

The initial velocity and geopotential fields for this test computation were defined by a flow pattern of the type treated by Haurwitz [7]. The initial velocity field **v** was non-divergent, and given by the stream function ψ:

$$\psi=-a^2\omega\sin\theta+a^2 K\cos{}^R\theta\sin\theta\cos R\lambda. \quad (36)$$

ω, K, R, and a (radius of the earth) are constants. As shown by Haurwitz, a flow pattern like this will, in a *non-divergent* barotropic atmosphere, move from west to east without change of shape with the angular velocity ν:

$$\nu=\frac{R(3+R)\omega-2\Omega}{(1+R)(2+R)}. \quad (37)$$

The equations used in the computations, however, are not those for a non-divergent atmosphere, but for one with a free surface. (37) will therefore only be satisfied approximately. The presence of divergence in the barotropic atmosphere, will, as is well known, slow up the rate of progression of the flow pattern, especially for small values of the wave number R [16].

In the non-divergent barotropic atmosphere treated by Haurwitz, the pressure field (p/ρ) associated with the initial flow pattern (36) can be readily determined by integration of the equations of motion (1)–(2), using the

angular phase velocity ν to evaluate $\partial\psi/\partial t$. We replace p/ρ by ϕ. The distribution of ϕ obtained in this way is given in the following formulae:

$$\phi=\phi_0+a^2A(\theta)+a^2B(\theta)\cos R\lambda+a^2C(\theta)\cos 2R\lambda, \quad (38)$$

$$A(\theta)=\tfrac{1}{2}\omega(2\Omega+\omega)c^2+\tfrac{1}{4}K^2c^{2R}[(R+1)c^2$$

$$+(2R^2-R-2)-2R^2c^{-2}],$$

$$B(\theta)=\frac{2(\Omega+\omega)K}{(R+1)(R+2)}\,c^R[(R^2+2R+2)-(R+1)^2c^2],$$

$$C(\theta)=\tfrac{1}{4}K^2c^{2R}[(R+1)c^2-(R+2)],$$

$$c=\cos\theta.$$

Both (36) and (38) satisfy the symmetry conditions (31). ϕ_0 in (38) is an arbitrary constant which will determine the average height of the free surface in the atmospheric model being used here. This in turn will determine the speed of propagation of gravity-inertia waves and also the order of magnitude of the divergence in the model (div $\mathbf{v}=-\phi^{-1}d\phi/d\,t$).

The initial distribution of ψ and ϕ used for the computations was that given by (36) and (38), with the following values for the constants:

$$\omega=K=7.848\times10^{-6}\ \text{sec.}^{-1}\ (\sim0.1\Omega),$$

$$R=4$$

$$\phi_0=9.8\ (8\times10^3)\ \text{m.}^2\ \text{sec.}^{-2}.$$

These values for ω and K give rise to large velocities, the maximum values of $a\dot\lambda\cos\theta\ (=-a^{-1}\partial\psi/\partial\theta)$ and $a\dot\theta[=(a\cos\theta)^{-1}\partial\psi/\partial\lambda]$ being about 99 and 65 m. sec.$^{-1}$. Figure 3 shows the distribution of the initial height of the free surface $z=\phi/g$. The total variation of 3.5 km. in z is several times as large as the typical variation in the height of the 500-mb. surface in winter.

It is clear from the way in which this initial ϕ-field was determined, that ψ and ϕ together satisfy the so-called "balance equation" [3]:

$$\nabla\cdot F\nabla\psi+\nabla\cdot\mathbf{A}=\nabla^2\phi,$$

where

$$F=\sin\theta\left(2\Omega-\frac{1}{a^2\cos\theta}\frac{\partial\psi}{\partial\theta}\right),$$

$$A_\lambda=a^{-3}\sec\theta J\left(\frac{\psi,\partial\psi/\partial\theta}{\lambda,\theta}\right)=-\mathbf{v}\cdot\nabla(a\dot\lambda\cos\theta), \quad (39)$$

$$A_\theta=-a^{-3}\sec\theta J\left(\frac{\psi,\sec\theta\partial\psi/\partial\lambda}{\lambda,\theta}\right)=-\mathbf{v}\cdot\nabla(a\dot\theta).$$
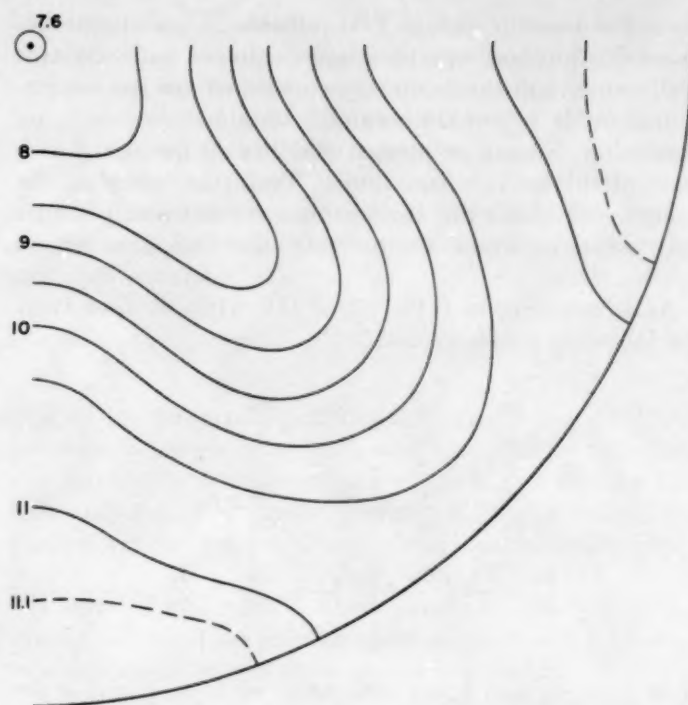

FIGURE 3.—Initial distribution of the height of the free surface, shown on a stereographic projection. Only one octant is shown, the pattern repeating in the other three octants of the hemisphere. The outer circle is the equator. Isolines are labeled in km.

(∇ is the horizontal gradient operator on the sphere.) The advantage of using ϕ- and ψ-fields which satisfy (39) is that $\partial(\text{div }\mathbf{v})/\partial t$ is initially zero. According to Charney [3], this will result in much smaller amplitudes of the gravity-inertia waves than would appear if only the geostrophic relation were used to relate the initial ϕ- and $\mathbf{v}$-fields to one another.

It is of some interest to examine the vorticity field corresponding to (36):

$$f+\zeta=2(\omega+\Omega)\sin\theta-(1+R)(2+R)K\cos^R\theta\sin\theta\cos R\lambda$$

$$\sim f[1.1-1.5\cos^4\theta\cos 4\lambda]. \quad (40)$$

(We have here introduced the value $R=4$ and the approximate values $\omega=K\sim0.1\Omega$). Because of the large value of K there are four regions of negative absolute vorticity in low latitudes. These regions extend poleward to a latitude of about 22° where $\cos^4\theta=(1.1)/(1.5)$. The minimum value of $f+\zeta$ (reached at $\theta\sim7.25°$) is only about -0.09Ω, however.

6. COMPUTATIONAL STABILITY

The computational stability of the finite-difference equations derived in section 3, with the boundary condi-

tions discussed in section 4, is difficult to investigate because the forecast equations are nonlinear with variable coefficients, and the boundary conditions are not simple. Considerable information can be obtained, however, by examining the computational stability of linearized versions of the forecast equations. To further simplify the analysis we make the coefficients constant and consider only solutions which are periodic in x and y, as on an infinite plane.

As an analogue to (11)–(13) or (14)–(16), we then treat the following simple system:

$$\frac{\partial u}{\partial t} = -\frac{\partial \phi}{\partial x} - u_0 \frac{\partial u}{\partial x} - v_0 \frac{\partial u}{\partial y} + fv \tag{41}$$

$$\frac{\partial v}{\partial t} = -\frac{\partial \phi}{\partial y} - u_0 \frac{\partial v}{\partial x} - v_0 \frac{\partial v}{\partial y} - fu \tag{42}$$

$$\frac{\partial \phi}{\partial t} = -\Phi \left(\frac{\partial u}{\partial x} + \frac{\partial v}{\partial y} \right) - u_0 \frac{\partial \phi}{\partial x} - v_0 \frac{\partial \phi}{\partial y}. \tag{43}$$

Here f, u_0, v_0, and Φ are constants, while u, v, and ϕ are perturbation quantities. (43) could also include a term $-(u \partial \Phi/\partial x + v \partial \Phi/\partial y) = -f(uv_0 - vu_0)$. It also is omitted for simplicity. For disturbances of the form $\exp i\ (\mu t + ax + by)$, (41)–(43) are satisfied by three solutions for the frequency μ:

$$\mu_1 = -(au_0 + bv_0),$$
$$\mu_2 = \mu_1 + [f^2 + \Phi(a^2 + b^2)]^{1/2}, \tag{44}$$
$$\mu_3 = \mu_1 - [f^2 + \Phi(a^2 + b^2)]^{1/2}.$$

μ_1 corresponds to a geostrophic, non-divergent wave, while μ_2 and μ_3 are gravity-inertia waves.

We now write (41)–(43) in finite-differences, using the same basic scheme that was used to get (19)–(24) and (25)–(30). We introduce solutions of the form $\Psi_{pq} = \exp i\ (\alpha p + \beta q)$, where $\alpha = a\Delta, \beta = b\Delta$, and p and q are the finite-difference space coordinates. For convenience in the analysis we introduce the following new quantities:

$$u_{pqn} = U_n \sqrt{\Phi} \Psi_{pq},$$
$$v_{pqn} = V_n \sqrt{\Phi} \Psi_{pq} e^{1/2i(\alpha+\beta)},$$
$$\phi_{pqn} = H_n \Phi \Psi_{pq} e^{1/2i\beta},$$
$$u'_{pqn} = U'_n \sqrt{\Phi} \Psi_{pq} e^{1/2i(\alpha+\beta)},$$
$$v'_{pqn} = V'_n \sqrt{\Phi} \Psi_{pq},$$
$$\phi'_{pqn} = H'_n \Phi \Psi_{pq} e^{1/2i\alpha},$$
$$W = \frac{\Delta t}{\Delta} \left(u_0 \sin \frac{\alpha}{2} \cos \frac{\beta}{2} + v_0 \cos \frac{\alpha}{2} \sin \frac{\beta}{2} \right),$$

$$F = \frac{1}{2} f \Delta t,$$
$$M = \left(\frac{\Delta t}{\Delta} \right) \sqrt{\Phi} \sin \frac{\alpha}{2},$$
$$N = \left(\frac{\Delta t}{\Delta} \right) \sqrt{\Phi} \sin \frac{\beta}{2}. \tag{45}$$

U_n, V_n, . . ., H'_n are now the non-dimensional amplitudes of the perturbations and are functions of time $(n\Delta t)$. We also define the following matrices:

$$Z_n = \begin{bmatrix} U_n \\ V_n \\ H_n \end{bmatrix}, \quad Z'_n = \begin{bmatrix} U'_n \\ V'_n \\ H'_n \end{bmatrix},$$

$$G = -2i \begin{bmatrix} W & iF & M \\ -iF & W & N \\ M & N & W \end{bmatrix}. \tag{46}$$

The Eliassen-grid finite-difference equivalents of (41)–(42) can then be written (after some algebra) in the following compact form:

$$Z'_n = Z'_{n-1} + GZ_n,$$
$$Z_n = Z_{n-1} + GZ'_{n-1}. \tag{47}$$

An equation for Z (or Z') alone is easily obtained from these:

$$Z_{n+1} - 2LZ_n + Z_{n-1} = 0. \tag{48}$$

Here L is the matrix $I + \frac{1}{2} G^2$, where I is the unit matrix. L is Hermitian (l_{ij} is the complex conjugate of l_{ji}) and therefore has three real eigenvalues λ_j and three orthogonal eigenvectors ϵ_j. Further calculation shows that the λ's are equal to $\cos \xi$, where ξ can assume any one of the three values

$$\sin\left(\frac{1}{2} \xi_1 \right) = W,$$
$$\sin\left(\frac{1}{2} \xi_2 \right) = W - [F^2 + M^2 + N^2]^{1/2}, \tag{49}$$
$$\sin\left(\frac{1}{2} \xi_3 \right) = W + [F^2 + M^2 + N^2]^{1/2}.$$

Expanding Z_n now as a series in the orthogonal eigenvectors ϵ_j,

$$Z_n = \sum_{j=1}^{3} \delta_{jn} \epsilon_j,$$

we find that (48) leads to the following scalar equations for the δ_j:

$$\delta_{j\,n+1} - (2\cos\xi_j)\delta_{jn} + \delta_{j\,n-1} = 0,\ j=1,2,3. \tag{50}$$

The solutions for δ_{jn} are therefore

$$\delta_{jn} = \exp \pm (i\,n\xi_j), \tag{51}$$

where the three values of ξ_j are still given by (49). Computational stability is achieved by demanding that all ξ_j be real. Referring to (49) we see that this requires the following inequality to be satisfied:

$$|W \pm \sqrt{F^2+M^2+N^2}| < 1. \tag{52}$$

It should be noted that a weakening of this to permit the equality will allow $\cos\theta = -1$, whereupon (50) will contain an unstable solution of the form $\delta_n = n(-1)^n$.

Introducing the definitions of W, F, M, and N from (45), and taking the worst possible orientation for u_0 and v_0, the simplified computational stability criterion for this Eliassen grid system can finally be written:

$$\left(\frac{\Delta t}{\Delta}\right)\left[|\mathbf{v_0}| + \sqrt{\left(\frac{f\Delta}{2}\right)^2+\Phi}\right] < 1. \tag{53}$$

In this formula Δt and Δ are the time and space increments over which the partial derivatives with respect to t and x (or y) are expressed as finite differences. $|\mathbf{v_0}|$ is equal to $\sqrt{u_0^2+v_0^2}$. As is clear from the preceding analysis, the satisfaction of (53) will not necessarily insure the stability of a computation where the lateral boundary conditions are more complicated than the simple ones implied by (45). In such cases (53) is best thought of as a necessary, but not sufficient, condition for stability.

Criterion (53) allows a maximum time step of $\Delta t =$ 12.5 min. to be used in forecasting the flow pattern described in section 5. The test computations were made with a time step of (1/7) hr. $\sim$8.5 min. It took approximately 30 sec. on an IBM 704 to compute one time step; that is, to solve the 12 equations (19)–(30) at all points concerned, and to do the necessary boundary computations listed in table 2. A 24-hr. forecast therefore required about 84 minutes of computer time. (Checking of the results is not included in this figure.) Any further increase in computer speeds, say by a factor of 10, will certainly make it possible to use the primitive equations over an entire hemisphere for even a multi-level baroclinic atmosphere.

It is clear from (51) and (49) that the linearized finite-difference system (47) possesses *six* frequencies. The continuous system (41)–(43), on the other hand, possesses

only the *three* frequencies given in (44). It can be shown that three of the six frequencies in the finite-difference system are similar in form to the three continuous frequencies in (44), and that the remaining three finite-difference frequencies differ only by a reversal in the sign of the advection term W. These extra solutions are very similar to the "computational wave" which is present in the conventional way of solving the geostrophic vorticity equation [14].

7. RESULTS OF THE TEST COMPUTATION

A 48-hr. forecast was made from the initial wind and pressure fields given by (36) and (38). Since this forecast cannot be compared with either a real atmospheric flow pattern or a mathematically known solution, the results will be examined only from the following viewpoints:

a. Smoothness of the fields in space. In particular, the agreement between the stereographic and Mercator representations in the areas of overlap (see fig. 1).

b. Smoothness of the fields in time—the question of "meteorological noise."

Figure 4 shows the forecast field of $z = \phi/g$ at 48 hours, in the area covered by the stereographic A grid. The waves have moved about 18° to the east in approximate agreement with (37). Of special interest is the agreement between the stereographic isolines and the Mercator isolines (heavy dashed lines) in the area of overlap of the two grids. In general, the two sets of lines are both smooth. They agree with one another extremely well except for one area near the upper right corner and another smaller area near the lower left corner. The maximum value of the difference between the two grids of z-values in these areas is about 90 meters—about 1/20 of the maximum difference in z between a trough and ridge at the same latitude. The field of z on that portion of the Mercator grid not shown in figure 4 was very smooth, even in the low latitude regions where $f+\zeta$ was negative.

A severe test of the smoothness of the forecast z-field is shown in part A of figure 5. Here the quantity $-4z_{ij} + z_{i+1\,j} + z_{i\,j+1} + z_{i-1\,j} + z_{i\,j-1}$ at $t = 36$ hr. is plotted for an area centered near the North Pole. (Only the stereographic grid covers this region.) There is some tendency for a "checkerboard" pattern to appear, but it is not very pronounced.

Smagorinsky [17] and Hinkelmann [9] have made experimental forecasts with the primitive equations which were not based on the Eliassen type of finite-difference grid. In their scheme, only one grid is used (instead of the four grids described in section 3), and the geopotential and both velocity components are stored at all points of this single grid at all time steps. Time and space derivatives are expressed as centered finite differences over the intervals $2\,\Delta\,t$ and $2\,\Delta$, much as is done in the usual
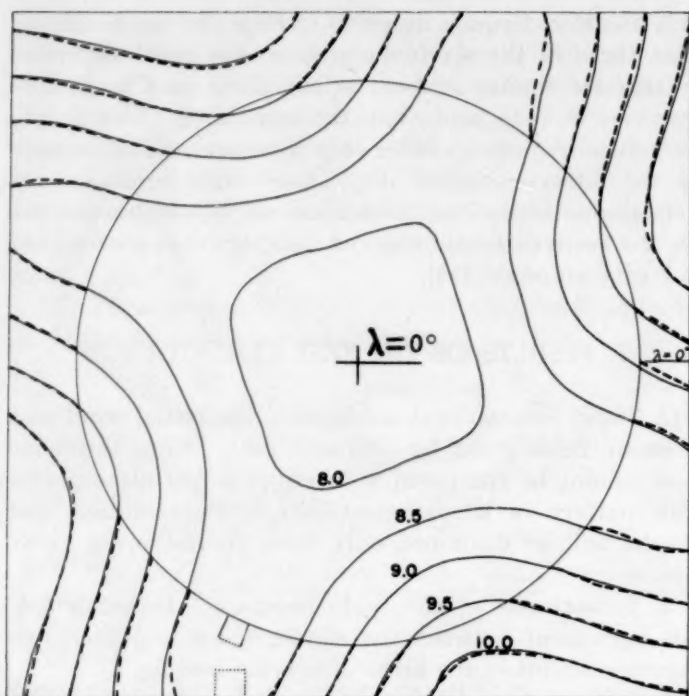
FIGURE 4.—The forecast field of z at 48 hours, drawn on a stereographic map, showing only the area covered by the stereographic grid A. Isolines are drawn at intervals of 500 m. Thin continuous isolines are drawn from the stereographic grid-point values (grid A). Heavy dashed isolines are drawn from the Mercator grid-point values (grid A). The Mercator grid A extended only in to the circle. The small dotted areas show the spacing of the lattice points on the Mercator and stereographic grids.

4	14	6	12	5	-1	12		2	22	-4	22	-4	19	2
5	0	11	5	5	15	10		19	-7	25	-14	22	-7	22
4	2	8	2	21	-4	10		-4	22	-4	27	-4	25	-4
6	17	0	11	1	17	-3		22	-14	27	-20	27	-14	22
5	1	14	3	13	10	13		-4	25	-4	27	-4	22	-4
5	9	5	10	8	4	7		22	-7	22	-14	25	-7	19
6	3	11	8	6	6	8		2	19	-4	22	-4	22	2

A   B

FIGURE 5.—Grid point values of the quantity $(-4z_{ij}+z_{i+1\ i}+z_{i-1\ j}+z_{i\ j+1}+z_{i\ j-1})$ at 36 hours for an area centered near the pole; (A) from the forecast made with the Eliassen grid system, (B) from a special forecast made with the finite-difference system used by Smagorinsky and Hinkelmann. Units are in tens of meters.

way of making numerical weather predictions with the geostrophic model [4]. In order to compare this method with the Eliassen method of solving the primitive equations, a special 36–hr. forecast was made with the appropriate difference equations from the same initial flow pattern. Figure 5 B shows the resulting field of $-4z_{ij}+z_{i+1\ j}+z_{i\ j+1}+z_{i-1\ j}+z_{i\ j-1}$ at 36 hr. from this special forecast. The *average* value of the plotted numbers is almost the same, 7.1 in figure 5A and 8.2 in figure 5B, but the range in the plotted values is 25 in figure 5A and 47 in figure 5B. The tendency to a checkerboard pattern is very marked in figure 5B. It is clear then that forecasts made this way will be much more irregular than those obtained with the Eliassen grid system.

The main purpose of the computation described in this paper was to test the computational stability of the overlapping stereographic-Mercator grids, since this feature of the computation was not amenable to the type of computational stability analysis carried out in section 6. Although the results shown in figure 4 certainly indicate that the scheme is at least reasonably stable, two small temporary "wiggles" did appear during the course of the forecast. They did not appear until after 24 hours, and as shown by figure 4, had practically disappeared again by 48 hours. They appeared only near the top boundary of the Mercator grid, the stereographic grid point values being quite smooth at all times. Figure 6 shows the detailed structure at 36 hours of the wiggle located near $\lambda = 56°$. The other irregularity was very similar and located exactly on the other side of the hemisphere, in the same part of the wave-like flow pattern.

Both of the irregularities seemed to be quasi-geostrophic in character, with the U and V components following the geopotential field shown in figure 6. The writer has not been able to isolate the cause of these two "errors," which, although small, disfigure what otherwise seems to be an excellent computation. Since they appear only on the Mercator grids, and in only two of the four waves, it is safe to conclude that they do not represent anything real, but represent rather some peculiar type of truncation error. In this connection it may be important to recall from section 6 that the Eliassen grid system does contain three false computational frequencies in addition to the three physical frequencies. Experience with the geostrophic vorticity equation has shown that such false frequencies frequently become important near boundaries.

In order to give an idea of the amount of "meteorological noise" present in the computations, a record of the height z at 2-hour intervals is shown in figure 7 for 3 selected points. (Unfortunately, a record of the forecast fields was printed out only every 2 hours=14 time steps.) Point I is located near the equator in one of the regions of negative $f+\zeta$. Point II is located initially in the trough at 46° N. near the top of the Mercator grid. (It is one of the points in figure 6, where it is marked II.) Point III

is located 175 km. from the North Pole. All three points have been purposely chosen in regions of small net changes in z (except for the last half of curve II), so that any small short-period oscillations will stand out clearly. Such oscillations are indeed present and evidently have an amplitude corresponding to a height change of ± 50 meters. For comparison, the maximum net 48-hr. change in z at any point was equal to ± 1450 meters—a value 29 times as large as the amplitude of the meteorological noise. Height tendencies measured over intervals of less than about 4 hours would therefore represent primarily "noise," and not the slower quasi-geostrophic changes.

This result—the presence of a small but noticeable inertia-gravity oscillation—is at first sight contrary to the results obtained from "balanced" initial data by Charney in [3]. In Charney's test computation with the primitive equations, no meteorological noise appeared at all when the initial wind and pressure fields satisfied the balance equation (39). The explanation for this difference is that Charney's initial flow pattern was a stationary wave, while the flow pattern used here is not stationary but moves slowly to the east. In a barotropic atmosphere a quasi-geostrophic wave has, as is well known, a small, but significant divergence field associated with it if the wave is not stationary. This divergence associated with the geostrophic wave disappears only if the wavelength happens to be such that the wave is stationary. Therefore, unless the initial wind field also has this small amount of divergence, the forecast must contain some high-frequency gravity-inertia oscillations ("noise") in addition to the low-frequency geostrophic motions.

From the linearized treatment of the noise problem by Hinkelmann in [8], it is possible to estimate the magnitude of the noise which is introduced by neglecting in the initial data the (small) divergence associated with a moving geostrophic wave. If c_1 and c_2 are the phase velocities of the geostrophic and gravity-inertia waves respectively, the fictitious gravity-inertia wave will have an amplitude in the geopotential ϕ approximately equal to (c_1/c_2) times the amplitude in ϕ of the quasi-geostrophic wave. For the example treated in this paper, (c_1/c_2) is about $1/30$, giving good agreement with the numerically computed amplitudes in ϕ of the two types of motion. There can be no doubt then that the numerically computed noise shown in figure 7 is due to the choice of initial data and is not caused by the numerical technique. The importance of including this geostrophically-conditioned divergence in the initial data for the primitive equations has also been demonstrated recently by Hinkelmann [9].

According to the theory of the geostrophic approximation as developed by Monin [12] (contained to some extent also in [5]), the second geostrophic approximation to the true wind is given by v_2, say, where the divergence of v_2 is precisely that divergence which appears (multiplied by f) in the usual geostrophic form of the vorticity equation,
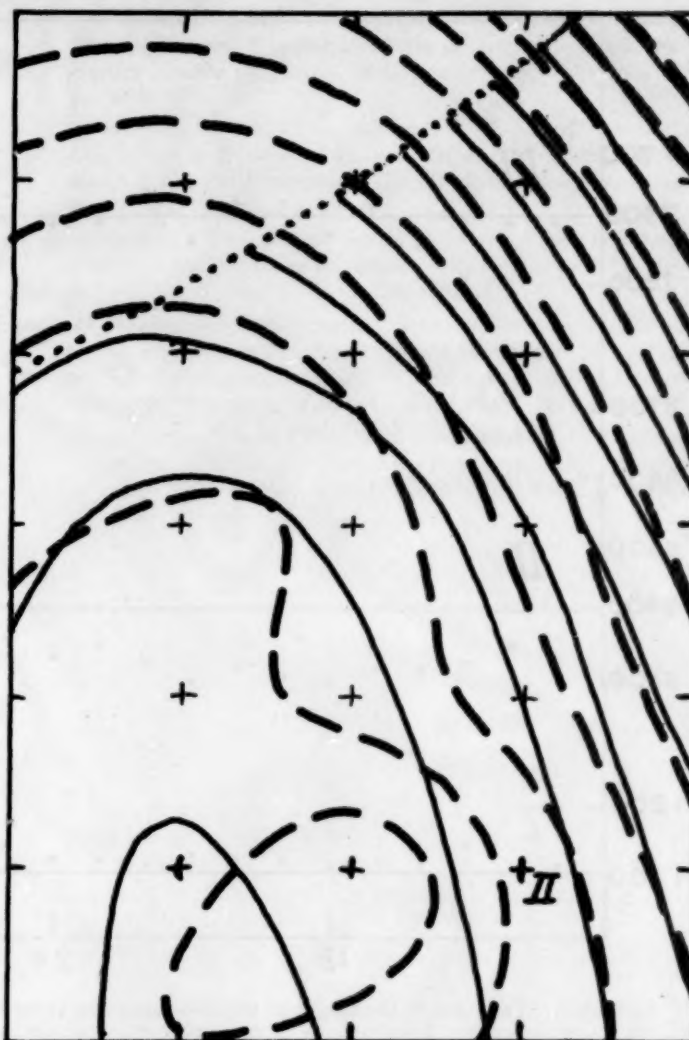

FIGURE 6.—Detailed structure of one of the two temporary irregularities which appeared on the Mercator grid. The isolines of z (for $t=36$ hours) are drawn on a Mercator projection, the small crosses being the points of Mercator grid A. The top of the figure is at $q=Q+1$. The heavy dashed isolines represent the Mercator analysis and the thin continuous lines an independent analysis of the corresponding stereographic grid. Both sets of isolines are drawn at intervals of 100 meters, the minimum value isolines in the upper right portion of the area being in both cases that for 8300 m. The grid point marked II is the point corresponding to curve II in figure 7.

and the vorticity of v_2 is given by an equation similar to the balance equation (39), but with the non-linear terms in ψ evaluated geostrophically. Evidently Charney [3] and Hinkelmann [9] have each tested separately the value of adding to the geostrophic wind a correction either for the vorticity or for the divergence. The elimination of noise in both of their results is due to the special choice of initial
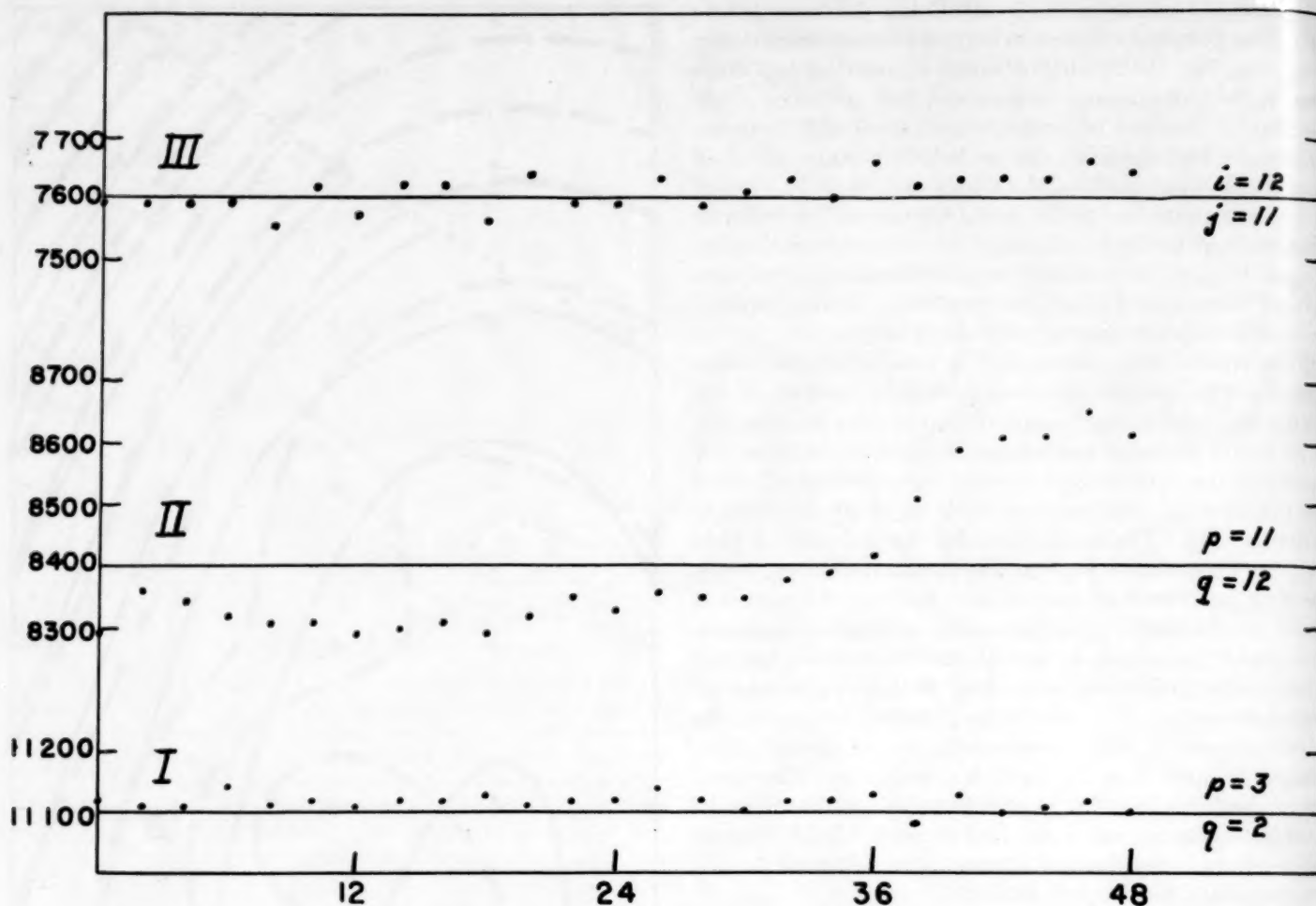
FIGURE 7.—Variation of the height of the free surface at three selected grid points, shown at 2-hour intervals.   Units are meters.

data used by each of them; in Charney's special test case the correction for divergence was unnecessary, as mentioned above, because the wave was stationary, while in Hinkelmann's special case the linear terms in (39) were not only much larger than the neglected non-linear terms, but the correction for divergence was quite important because of the very strong baroclinicity in the zonal flow.

ACKNOWLEDGMENTS

REFERENCES

1. A. P. Burger, "Scale Considerations of Planetary Motions of the Atmosphere," *Tellus*, vol. 10, No. 2, May 1958, pp. 195–205.
2. J. Charney, "On the Scale of Atmospheric Motions," *Geofysiske Publikasjoner*, vol. 17, No. 2, 1948, 17 pp.
3. J. Charney, "The Use of the Primitive Equations of Motion in Numerical Prediction," *Tellus*, vol. 7, No. 1, Feb. 1955, pp. 22–26.
4. J. Charney, R. Fjørtoft, and J. von Neumann, "Numerical Integration of the Barotropic Vorticity Equation," *Tellus*, vol. 2, No. 4, Nov. 1950, pp. 237–254.
5. A. Eliassen, "The Quasi-Static Equations of Motion with Pressure as Independent Variable," *Geofysiske Publikasjoner*, vol. 17, No. 3, 1949, 44 pp.
6. A. Eliassen, *A Procedure for Numerical Integration of the Primitive Equations of the Two-Parameter Model of the Atmosphere*, Scientific Report No. 4, on Contract AF 19(604)–1286, Dept. of Meteorology, Univ. of California at Los Angeles, 1956, 53 pp.

7. B. Haurwitz, "The Motion of Atmospheric Disturbances on the Spherical Earth," *Journal of Marine Research*, vol. 3, 1940, pp. 254–267.

8. K. Hinkelmann, "Der Mechanismus des meteorologischen Lärmes," *Tellus*, vol. 3, No. 4, Nov. 1951, pp. 285–296.

9. K. Hinkelmann, "Ein Numerisches Experiment mit der primitiven Gleichungen," *C.-G. Rossby Memorial Volume*, Esselte A.B., Stockholm, 1959.

10. G. Hollman, "Über prinzipielle Mängel der geostrophischen Approximation und die Einführung ageostrophischen Windkomponenten," *Meteorologische Rundschau*, vol. 9, Nos. 5/6, May/June 1956, pp. 73–78.

11. E. N. Lorenz, "Static Stability and Atmospheric Energy," *Scientific Report*, No. 9, on Contract AF 19(604)–1000, (General Circulation Project), Dept. of Meteorology, Massachusetts Institute of Technology, 1957, 41 pp.

12. A. S. Monin, "Izmeneniĭa Davleniĭa v Baroklinnoi Atmosfere," [Pressure Changes in a Baroclinic Atmosphere] *Izvestiĭa Akademiĭa Nauk SSSR, Ser. Geofiz.*, No. 4, Apr. 1958, pp. 497–514.

13. N. A. Phillips, "A Map Projection System Suitable for Large-Scale Numerical Weather Prediction," *Journal of the Meteorological Society of Japan*, 75th Anniversary Volume, 1957, pp. 262–267.

14. G. Platzman, "The Computational Stability of Boundary Conditions in Numerical Integration of the Vorticity Equation," *Archiv für Meteorologie, Geophysik, und Bioklimatologie*, Ser. A, vol. 7, 1954, pp. 29–40.

15. G. Platzman, "The Lattice Structure of the Finite-Difference Primitive and Vorticity Equations," *Monthly Weather Review*, vol. 86, No. 8, Aug. 1958, pp. 285–292.

16. C.-G. Rossby and collaborators, "Relation Between Variations in the Intensity of the Zonal Circulation of the Atmosphere and the Displacements of the Semi-Permanent Centers of Action," *Journal of Marine Research*, vol. 2, 1939, pp. 38–55.

17. J. Smagorinsky, "On the Numerical Integration of the Primitive Equations of Motion for Baroclinic Flow in a Closed Region," *Monthly Weather Review*, vol. 86, No. 12, Dec. 1958, pp. 457–466.

Weather Note

TORNADOES NEAR NAGS HEAD, N.C. JULY 1959

FRANK B. DINWIDDIE

Weather Bureau Cooperative Hurricane Reporting Observer, Nags Head, N.C

On July 10, 1959, at 1300 EST, a tornado was seen to form over the mile-wide barrier beach at Nags Head, N.C., a little less than a mile from the observer's house (fig. 1). The center of tropical storm Cindy was then about 75 miles to the west-northwest, moving northeastward. Surface conditions at the time were: wind south with gusts to 52 m.p.h., sea level pressure 29.79 inches, temperature 82° F., dewpoint 72° F., and cloud base level about 2250 feet. A loosely formed band of cumulus congestus was overhead, oriented southwest by south to northeast by north, and a heavy rain shower with no thunder was just passing over to the north (see fig. 2).

Suddenly a small cumulus, somewhat rectangular in outline, about a mile to the northwest and apparently detached from the cloud band, showed unusual though not violent agitation as a strong updraft accelerated in the body of the cloud and a small horizontal roll developed along the nearer edge (figs. 3 and 4). The whole system drifted rapidly toward the north-northeast with the gale then prevailing. After about 20 seconds the small roll cloud elongated southwestward beyond the end of the cumulus and a small almost vertical vortex cloud appeared near the ground. Immediately thereafter small filaments of cloud raced northeastward along the upper edge of the roll cloud (fig. 5). This is the only instance I have seen or known about of a horizontal roll cloud becoming a tornado, and I watched it with unbelieving amazement. The bottom of this roll cloud rolled toward the parent cumulus, which is opposite to the rotation of the typical thundersquall roll cloud.

Several seconds more and the roll cloud had elongated into a true funnel, wider than before, inclined upward toward the northeast, and joined by a rather sharp elbow to the slender nearly-vertical tube at its southwestern end. This latter cloud reached to the ground, rotated cyclonically, and soon developed a cylindrical sheath of flying sand around its base, as in figure 6. All these developments, from figure 3 to figure 6, were extremely rapid and probably did not require more than 30 or 35 seconds. Figure 6 is the situation about the time several buildings were severely damaged; wind damage was more apparent than low-pressure damage. One brick cabin had the roof
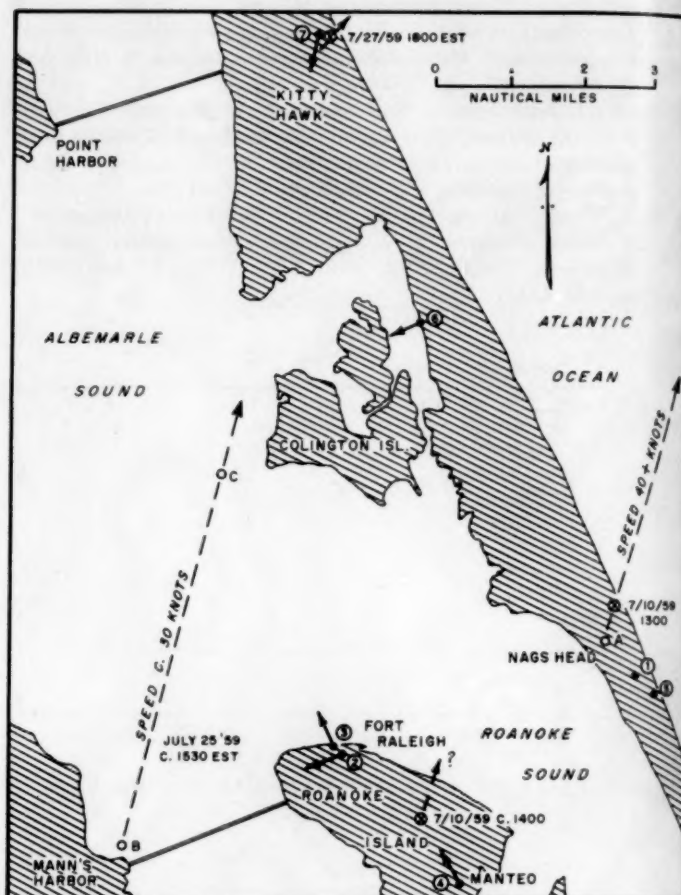

FIGURE 1.—Map showing locations of tornadoes and observers. Dashed arrows show estimated tracks of tornadoes or damaging winds.

X   Location of damage.
A   Location of tornadogenesis 7/10/59 (see also fig. 2).
B   Approximate location of tornado 7/25, first photo by Dan Morill.
C   Approximate location of tornado 10 min. after B, second photo by Dan Morill (fig. 9).
1   Location of F. B. Dinwiddie observing tornado of 7/10 (figs. 2–8).
2   Camera location and tornado bearing 7/25, first photo by Dan Morill.
3   Camera location and tornado bearing 7/25, second photo by Dan Morill (fig. 9).
4   Location and tornado bearing 7/25, Henry Eden.
5   Location 7/25 of anonymous viewer of tornado.
6   Location and tornado bearing 7/25 at time of dissolution, Mr. Morrison.
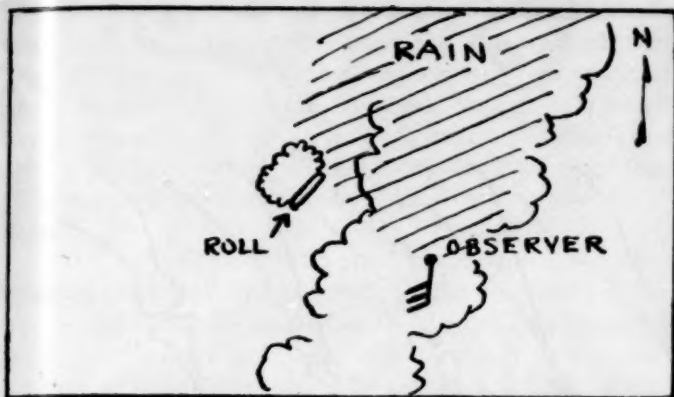7   Location and tornado bearing 7/25, James W. Pace and sketches (figs. 10–17).

FIGURE 2.—Plan view of position of observer in relation to rain shower and cumulus cloud which developed a tornado funnel, 1300 EST, July 10, 1959.

FIGURE 5.—Elongation of roll cloud beyond edge of cumulus and appearance of small vertically-oriented vortex cloud near the ground.
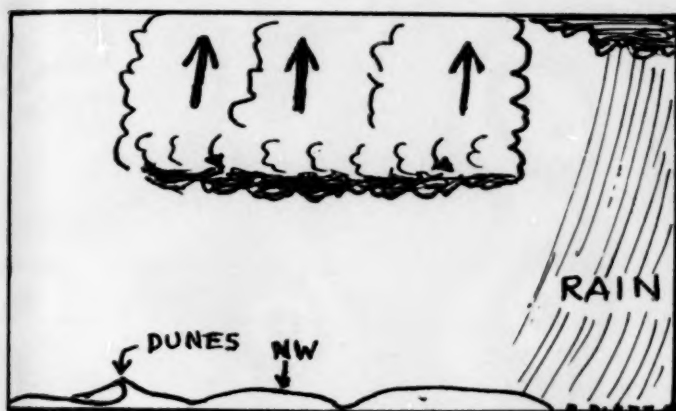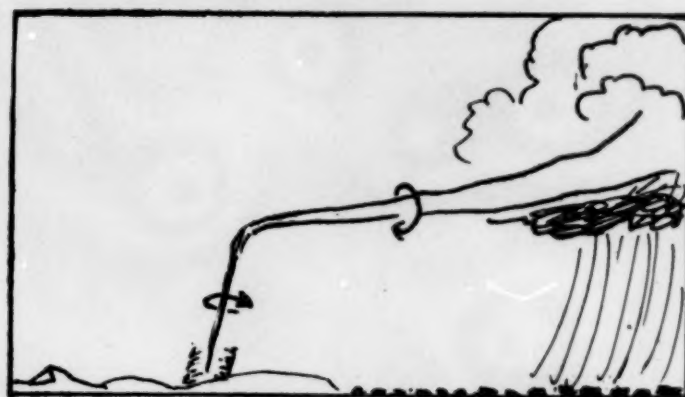

FIGURE 3.—Beginning of roll cloud development.

FIGURE 6.—The complete funnel. It was at this stage that severe damage to several buildings occurred.
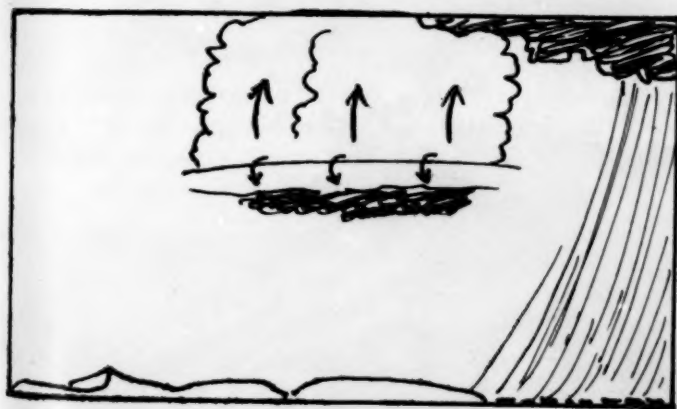

FIGURE 4.—Fully developed roll cloud.

FIGURE 7.—The tornado moving away toward the north-northeast.

moved northeastward about 2 feet but left on the walls, and part of the southwestern wall blown inward. One frame cabin was blown partly off its foundation posts toward the northeast. One ticket booth for an amusement center was overturned and one brick chimney was blown off. The major damage was the collapsing of the front end, walls, and roof of a concrete-block recreation building. The front faced the west-southwest. Wit-

nesses in another building described splintering sounds passing through the building as if every timber in the roof and walls was being shattered although no structural damage was apparent afterward.

As the tornado passed out to sea, moving north-northeastward, the funnel became thick at the top, and it was surrounded by several concentric edges of slowly turning cumulus, looking somewhat like the wrapped leaves at the
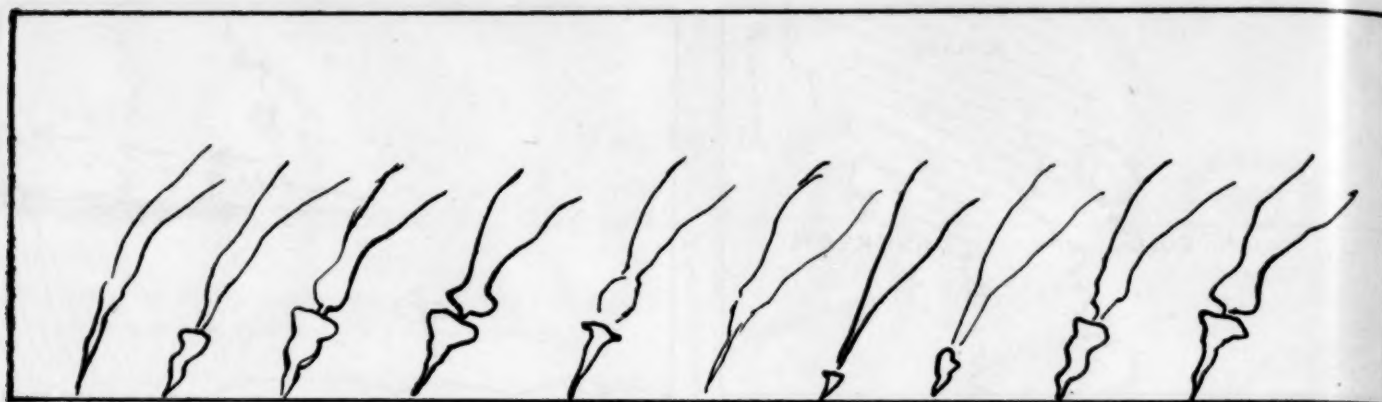
FIGURE 8.—Sketch of the successive thickenings which seemed to move up the funnel just after the stage of figure 6.

Photo by Dan Morill

FIGURE 9.—Photograph of funnel about 3:30 p.m. EST, July 25, 1959, looking north-northwest from Fort Raleigh, Roanoke Island, N.C. The spout dissipated a minute or two later.

end of a cigar (fig. 7). It was now joined to the massive cumulonimbus formation from which heavy rain was falling northeast of the tornado. The tornado was in view for about 15 minutes longer. At this stage (fig. 7) an important change took place in the action of the tornado. Small thickenings of the funnel began from the surface and grew upward, being cone-shaped with spiral ridges (fig. 8). When this formation reached about halfway up to the cumulonimbus base level, resistance to its further ascent developed in the funnel immediately above

in the form of bulbous protuberances. It looked as if a downdraft from above was opposing the updraft from below at this level. A typical sequence of this process is shown in figure 8, viewing from left to right. I saw a similar situation in a very large tornado-waterspout on August 10, 1953, which actually ejected cloud rings from protuberances developing about midway up the funnel cloud.

Also on July 10, 1959, tornado-like damage to electrical lines and poles was reported from 4 miles southwest of this station and about an hour after the disturbance described above, but I have not been able to verify any certain sightings of a funnel cloud. The next day, July 11, during a highly agitated squall cloud condition which produced some very strong localized winds 5 miles to the south-southwest at Manteo, N.C., one boy reported seeing a funnel cloud, but I personally saw none, though I scanned the sky with camera in hand.

Two weeks later, on July 25 at about 1530 EST, a large tornado-waterspout was observed near Colington Island, about 6 miles west-northwest of this station (fig. 1). Although I missed seeing it completely, it was seen by many people along the coast and in Manteo on Roanoke Island. Figure 9 is the second of two photographs of the funnel taken by Mr. Dan Morill from Roanoke Island (fig. 1). Very fortunately, the tornado-waterspout was sketched by Mr. James W. Pace, my art instructor and a man of well-trained powers of observation, as he viewed it from near Kitty Hawk (fig. 1). Figures 10 through 17 are copies of Mr. Pace's sketches, as he faced about south by west from about 5½ miles away.

Surface conditions an hour before the tornado and when rain began were: temperature 89° F., dewpoint 75° F., sea level pressure 30.07 inches, and wind light air from west-southwest. Prior to the onset of rain a band of cumulo-nimbus clouds had slowly developed overhead oriented west-southwest to east-northeast. During the rain squall here, about an hour before the tornado, the wind backed to southeast and east, which is unusual, with gusts to 22 m.p.h. There was no appreciable drop in dewpoint or permanent shift of wind after this disturbance, the wind afterward averaging about 8 m.p.h., from the southwest.

Beginning in figure 10 are the shape sequences of the tornado seen and sketched by Mr. Pace. Figure 10 shows a sheath beginning to grow downward around the cloud tube, reaching its maximum extension in figure 11. Two small poorly-formed pendant clouds are on either side of the main tornado cloud in figure 12 as it lifted temporarily. Rotation in these smaller clouds could not be verified. Figure 13 shows what Mr. Pace called the "dumping stage," as he thought it was "dumping water" back into the Sound. I think it likely that a downflow in the funnel cloud was responsible for the downward progress of the humps. Figures 14 and 15 show the weakening and terminal stages of the tornado. Figure 16 shows what Mr. Pace thought was a line of very slender but well-formed translucent tubes, which lasted about two minutes and
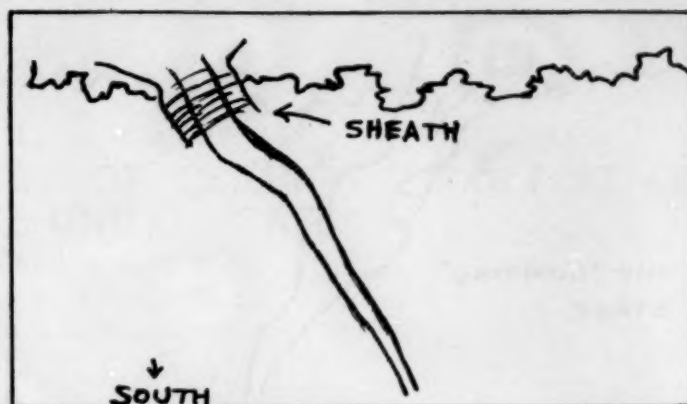

FIGURE 10.—Tornado cloud as seen by Mr. James W. Pace from about 5.5 miles distant near Kitty Hawk, about 1530 EST, July 25, 1959.
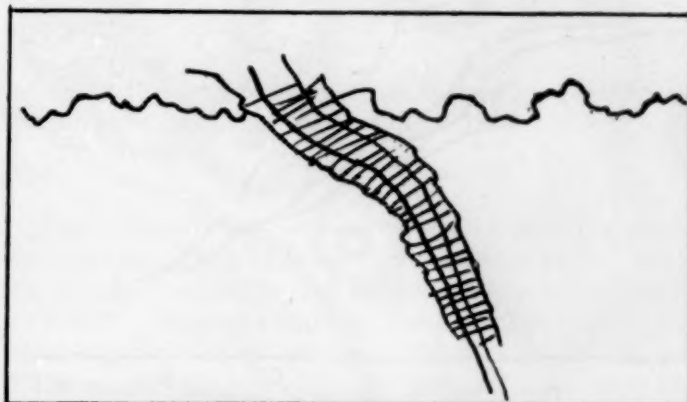

FIGURE 11.—Maximum extension of sheath around funnel shown in its beginning stage in figure 10.

FIGURE 12.—Pendulous formations on either side of the funnel cloud.

appeared just after the main funnel disappeared. He admitted the possibility that these were thin streaks of rain, but did not think they were. The tornado was in view about 10 or 12 minutes.

Figure 17 is Mr. Pace's impression of a cloud of sand, probably whirling, through which he drove several minutes earlier in its formative moments, and which seemed to
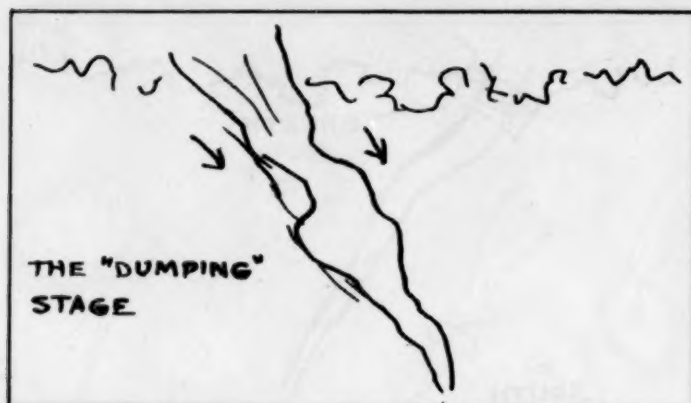
Figure 13.—A kind of down-flow apparent in the funnel.
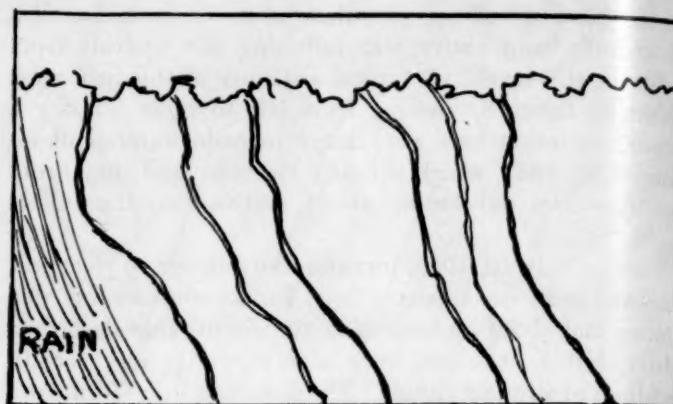

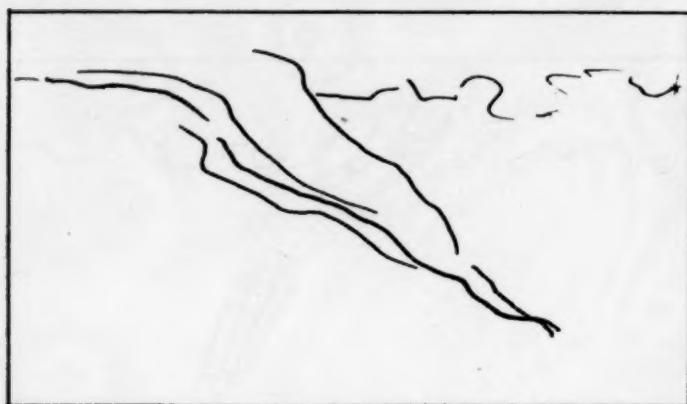Figure 16.—Translucent tubes which appeared after main tornado funnel had disappeared.

Figure 14.—Weakening of the tornado.

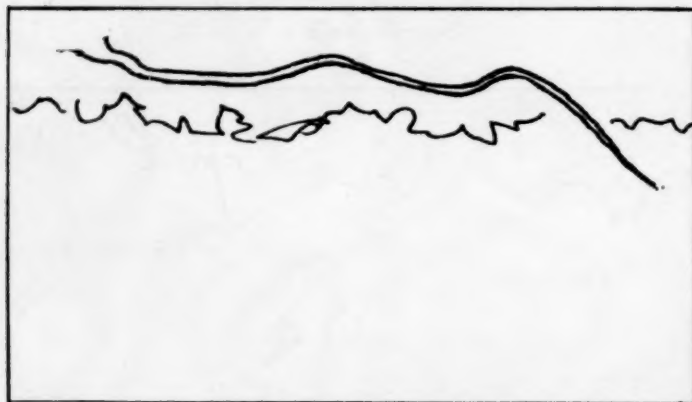Figure 17.—Sand cloud 4 miles east or northeast of the tornado sketched in figures 10–16.

Figure 15.—Terminal stage of the tornado.

move very slowly thereafter. This sand cloud was 4 miles east or northeast of the tornado. No funnel cloud was observed near it.

Two days later, at 1800 EST July 27 and 400 feet from where Mr. Pace viewed this disturbance, wind damage occurred in a very small area, along Highway 158 at Kitty Hawk (fig. 1). The ceiling was blown down in a room of a motel, a door blown off, and a boat blown off its trailer, while across the road at a service station a refreshment stand was blown over a fence toward the northeast. The vending machines at the station were damaged and its plate glass windows were blown in from the southwest injuring three people. Oil cans were reported as flying through the air, but whirling motion or the sighting of a funnel cloud could not be verified. I drove by the spot 30 minutes later, but the rain was so heavy and visibility so poor that I was unaware of the damage. Severe lightning was also in progress at the time I passed, with the main body of the thunderstorm then out at sea to the northeast.

MONTHLY PERCENTAGE FREQUENCY OF CEILINGS 2,000 FEET OR HIGHER OVER THE UNITED STATES

M. N. HUNTER, R. I. FOSTER, and H. A. SCOTT

U.S. Weather Bureau, Washington National Airport, Washington, D.C.

ABSTRACT

Maps of the percentage frequency of occurrence of ceilings of 2,000 ft. or higher over the United States, excluding Alaska and Hawaii, are presented for each month. A second set of maps shows for each month the change in percentage from the preceding month.

1. INTRODUCTION

Low ceilings are frequently the cause of interrupted aircraft operations involving either delays or cancellations of flights. The increase in air traffic and the change to jet-type aircraft, which must land at a destination or alternate airport with little or no delay, emphasize the need for extended weather information for planning purposes. Government and military personnel, business executives, and many airline passengers planning important journeys, need some indication of advance aviation weather probabilities to decide upon their mode of transportation and time of departure. An increasing number of requests for information involve aviation weather probabilities for periods beyond those for which conventional aviation weather forecasts can be made at the present time.

If such requests are for periods in the order of 24 to 72 hours in advance, the meteorologist must consider the present synoptic situation and available prognostic material in arriving at some kind of probability guidance. Readily available aviation climatological information can be used to good advantage as background information in such cases. If the request is for an even more extended aviation weather probability, the meteorologist must depend almost entirely on aviation climatological information. The type of information needed is frequently nonexistent or inaccessible.

As an aid to the solution of the problem of providing some type of advance aviation weather information, maps have been constructed showing the percentage frequency of ceilings 2,000 feet or higher over the United States. Aircraft operations over the greater part of the United States are usually not interrupted when ceilings are above 2,000 feet, but the problems involving aircraft operations increase as the ceilings fall below 2,000 feet. Therefore the 2,000-foot limit was used as the basis for these charts, even though it is well-known that terrain, weather, density

of air traffic, and possibly other things are contributing factors in determining the flow of air traffic.

2. DATA

The basic data used in construction of these maps were obtained from summaries, covering a 5-year period, of the hourly observations for 115 airport stations in the United States [1]. Supplementary data from [2] and [3] were also used with various climatological charts in [4], [5], [6], and [7] as supporting material. Topographic maps were also used in interpolating over areas where data were sparse. Maps, showing the geographical distribution of 2000-ft. and higher ceilings were constructed for each month of the year (fig. 1) since there is a great variation between seasons and also between months of the same season. In addition, derivative maps, showing the change from the previous month, were constructed for each month of the year (fig. 2).

3. SEASONAL FEATURES

The following paragraphs describe the most prominent seasonal features depicted by figures 1 and 2.

WINTER MONTHS (DECEMBER, JANUARY, AND FEBRUARY)

A high frequency of low ceilings prevails over the Great Lakes Region and along the western slopes of the Appalachian Mountains from Pennsylvania to Georgia. A secondary region of low ceilings occurs from Washington State southward over the Cascade Range and Sierra Nevada and down through the Rocky Mountains. The frequency of low ceilings reaches a peak during the month of January over both of these areas with noticeable improvement beginning during February. Over southern Texas, where a gradual shift in the mean wind to southeasterly advects moisture from the Gulf of Mexico, a high frequency of low ceiling continues during February. Over the remainder of the Plains States and in Florida, rela-
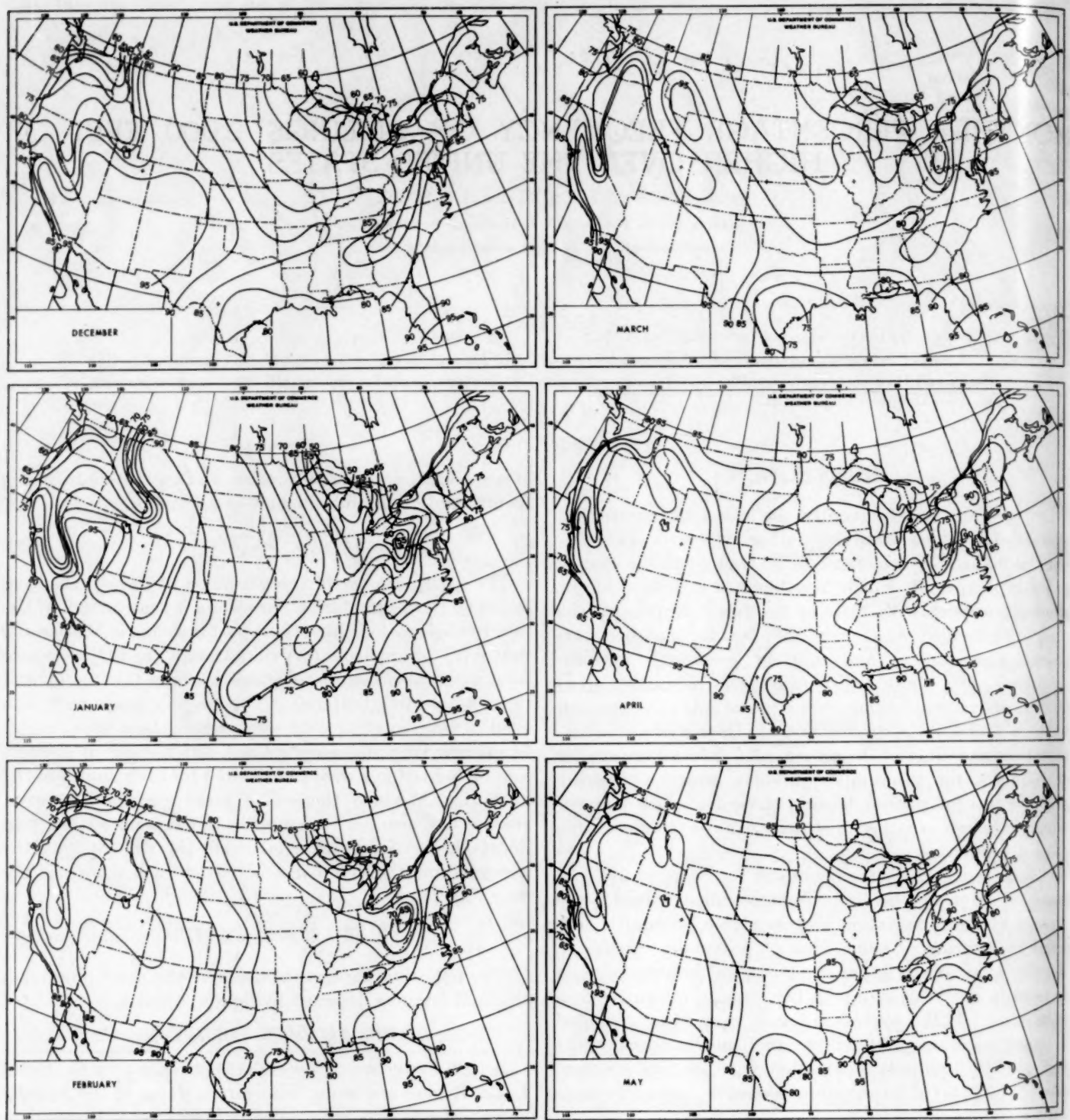
FIGURE 1.—Monthly average percentage frequency of ceilings 2,000 feet or higher.

tively high, frequency of ceilings above 2,000 feet persists during the winter season.

SPRING MONTHS (MARCH, APRIL, AND MAY)

Rapid improvement of low ceilings from Washington State through the Cascade Range, Sierra Nevada, and Rocky Mountains may be noted during March with gradual improvement thereafter. Improvement of the low ceilings over the Great Lakes Region and the western slopes of the Appalachian Mountains occurs throughout the spring months with improvement becoming more rapid during May. Southeasterly advection of moist air over
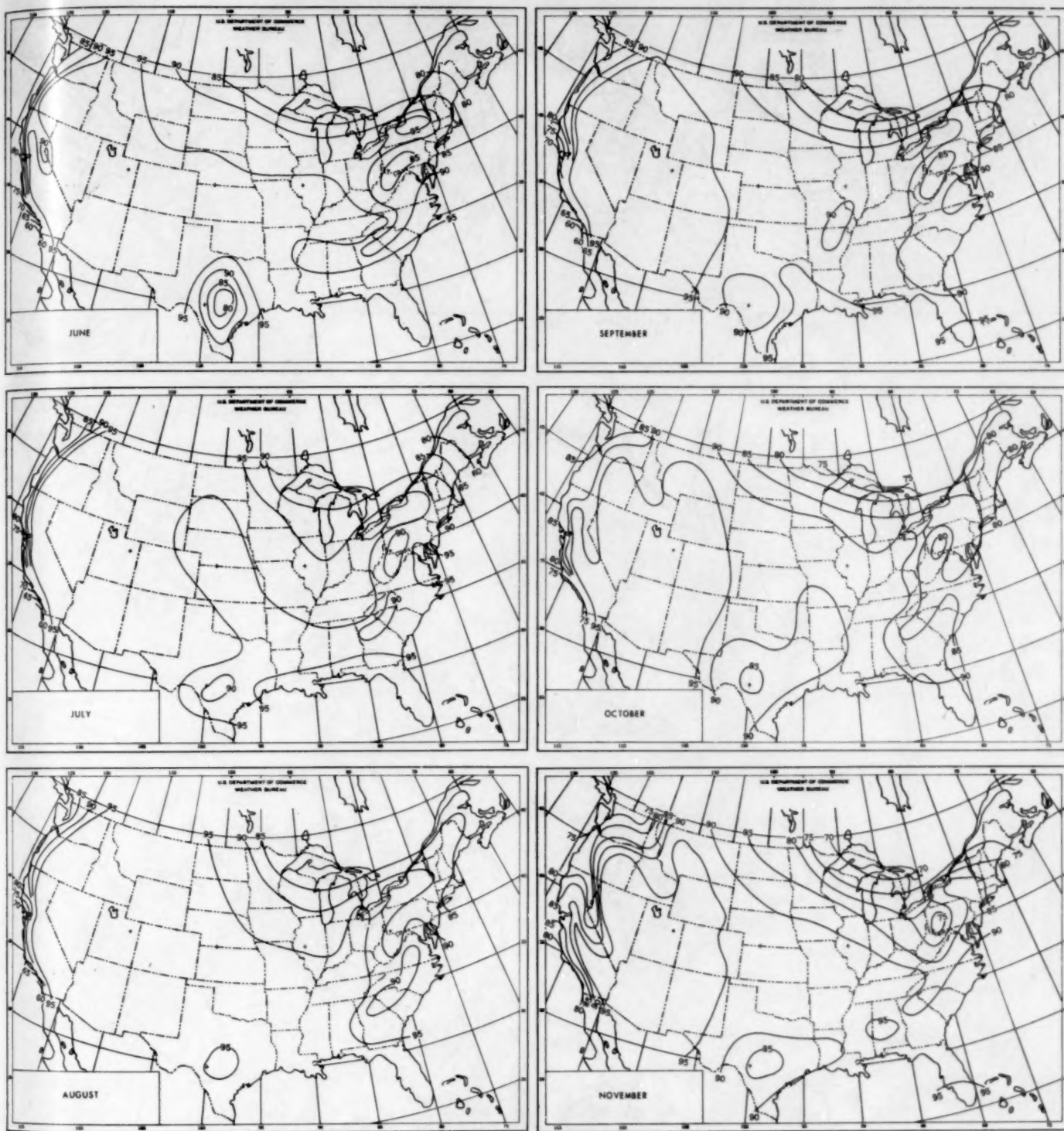
FIGURE 1.—Continued.

eastern Texas and the Southern Plains is evidenced by the relatively high frequency of ceilings below 2,000 feet over this area, especially during the late spring. A rapid increase in the frequency of ceilings below 2,000 feet occurs along the western sections of the Coastal Range in California during April. Elsewhere there is a gradual

tendency toward a higher frequency of ceilings above 2,000 feet during the spring.

SUMMER MONTHS (JUNE, JULY, AND AUGUST)

Coastal stratus over the western sections of the Coastal Range in California prevails throughout the summer.
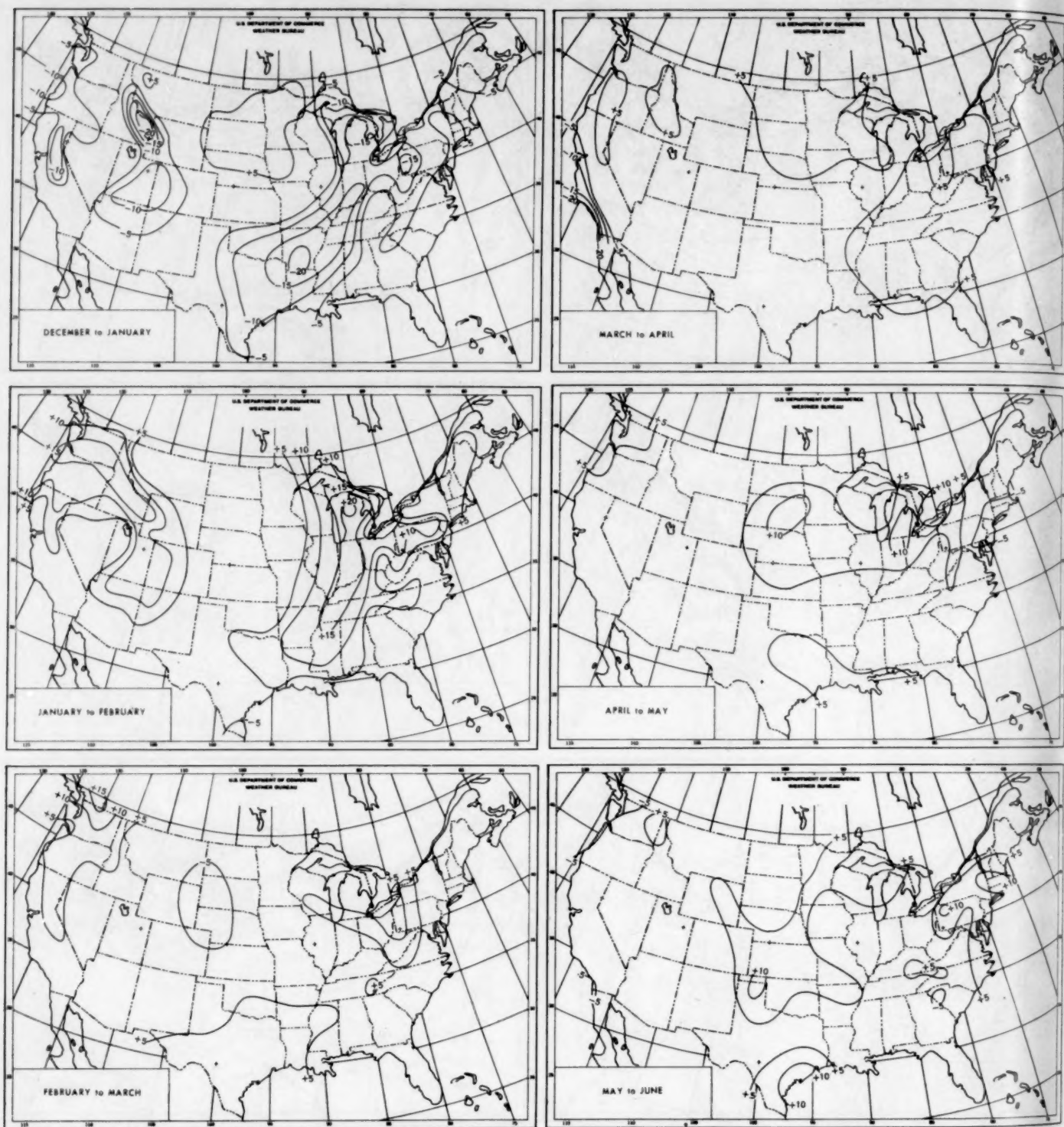
FIGURE 2.—Month-to-month change in percentage frequency of ceilings 2,000 feet or higher.

However, it is interesting to note that the frequency of ceilings below 2,000 feet in this area during the summer is not as great as that experienced over northern Michigan and in part of western Pennsylvania during the winter. The remainder of the United States, including Texas and the Southern Plains where rapid improvement occurs during June, generally has the highest percent of ceilings above 2,000 feet during the summer season.

AUTUMN MONTHS (SEPTEMBER, OCTOBER, AND NOVEMBER)

Very little change occurs during September except the slight increase in frequency of ceilings below 2,000 feet
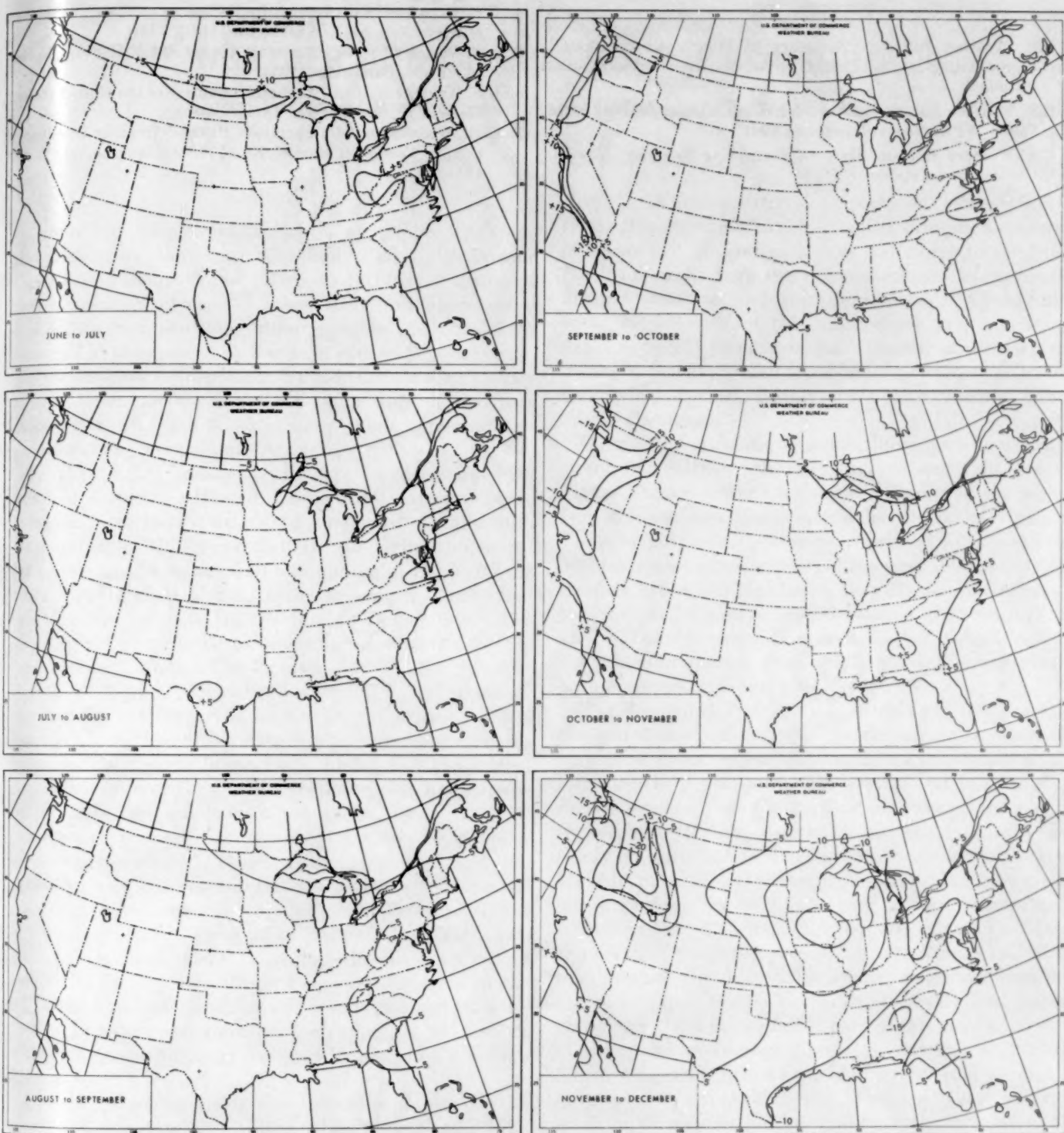
FIGURE 2.—Continued.

over northern Michigan, most of Maine, along sections of the Appalachian Mountains, and northern Florida through coastal areas of Georgia. Rapid improvement of the coastal stratus along California is evident during October. The frequency of ceilings below 2,000 feet increases over northern Michigan, through the northern Appalachians, and from Washington State through the Cascade Range, Sierra Nevada, and Rocky Mountains during November, with the pace becoming more rapid toward the end of the month and through December.

REFERENCES

1. U.S. Weather Bureau, "Summary of Hourly Observations," *Climatography of the United States No. 30*—(for individual stations).

2. U.S. Weather Bureau, *Airway Meteorological Atlas for the United States*, WPA, New Orleans, La., 1941.

3. U.S. Weather Bureau, *Terminal Forecasting Reference Manual*, (for individual stations).

4. U.S. Department of Agriculture, "Climate and Man," *Yearbook of Agriculture 1941*, Washington, D.C., 1941.

5. S. S. Visher, *Climatic Atlas of the United States*, Harvard University Press, Cambridge, 1954.

6. U.S. Weather Bureau, "Climatic Summary of the United States," *Bulletin W*, Washington, D.C., 1930.

7. Civil Aeronautics Administration, "Pilots' Weather Handbook," *C.A.A. Technical Manual* No. 104, Washington, D.C., July 1954, 143 pp.

THE WEATHER AND CIRCULATION OF SEPTEMBER 1959

Quasi-Periodic Oscillations in Zonal Index and Centers of Action

J. F. O'CONNOR

Extended Forecast Section, U.S. Weather Bureau, Washington, D.C.

1. HIGHLIGHTS

One of the weather highlights of September 1959 was the striking of the South Carolina coast by hurricane Gracie near month's end. Due to the timely warnings and evacuation of coastal areas, there was no reported loss of life from drowning although more than 20 deaths occurred in the storm. A few days earlier, September 26, one of the most catastrophic typhoons of modern history struck Japan near Nagoya. Deaths were reported in excess of 4,000, with 1,700 missing, many thousands injured, and enormous property damage.

In the United States surprisingly large contrasts in weather occurred. Record temperature extremes were common. North Platte, Nebr., reported a maximum temperature of 102° F. on the 7th, the highest on record for so late in the season, and a minimum of 29° F. on the 10th. At Hartford, Conn., three temperature minima and two maxima set new records for individual days. Los Angeles had the warmest September of record (average temperature 72.8°). The hottest day of the year at Buffalo, N.Y., was September 9 when 95° F. was recorded, the highest ever reported so late in the season. Binghamton, N.Y., had the warmest September since records began in 1891, while Idaho Falls, Idaho, had the coldest September of record. Grand Junction, Colo., had a freeze on the 28th, the earliest in 51 years.

Excessive precipitation occurred this month in many areas. For example, Boise, Idaho, reported 2.54 in., exceeding all September totals since 1864. Other cities reporting record amounts were Kalispell, Mont. with 3.84 in.; Sexton Summit, Oreg., 2.81 in.; Seattle, Wash., 4.60 in.; and Oakland, Calif., 3.27 in., the previous record being 0.82 in. in 1939. Record snowfall hit areas in the lee of the Colorado Rockies. Colorado Springs received 34.1 in. of heavy wet snow on September 28, 29, and 30, with damage to property reported in excess of a million dollars.

By way of contrast this was the driest September on record at Lexington, Ky., Milton, Mass., Providence, R.I., Oak Ridge, Tenn., and Brownsville and El Paso, Tex. Philadelphia, Pa. had its longest consecutive period without rain, from the 4th to the 27th.

This was the windiest September on record at many places on the west coast from Sacramento, Calif. northward to Olympia, Wash.

2. MONTHLY CIRCULATION AND WEATHER

The largest abnormalities of the Northern Hemisphere's circulation in September 1959 occurred in western Europe (fig. 1). A strong anticyclone persisted in the vicinity of Great Britain throughout the month, bringing a succession of warm, dry, and brilliant days and nights to the British Isles, following four consecutive months of unequalled dryness, sunshine, and warmth combined. Closely allied with the strength of this anticyclone were the intense negative height departures from normal to the east, over northern Russia, a manifestation of persistent storminess and below normal temperatures over eastern Europe during the month.

Over North America, however, there were no unusually strong circulation anomalies in the monthly average. Figure 1 shows lower than normal heights in the western United States and above normal heights in the Northeast. These height departures were associated with lower than normal temperatures in most of the west and north-central sections, while the Northeast, the Mississippi Valley, and the Southern Plains averaged warmer than normal (fig. 2A). Within the month, however, some violent temperature fluctuations occurred, and record temperatures at both extremes were not uncommon.

The departures from normal of this month's precipitation are shown in figure 2B. September was a wet month over most areas except the Northeast and Southwest, in line with the prevailing height anomaly pattern which reflected stronger than normal flow of moist air from source regions in the Gulf of Mexico, Pacific, and Atlantic. Very heavy precipitation occurred in the West north of northern Nevada and Utah, with many places in this region reporting this month the wettest or near wettest September on record. Most of the heavy precipitation from the Mississippi Valley westward occurred in the second half of the month when the deep mean trough migrated from near the west coast to the Continental Divide and became stationary there in the latter part of the month.

Although the average circulation for the month over North America was not greatly different from normal, an intramonthly upheaval in the broad-scale flow occurred, resulting in considerable variability in the circulation and weather within the month. This evolution will be considered in some detail below.

3. THE INDEX CYCLE

An interesting aspect of this month's weather was the oscillation of the speed of the 5-day mean 700-mb. westerlies at temperate latitudes in the Western Hemisphere (fig. 3). This was a continuation of a rhythmical variation in the strength of the westerlies which started in early August with the first substantial weakening of wind speeds since June 20. The next low point in the index
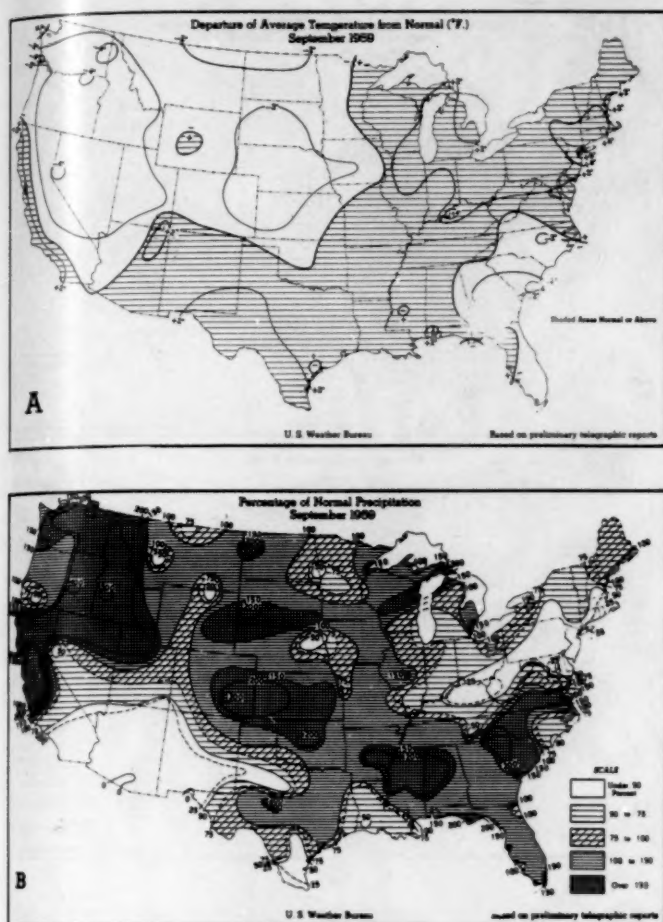
FIGURE 1.—Mean 700-mb. contours (solid) and height departures from normal (dotted) (both in tens of feet) for September 1959. The westerlies averaged near normal, being somewhat depressed in western North America but north of normal in the East.

(4.8 m.p.s.) was reached at the end of August, after which the westerlies increased until the 5-day period ending September 7, when the first maximum of September (9.3 m.p.s.) occurred. This was followed by a decrease to 6.5 m.p.s. a week later, after which a new high of 10.4 m.p.s. was reached on the 26th. Following this peak, another decrease set in, which was still in progress at month's end.

Figures 4 to 7 are presented to illustrate the sequence of 5-day mean circulation and weather anomaly patterns associated with this rhythm in the strength of the westerlies.

4. FIRST WEEK—HIGH INDEX

The high index at the end of the first week was due primarily to a deep Low over northwestern Canada (fig. 4A) which maintained stronger than normal westerlies over North America. Five-day mean Lows in September have not been observed this far west in Canada in the last decade or more, since in this area a ridge normally prevails. With the mean Low in this position (see also the sea level mean, fig. 4B) the regime was unfavorable for anticyclonic activity in Canada. As a result, most of

FIGURE 2.—(A) Departure of average surface temperature (° F.) from normal for September 1959. (B) Percentage of normal precipitation for September 1959. (*From Weekly Weather and Crop Bulletin, National Summary,* vol. XLVI, No. 40, October 5, 1959, and No. 41, October 12, 1959.

the United States remained warmer than normal except for the Far West (fig. 4C). Here cooler than normal Pacific air predominated, largely due to stronger than normal westerlies along the west coast. The abnormal strength of the westerlies can be deduced from the height departures in this area (fig. 4A), which totalled 820 feet of contour gradient in excess of the normal, between the positive center off lower California and the negative center in western Canada.

Figure 4B, which depicts the average sea level flow during the first week, shows the predominantly southerly flow from the southern Rockies eastward which kept this area warmer than normal. Also, the southeasterly drift of tropical Atlantic air which favored showery conditions along the Atlantic Seaboard may be inferred from the abnormal location of the Bermuda High near the Maritime Provinces.

The tracks on figure 4B show that only one High crossed the country during the week, and this of Pacific origin.
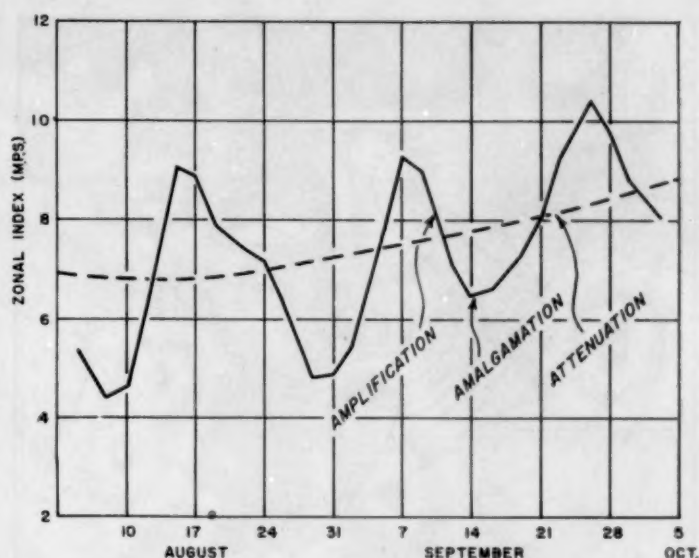

FIGURE 3.—Time variation of 5-day mean values of the zonal index in meters per second, plotted on the last day of the period. The index is computed from 35° to 55° N. for the Western Hemisphere. The dashed line represents the variation of normal index. Arrows indicate approximate stages of the index cycle when amplification, amalgamation, and attenuation of the planetary wave train occurred.

It slowed down over the Northeast and maintained easterly flow over the western Atlantic as far north as 40° N. This flow kept the Southeast wet through much of the week (fig. 4D).

Considerable storminess occurred over western Canada with practically no anticyclonic activity. Over the United States the only significant cyclonic activity was a weak Low which traversed the lower Mississippi and Ohio Valleys early in the week, spreading heavy rains through much of this area.

5. SECOND WEEK — AMPLIFICATION AND RETROGRESSION OF THE LARGE-SCALE WAVES IN THE WESTERLIES

During this week the speed of the westerlies dropped sharply in the Western Hemisphere, reaching a minimum at week's end. This was a manifestation of marked amplification of the large-scale waves in the westerlies over the Pacific and North America.

Associated with this amplification was an almost complete phase shift of the major waves over North America from the first week. Figure 5A shows the strong upper-level High that developed over the Rockies in consonance with deepening south of Alaska. This reversal of phase might be viewed as a retrogression of the large-scale height anomalies over North America and the Atlantic. Comparing figures 5A and 4A, it may be seen that the Scandinavian positive anomaly retrograded to Iceland,
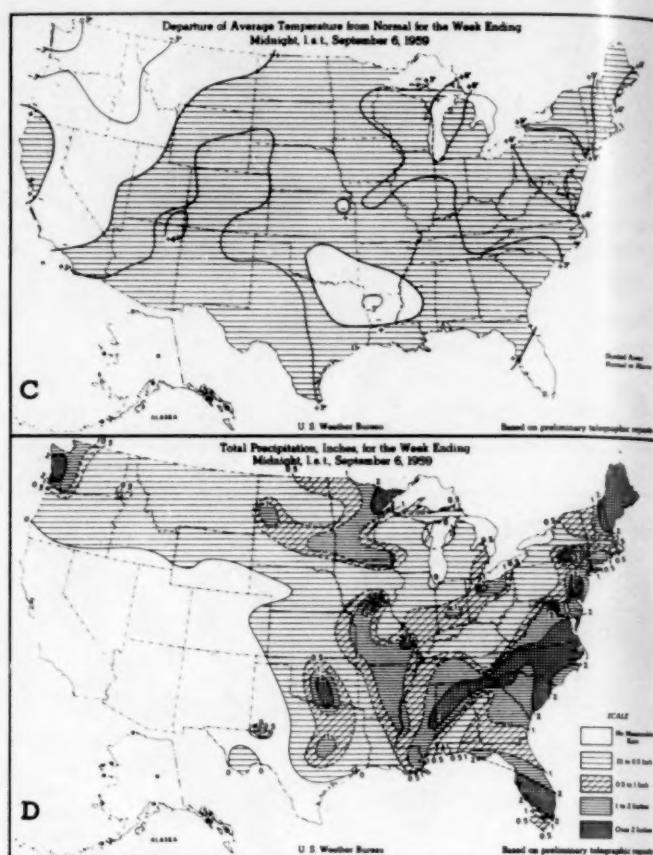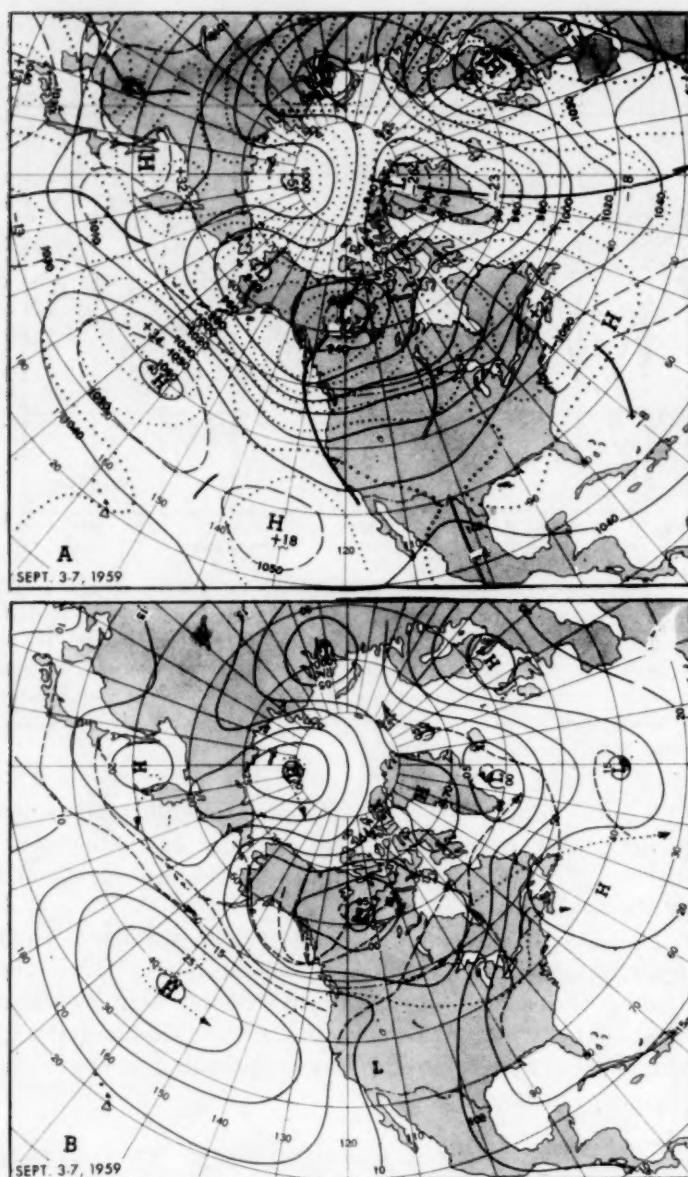
FIGURE 4.—(A) 5-day mean 700-mb. contours (solid) and height
departures from normal (dotted) (both in tens of feet) for Sep-
tember 3–7, 1959.   (B) Mean sea level isobars (solid) (millibars—
hundreds omitted) for September 3–7, with smoothed tracks of
migratory cyclones (dashed) and anticyclones (dotted) for week
ending September 7, 1959.   (C) Departure of average surface
temperature from normal (° F.), and (D) total precipitation
(inches) for the week ending September 6, 1959. (C and D from
Weekly Weather and Crop Bulletin, National Summary, vol. XLVI,
No. 36, Sept. 7, 1959.)

the positive center over the Maritime Provinces retreated
to middle North America, and the western Canadian
negative center backed off into the northeastern Pacific.

The amplification of the ridge in western North America
occurred almost explosively between September 9 and 10,
with simultaneous deepening of the troughs near Kam-
chatka and the Gulf of Alaska. During this period
typhoon Patsy (fig. 5B) emerged from the subtropics and
contributed its energy to the developing Kamchatka
vortex. At the same time an upper-level anticyclone
from north of the East Siberian Sea drifted southeastward
and merged temporarily with the intensifying central
Pacific ridge about midweek (fig. 5A) before continuing
southeastward to reamalgamate with the amplifying ridge
in North America.

The ridge development in the western United States
was accompanied by strong warming over that area while
at the same time it deployed cool air into the East as the
southerly flow of the previous week gave way to northerly
flow in this region. This is clearly portrayed by the
mean sea level chart (fig. 5B). The front which ushered
the cold air into the Eastern States from the 9th to the
11th dropped temperatures 20°–40° in a few hours, ending
the late-season heat and humidity which had prevailed
for a month or more. This heat wave was climaxed by
record maxima on the 8th and 9th, such as 96° at Sheridan,
Wyo., 103° at Rapid City, S. Dak., 94° at Cleveland,
Ohio, and 98° at Rochester, N.Y. Despite the cooling,
northern sections still averaged above normal for the
week due to the large surplus built up in the early part of
the week (fig. 5C).

Rains were light over most of the country this week
(fig. 5D) since the location of the High in the West pre-
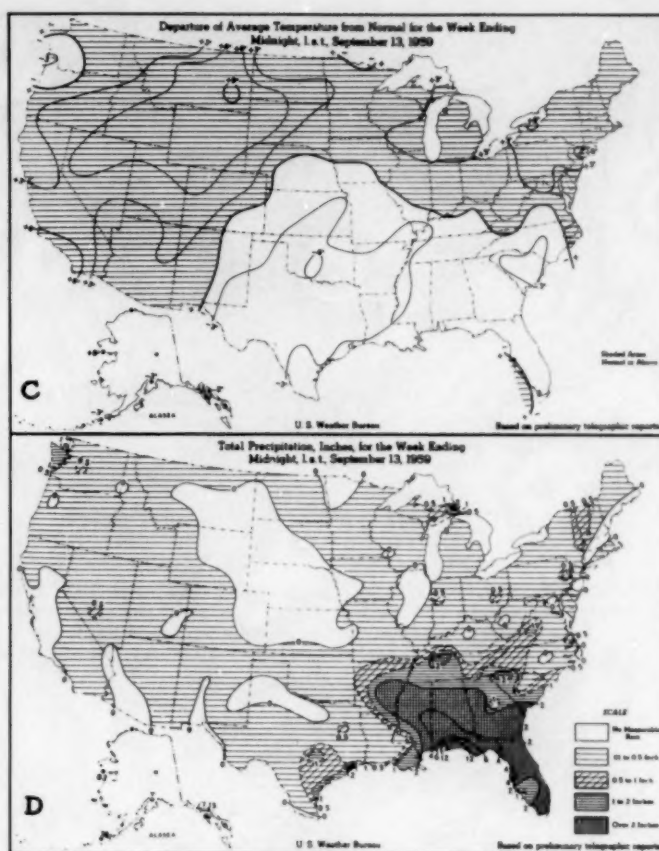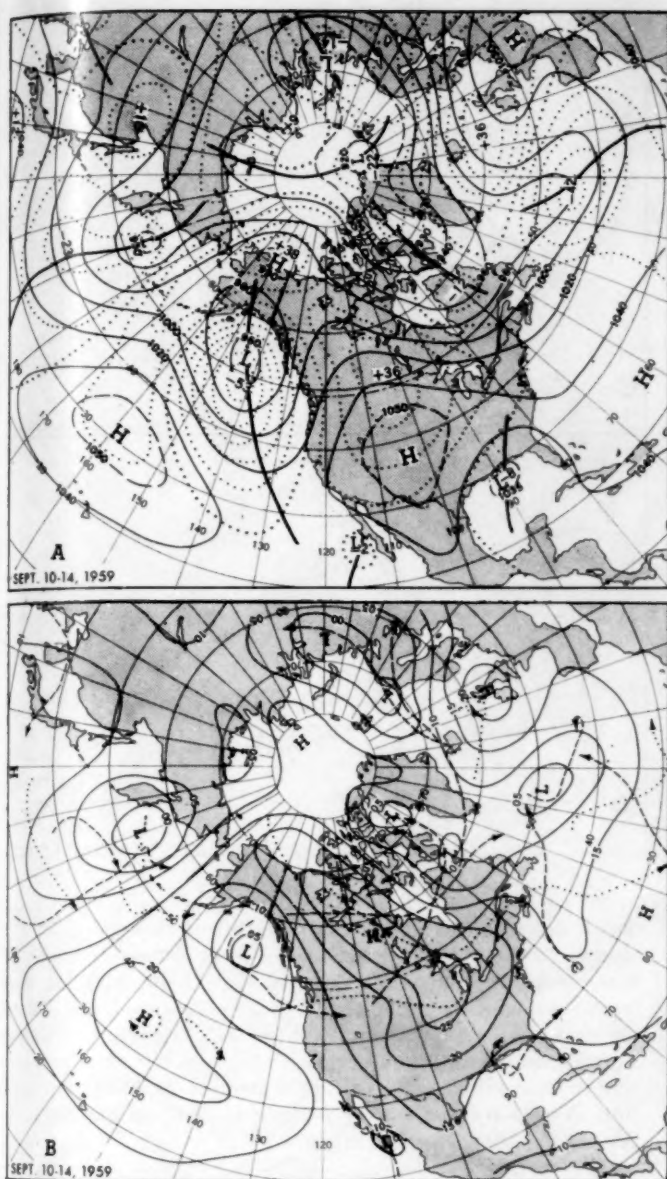vented moisture from entering most areas. The subsid-

FIGURE 5.—(A) 5-day mean 700-mb. contours (solid) and height departures from normal (dotted) (both in tens of feet) for September 10–14, 1959. (B) Mean sea level isobars (solid) (millibars—hundreds omitted) for September 10–14, with smoothed tracks of migratory cyclones (dashed) and anticyclones (dotted) for week ending September 14, 1959. (C) Departure of average surface temperature from normal (° F.) and (D) total precipitation (inches) for the week ending September 13, 1959. (C and D from *Weekly Weather and Crop Bulletin, National Summary* vol. XLVI, No. 37, September 14, 1959.)

ing motions associated with anticyclonic curvature of the flow provided an additional desiccating mechanism.

However, in the Southeast, conditions were quite different. Here cyclonic flow associated with a Low near the mouth of the Mississippi River maintained ascending motion over the East Gulf States, overrunning the wedge of cooler than normal air. This produced excessive rains in the East Gulf States and the Carolinas, with totals in excess of 4 inches over a large area. Both Pensacola and Appalachicola, Fla., reported over 11 inches, with almost 10 inches falling at Pensacola in one 24-hour period on the 12th and 13th.

A comparison of figure 5B with 4B reveals further highlights of the dramatic reversal of the circulation from the first week to the second week. The cyclone tracks reflect the absence of cyclonic activity over the United States except in the Gulf of Mexico and in the extreme West. Here the Low from the Gulf of Alaska plunged south-

eastward toward the Pacific Northwest as the amplification neared its climax.

The anticyclone track from the Pacific Northwest to the Great Lakes was also a symptom of the extreme amplification process going on at upper levels. For one thing this High intensified as it moved across the northern Plains, and its northward recurvature along Lake Michigan on the 12th was probably one of the most unusual anticyclone tracks on record for this area. The southward movement of the Gulf of Alaska Low and the northward movement of the High were both compatible with diminishing westerlies at middle latitudes.

6. THIRD WEEK—AMALGAMATION OF ANTICYCLONES OVER CANADA

Early in the third week the large-scale waves reached their greatest amplitude. At this time the southeastward-moving anticyclone from the East Siberian Sea
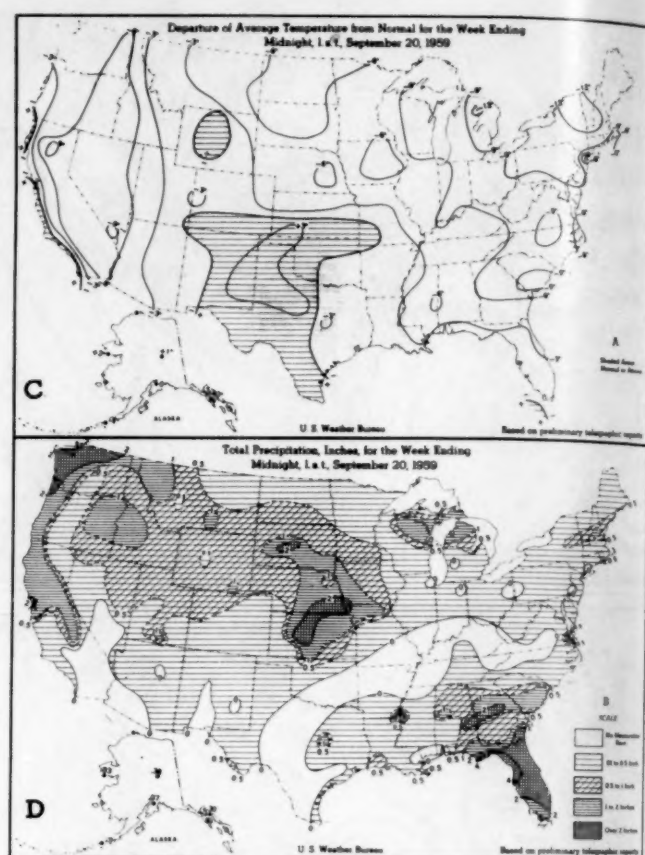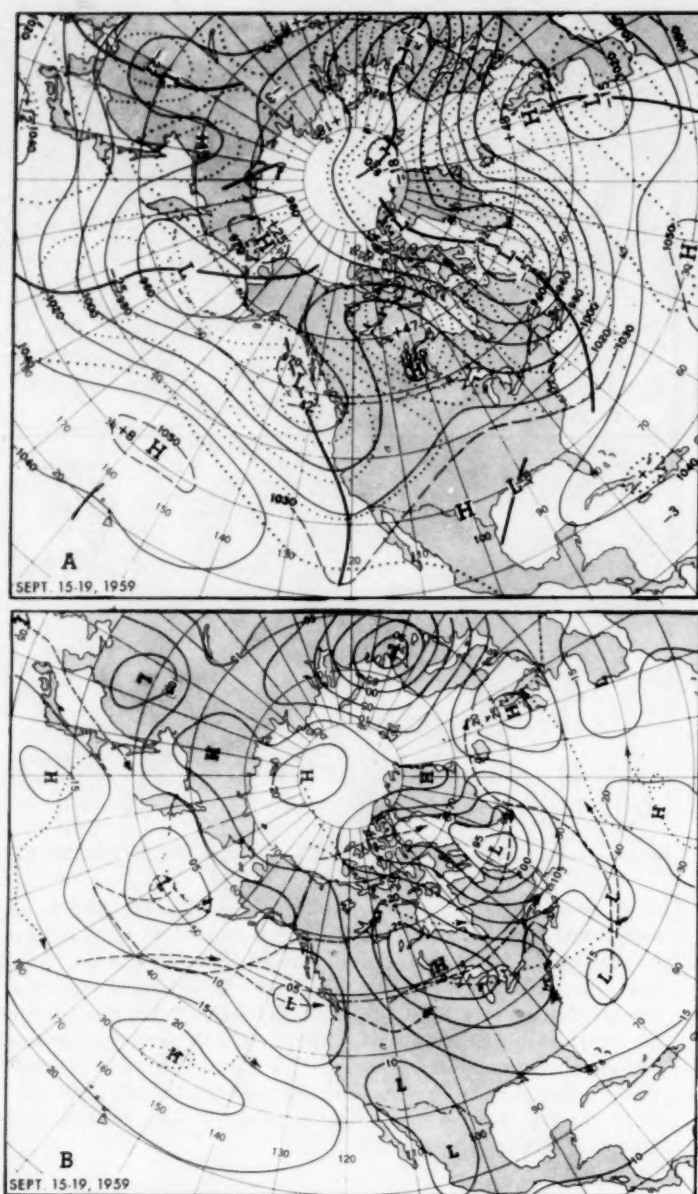
FIGURE 6.—(A) 5-day mean 700-mb. contours (solid) and height departures from normal (dotted) (both in tens of feet) for September 15–19, 1959. (B) Mean sea level isobars (solid) (millibars—hundreds omitted) for September 15–19, with smoothed tracks of migratory cyclones (dashed) and anticyclones (dotted) for week ending September 21, 1959. (C) Departure of average surface temperature from normal (° F.), and (D) total precipitation (inches) for the week ending September 20, 1959. (C and D from *Weekly Weather and Crop Bulletin, National Summary,* vol. XLVI, No. 38, September 21, 1959.)

merged over central Canada with the northward-moving anticyclone from the western United States. This was followed by severing of the anticyclone over central Canada as a new branch of westerlies broke across the central United States to its south. This evolution proceeded in concert with further deepening of the west coast trough as the Low from the Gulf of Alaska migrated toward the Pacific Northwest. Figure 6A shows the average circulation at 700 mb. for period September 15–19, with the height departures from normal highlighting the blocking character of this stage of the cycle; i.e., a positive departure area over central Canada flanked by negative areas to its southeast and southwest. This period is a classic example of the forecaster's rule that blocking in Canada is generally associated with cold and wet conditions in the United States, shown by figures 6C and 6D.

The mean sea level chart (fig. 6B) reflects the storminess which dominated the Pacific Northwest during this period.

The mean Low off the west coast averaged 15 mb. below normal, and was largely a reflection of an intense winter-type storm which attained a minimum pressure of at least 985 mb. near the Oregon coast on the 18th. This storm brought high winds and practically all the month's record rainfall to northern California. San Francisco received 2.30 inches within 24 hours, more than twice the previous September record and 24-hour record. San Francisco airport also reported high winds of 48 m.p.h. on the 18th, 5 m.p.h. higher than the previous record.

In the East, the week was featured by the southeastward migration of an unusually intense Arctic anticyclone from the Lakes Region across the Middle Atlantic States, as shown by the track on figure 6B. This track was a symptom of the early stages of attenuation of the extreme amplitude of the large-scale flow of mid-month. This slowly-moving High produced record-breaking low temperatures in the Northeast, from the Great Lakes to New
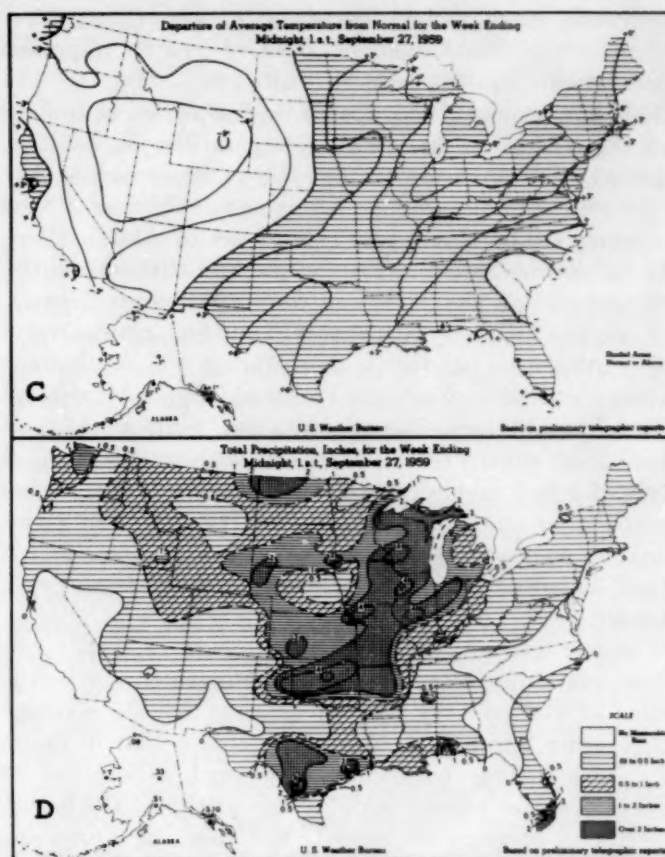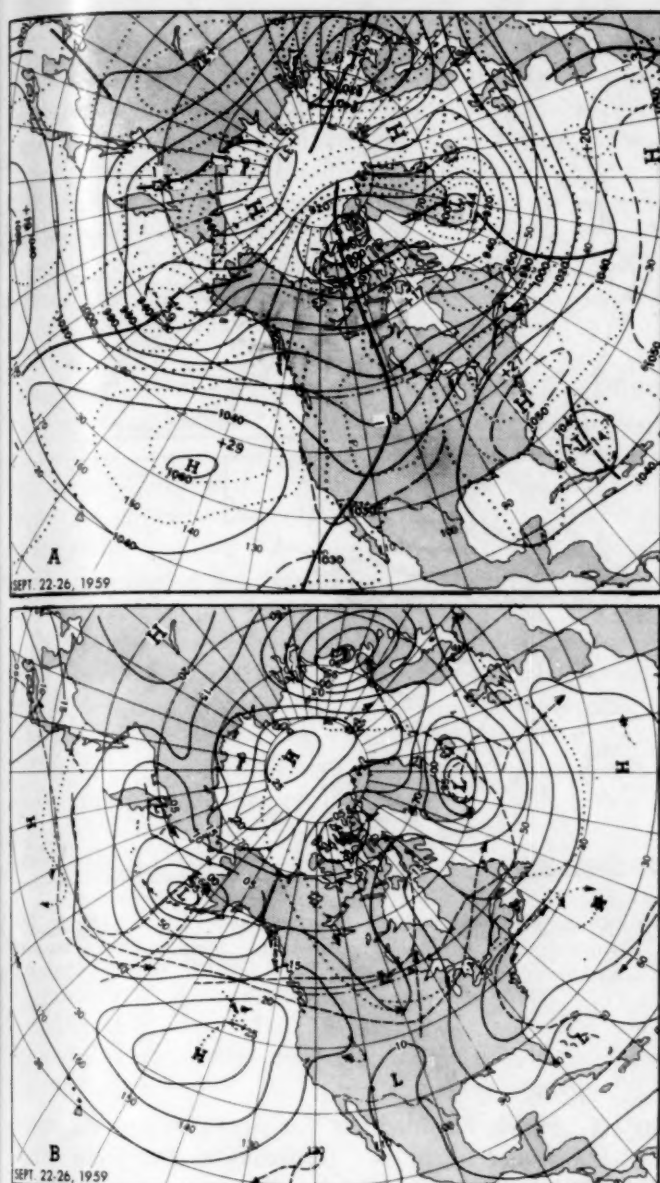
FIGURE 7.—(A) 5-day mean 700-mb. contours (solid) and height departures from normal (dotted) (both in tens of feet) for September 22–26, 1959. (B) Mean sea level isobars (solid) (millibars—hundreds omitted) for September 22–26, 1959 with smoothed tracks of migratory cyclones (dashed) and anticyclones (dotted) for week ending September 28, 1959. (C) Departure of average surface temperature from normal (° F.), and (D) total precipitation (inches) for the week ending September 27, 1959. (C and D from *Weekly Weather and Crop Bulletin, National Summary*, vol. XLVI, No. 39, September 28, 1959.)

7. FOURTH WEEK—ATTENUATION AND PROGRESSION OF THE LARGE-SCALE WAVES IN THE WESTERLIES

The fourth week saw the culmination of this remarkable 3-week cycle of development and decay of the large-scale wave pattern aloft. The attenuation of the major ridge over central North America was characterized by an almost complete phase shift over this continent, similar to, but in reverse of, the retrogressive shift which accompanied the amplification stage of the cycle in the second week. This week's reversal saw the ridge of the third week give way to a trough over central North America (fig. 7A). This may be viewed as a progression of the Pacific coastal trough eastward in response to increasing westerlies. Similarly, the collapse of the block over Canada may be viewed as a southeastward progression of this feature to the Middle Atlantic States. In terms of height anomalies, the negative anomaly off the Pacific

England, a marked reversal from the record high temperatures of the early part of the second week. A few examples of the cold accompanying this High are: Lansing, Mich., record minima of 32° and 31° on the 16th and 17th, respectively; Toledo, Ohio, minimum temperatures in the 30's on four consecutive days from the 16th to the 19th; and Pittsburgh, Pa., record minima in the 30's on the 17th, 18th, and 19th.

Heavy rains this week spread eastward across the Rockies to the Great Lakes Region as the southwesterly flow of moist air that prevailed aloft (fig. 6A) overran the cold Arctic air as far east as the Upper Mississippi Valley, with Kansas receiving ½ to 3 inches over most of the State. A similar overrunning pattern existed in the Southeast, producing excessive precipitation amounts of 8 to 10 inches at scattered places in Florida.

Northwest coast moved eastward to the Continental Divide, while the Canadian positive center migrated southeastward into the eastern United States.

This evolution set the stage for intensification of cooling over the central Rockies, while temperatures in the East returned to record warmth (fig. 7C) in many places, due to the return of abnormally strong southerly flow. New maximum temperature records were set at Akron, Ohio, with 88° on the 28th and Pittsburgh, Pa., with 90° on the 28th and 89° on the 29th, and were equalled at Albany, N.Y. on the 24th and 28th with 87° and 83°, respectively.

The persistent southerly flow during the week from eastern Texas to the Northern Plains and Upper Mississippi Valley brought excessive precipitation, high winds, and severe local storms to the Midwest, with weekly rainfall totals of 1 to 3 inches over a large area (fig. 7D). Local precipitation amounts of more than 10 inches in Oklahoma, 6 inches in southern Texas and Kansas, and 5 inches in Iowa, Minnesota, Illinois, and Michigan were recorded.

The strength and persistence of the meridionally oriented polar front associated with the mean trough in the center of the country can be assessed by the average temperature anomaly gradients for this period in figure 7C. This strong baroclinic zone bred a number of vigorous frontal waves, one of which produced the lowest September pressure of record, 989 mb., at Dubuque, Iowa on the 26th. This front, overrun by very warm and moist tropical Gulf air, spawned several tornadoes in Missouri, Wisconsin, Illinois, Kansas, and Iowa, on the 26th and 27th. Figure 7B shows the mean sea level pressure pattern characteristic of the week, with the associated cyclone and anticyclone tracks.

Late in the week the polar front moved eastward as cold Arctic air flowed southward into the northern Rockies and the high Plains. Overrunning of this wedge of cold air produced damaging snowfalls of record intensity in eastern Colorado. Pueblo reported a record 14 inches of heavy, wet snow which fell on the 29th and 30th with heavy damage to trees and shrubs.

Also near month's end hurricane Gracie moved inland across the South Carolina coast about 11 a.m. EST, September 29, a little south of Charleston. Winds were estimated near 120 m.p.h. and tides up to 9.7 ft. above mean low water in the Charleston area. Heavy rains along the storm path (fig. 8) totalled over 6 inches in most of South Carolina, 8 inches in western North Carolina, 10 inches locally in Virginia, 6 inches in western Maryland, 4 inches in West Virginia, and from 1 to 2 inches in the New England States. Figure 7D does not reflect this rainfall since the hurricane had not moved inland until the last two days of the month.

8. HURRICANES AND TYPHOONS

ATLANTIC

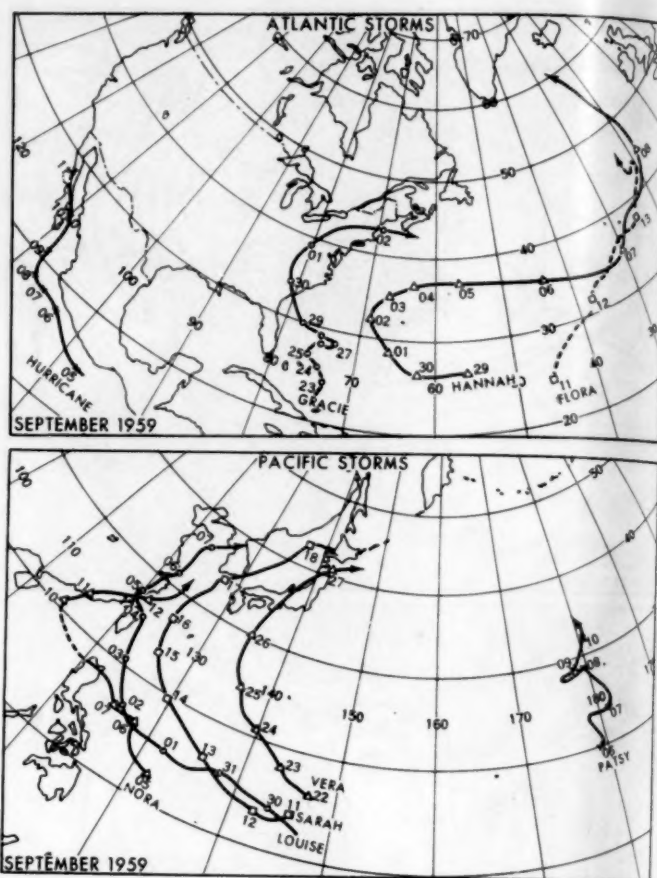Three hurricanes developed in the Atlantic during the month. All three developed hurricane winds north of

FIGURE 8.—Selected tropical storm tracks for September 1959. All attained hurricane force except Nora. Dates represent approximate 0000 GMT positions.

20° N., which is unusually far north except for storms which originate near the Bahamas as hurricane Gracie did. Flora may have originated south of this latitude, but Hannah clearly appeared to have originated north of 26° N. All three developed close to the stage of the index cycle considered most propitious for hurricanes; i.e., at times of high index, when the westerlies were farthest north and the subtropical easterlies strongest. Hurricane Flora developed around the 9th, Gracie on the 22d, and Hannah on the 27th, which were times when the index was close to its maximum. The development of Gracie and Flora appeared to be associated with the well-known shearing process, in which the southern portions of full-latitude major troughs become disassociated from the more rapidly moving northern portions near times of high index [1].

These storms traced widely diverse paths as shown in figure 8. Hurricane Flora followed a very unusual path, heading rapidly for the Azores after detection on the 9th, with highest winds reported near 65 knots. The eastward component of this motion throughout its entire duration may be attributed to the sharp drop in the speed and lati-

tude of the westerlies between September 9 and 12 (fig. 3). The latter circumstance occurred in consonance with retrogression of the blocking anticyclone from near the United Kingdom to a position south of Iceland during this period. As a result the depressed westerlies in the eastern Atlantic swept hurricane Flora rapidly northeastward.

Hurricane Gracie, on the other hand, had its inception in the ascendant phase of the index. Thus the westerlies were increasing their latitudinal separation from the storm, and it drifted slowly northwestward. Around the time of the index maximum, from the 25th to the 27th, the hurricane wallowed indecisively while blocked by a High which moved eastward across New England. The hurricane resumed its northwestward course toward the coast on the 27th as the High center moved east of the storm's meridian. This was also about the time hurricane Hannah put in its appearance about 1400 miles farther east. Between October 1 and 2 both Gracie (now an extratropical Low), and hurricane Hannah recurved sharply eastward as the index dropped below the normal.

Thus it appears that the Atlantic hurricanes this month were spawned when the speed of the temperate westerlies (and the subtropical easterlies) was above normal, at which time westward motion prevailed. When the zonal index declined below the normal, eastward motion and/or recurvature to eastward occurred.

PACIFIC

In the North Pacific, 12 tropical cyclones were observed this September. In the eastern Pacific, two hurricanes developed off the west coast of Mexico, and one tropical storm occurred east of Hawaii. The first eastern Pacific hurricane (fig. 8) was detected near 14° N., 98° W. on September 4, about the time the index rose above the normal. It apparently disintegrated over Baja California on the 11th when the index was dropping sharply. The second hurricane (not shown) was detected near 17° N., 119° W. on the 21st and, after following an irregular path, apparently dissipated on the 26th near 20° N., 130° W.

Tropical storm Wanda, east of Hawaii, was shortlived, as was tropical storm Opal and depressions Marge, Ruth, and Thelma (not shown). Tropical storm Nora (Sept. 5-12) moved from east of the Phillipines across Luzon and passed near Hong Kong into the Yellow Sea (fig. 8). Highest winds were estimated at about 35 knots.

In addition to typhoon Patsy in the central Pacific, and typhoon Louise which developed late in August but hit Formosa early in September, two other severe typhoons wreaked widespread destruction in the Far East. These were typhoon Sarah and typhoon Vera, whose tracks are shown in figure 8.

Typhoon Sarah, first detected on September 11, reached typhoon intensity on the 12th, passed over the Ryukyus on the 15th, and swept across southern Korea into the Sea of Japan. Winds well over 100 knots brought considerable destruction to Korea and southern Japan, and heavy casualties in the fishing fleets.

About 10 days later typhoon Vera, a monstrous storm in both size and intensity, after originating near the Marianas, moved northwestward and then northward along the 135° E. meridian, striking central Honshu on the 26th. Winds well over 100 knots plus excessive precipitation and tides resulted in enormous casualties and destruction, placing it in the category of one of the greatest natural catastrophies in the modern history of Japan.

REFERENCE

1. J. Namias "Long Range Factors Affecting the Genesis and Paths of Tropical Cyclones," *Proceedings of the UNESCO Symposium on Typhoons, 9-12 November 1954*, Tokyo, pp. 213-219.

Weather Note

A REPORTED SEA LEVEL PRESSURE OF 877 MB.

C. L. JORDAN

Florida State University, Tallahassee, Fla.

A dropsonde observation made in the eye of typhoon Ida at approximately 0500 GMT, September 24, 1958 showed a sea level pressure of 877 mb. (25.91 in.) which is believed to be the lowest sea level pressure ever recorded.[1,2] This is about 10 mb. lower than the generally accepted minimum pressure of 26.185 in. (886.7 mb.) which was observed in a typhoon in 1927 by the steamship *Sapoeroea* east of the Philippines, and about 15 mb. lower than the lowest Western Hemisphere reading of 26.35 in. (892.3 mb.) which was observed at Lower Matecumbe Key during the Florida Keys hurricane of September 1935 (cf. [2]).

The dropsonde observation cited above was made from the 700-mb. level by a U.S. Air Force reconnaissance aircraft of the 54th Weather Reconnaissance Squadron. At the time of this observation, typhoon Ida was located

[1] The value of 873 mb. reported for this typhoon in the 1958 *Climatological Data—National Summary* (p. 93) represents an estimate of the sea level pressure based on the last reported information from the dropsonde. The pressure-height computation from this sounding, which was made 8 hours earlier than the one considered in this note, gave 878 mb. as the sea level pressure.

[2] Spectacular photographs of the eye of this storm taken from very high levels have been presented by Bundgaard, Fletcher, and Smith [1].

MONTHLY WEATHER REVIEW

TABLE 1.—*Pressure-height, temperature, and dewpoint data for standard and significant levels in the dropsonde observation made in the eye of typhoon Ida at 0500 GMT September 24, 1958. Since these data were taken from coded reports, the listed temperature and dewpoint values may deviate 0.1° C. from those shown in the original records.*

Height (ft.)	Pressure (mb.)	Temperature (° C.)	Dewpoint (° C.)
0	877	27. 8	26. 5
910	850	26. 8	24. 8
	835	26. 2	23. 5
	769	29. 5	15. 5
	748	27. 8	14. 2
6580	700	29. 8	14. 2

near 18.9° N., 135.3° E., or about 600 miles northwest of Guam. The temperature, dewpoint, and pressure-height data reported in this sounding are shown in table 1. The temperature varied over a range of less than 4° C. and the maximum value of 29.8° C. (86° F.) was reported at the 700-mb. level. The 700-mb. surface was reported at 6580 ft. and the 850-mb. surface at 910 ft. above sea level.

In the dropsonde observation the 700-mb. height was determined by using the pressure and radio altimeters aboard the aircraft, and the 850-mb. height and sea level pressure were computed using the temperature and humidity data measured at flight level by the aircraft instruments and at levels below the aircraft by the dropsonde instrument. The sounding under consideration was found to be hydrostatically consistent and the vertical temperature distribution is realistic, in view of those found in other deep typhoons [3].

The sea level pressure is relatively insensitive to small temperature errors since a relatively thin layer is involved. In fact, an error of 5° C. at all levels would change the sea level pressure less than 4 mb. in the present case. The most likely source of major error in cases of this type is in the aircraft altimetry which provides the beginning point in the pressure-height computation. Errors of this type tend to be systematic for a given aircraft and flight, but are normally small on the reconnaissance aircraft since calibration checks are made as a routine part of each flight. In the case in question, the 700-mb. heights reported in the vicinity of Guam are consistent with those given by radiosonde observations. Any systematic error would undoubtedly have been less than 80 ft. which would correspond to sea level pressure errors less than 3 mb.

Perhaps the strongest supporting evidence of the relia-

bility of the dropsonde observation under examination is the fact that another dropsonde observation made about 8 hours earlier from a different aircraft reported a sea level pressure of 878 mb. A third dropsonde made about 23 hours later reported a sea level value of 886 mb. Since the three dropsonde observations were made from different aircraft, there is little chance that altimetry errors could have been important. Even if the improbable assumptions are made that the aircraft pressure-height values were 150 ft. too low and the reported temperatures were 3° C. too warm at all levels, the soundings made at 2100 GMT, September 23 and 0500 GMT, September 24 would still show sea level pressures lower than the previously accepted record value of 886.7 mb.

In view of the evidence cited above, it is felt that typhoon Ida of 1958 should be accepted as the deepest cyclone of record. Typhoons with central pressures as low as those reported in Ida of 1958 are undoubtedly rare. However, there have been at least seven other typhoons in the past eight years in which the minimum sea level pressure was reported to be 900 mb. or lower.[3] It is believed that typhoon Nina of 1953 would qualify as the nearest rival to Ida of 1958 with dropsonde sea level pressures of 886 and 883 mb. All of these very deep typhoons have contained extremely strong winds and have covered very large areas. In the case of typhoon Ida of 1958, the maximum reported 700-mb. wind speed was 185 kt. On September 23–24 at the times of the extremely low central pressures, typhoon-force winds were reported both at the surface and 700-mb. levels at distances as great as 275 miles from the storm center.

ACKNOWLEDGMENT

REFERENCES

1. R. C. Bundgaard, R. D. Fletcher, and J. R. Smith, "Typhoon-Eye Cloud Patterns as Viewed from Above," *Weatherwise*, vol. 12, No. 2, Apr. 1959, pp. 64–66.
2. G. E. Dunn, "Tropical Cyclones," *Compendium of Meteorology*, American Meteorological Society, Boston, 1951, pp. 887–901.
3. C. L. Jordan, "The Thermal Structure of the Core of Tropical Cyclones," *Geophysica*, vol. 6, No. 3/4, 1958, pp. 281–297.

[3] These were Marge of 1951, Nina of 1953, Ida of 1954, Virginia, Hester and Lola of 1957, and Grace of 1958.